MANTLE POTENTIAL TEMPERATURES OF 4.5 TO 47 MA HAWAIIAN VOLCANOES USING OLIVINE THERMOMETRY: IMPLICATIONS FOR MELT FLUX VARIATIONS

A THESIS SUBMITTED TO THE GRADUATE DIVISION OF THE
UNIVERSITY OF HAWAIʻI AT MĀNOA IN PARTIAL FULFILLMENT
OF THE REQUIREMENTS FOR THE DEGREE OF

MASTER OF SCIENCE

IN

GEOLOGY AND GEOPHYSICS

DECEMBER 2016

By

Jonathan P. Tree

Thesis Committee:

Michael O. Garcia, Chairperson

Eric Hellebrand

Thomas Shea

Keywords: Hawaiʻi, hotspot, melt flux, mantle, mantle potential temperature, olivine thermometry, olivine, geochemistry, petrology

Acknowledgements

This project benefitted from the support of my advisor, Michael Garcia; and committee members Eric Hellebrand and Thomas Shea. Additionally, University of Hawai‘i at Mānoa faculty including Neil Frazer, Garrett Ito, and Paul Wessel contributed to development of the methods and approach to quantifying uncertainties of results and interpretations. Keith Putirka from California State University, Fresno helped with understanding olivine thermometers and new approaches for calculations used in this study. The additional samples sent by Alexandra Hangsterfer from the Scripps Institution of Oceanography were valuable in extending the geographic range of the sample suite. The efforts of Mike Vollinger from the University of Massachusetts in expediting XRF analyses was greatly appreciated. Student lab technicians, Lauren Froberg and Lerma Gamiao, for sample preparation and assistance. This project was supported by NSF grant number: EAR-1219955 to Garcia. I would also like to thank: my wife, Dana and my mother-in-law for helping with revisions, my family, my dog, Maggie, for all of their unconditional support; and my good friend, Harrison Togia, who’s insightful conversations of the Hawaiian Ridge geophysics that added alternative views about the project.

Abstract

Hawaiian Ridge volcanoes vary in volume by a factor of 50 due to variations in the melt flux of the Hawai‘i mantle plume. One potential cause for these variations is the plume’s temperature. The objective of this study is to evaluate the relationship between melt flux variations and mantle potential temperature (T_p) of the plume during the formation of the Northwest Hawaiian Ridge (NWHR) that extends 2800 km northwest of the main Hawaiian Islands. Using olivine thermometry of 25 lavas from 10 Hawaiian volcanoes ranging from 1 x 10^3 km^3 to 54 x 10^3 km^3 in volume and 4.5 to 47 Ma in age, mantle potential temperatures are calculated. High-precision electron microprobe analysis of olivine compositions revealed that most of these volcanoes shared similar olivine forsterite (Fo) compositions (~80-88% Fo) with the exception of high forsterite olivines in Gardner lavas (91.85 % Fo, the highest measured in Hawaiian lavas). The highest forsteritic olivines from each sample were used to estimate parental magma compositions. A Monte Carlo simulation method was used to calculate the olivine-liquid equilibration temperature ($T^{ol\text{-}liq}$) of these magmas, the T_p, and uncertainties in temperature associated with equilibrium assumptions made for parental magma composition estimates. The minimum $T^{ol\text{-}liq}$ and T_p are for Daikakuji lavas from the second smallest examined volcano at northern end of NWHR (1335 ± 26; 1374 ± 48 ºC). The maximum T_p is at Gardner, the largest volcano located in the central part of the NWHR (1614 ± 26; 1703 ± 56 ºC). These results yield a T_p increase of 329 ºC for the ≥ 12.4 Ma section of the NWHR. Southeast of Gardner, T_p decreases at Mokumanamana to 1521 ± 50 ºC. The T_p of the NWHR volcanoes between Mokumanamana and West Nīhoa show no systematic change similar to variations in the melt flux. The maximum T_p from the southeastern portion of the NWHR was from Nīhoa (1632 ± 54 ºC) and the minimum T_p from West Nīhoa (1517 ± 56 ºC). A second increase in T_p was observed from new T_p estimates for Kaua‘i (1567 ± 42 ºC) to the current estimate range for volcanoes of the Island of Hawai‘i (1632 ºC ≥ T_p ≥ 1690 ºC). These variations in T_p along the Hawaiian Ridge follow an equivalent trend that is observed in the melt flux. The maximum T_p from each volcano have significant Spearman’s rank correlations with the distance from Mauna Loa, the melt flux, and volumes of these volcanoes. These correlations suggest that there is a strong coupling between the melt flux and the temperature of the Hawaiian mantle plume. T_p estimates from the Galápagos and Iceland hotspots show an opposite cooling trend over time. The Louisville hotspot track shows a dramatic decrease in the melt flux since 20 Ma. The T_p estimates from this study show that the Hawaiian hotspot is unique. The plume’s thermal history shows two instances of increasing T_p with increasing melt flux.

Table of Contents

List of Figures

List of Tables

1) Overview

Inquiry and estimation of the temperature and pressure for different processes that occur on Earth have remained a primary focus of geologists since as early as the 19th century. For example, Charles Daubeny (1835) developed one of the first geological thermometers in his attempt to measure the temperatures of recent lava flows on Vesuvius after a period of cooling due to intermittent rain. These types of geological investigations have been transformative throughout the past few centuries and have remained a central focus in modern research attempting to understand the role that these physical parameters play in global volcanism.

One main question at the core of the discussion of temperature has been: What is the relative contribution that temperature has as a driving force for the voluminous eruptions that generate large igneous provinces and intraplate volcanic chains like the Hawaiian Islands? Further, are these features the result of melting an anomalously hot mantle or are they the result of other mechanisms? Early efforts in understanding these features were carried out by Wilson (1973) and Morgan (1971) establishing the concept of a "hotspot". They defined these hotspots as the focal points of volcanism due to convective upwelling, or plumes, of unusually hot mantle (Morgan, 1971). The localized volcanism at hotspots, paired with plate motion, was used to explain volcanic chains with age progressions increasing in the direction of plate motion (Wilson 1963a, b). In addition to the sustained volcanism, hotspots thermally rejuvenate the lithosphere, creating anomalously shallow topography that extends hundreds of kilometers beyond the area of the volcanic edifice (i.e. bathymetric swell, e.g., Crough, 1983).

Both volcanism and the bathymetric swell are thought to be related to excess heat. However, heat flow measurements of the Hawaiian swell near Midway Island show no systematic variation, leading geologists to rely on dynamic uplift and modest excess

temperatures to reconcile the anomalous bathymetric depths around the Hawaiian hotspot (Von Herzen, et al., 1989). The lack of excess heat flow around Hawaii and other global hotspot locations has spurred modern investigations that have attempted to determine if "hotspots" are truly hot (Anderson, 2000). Recent studies have continued to refine the classical definition and role of hot spot mantle plumes and their interactions with the lithosphere, convection and chemical transport from the deep mantle, and the lithology and composition of the mantle (e.g., Ballmer et al., 2015). Though substantial work has been done on mantle plumes, the fundamental notion that hotspots are truly the result of thermal upwelling is still met by skepticism (Foulger and Natland, 2003). Alternative mechanisms have invoked asthenospheric and lithospheric processes without excess heat supply (Foulger et al. 2005).

McKenzie and Bickle (1988) provided a conceptual reference for the "mantle potential temperature" or T_p. The T_p is the temperature that a parcel of mantle would have if it were to rise to the surface adiabatically (Figure 1; McKenzie and Bickle, 1988). To quantify "excess heat" at any hot spot melting anomaly using T_p, the excess temperature is defined as the temperature difference between a mantle melting anomaly and the surrounding ambient mantle ($T_{ex}=T_p^{\text{hot spot}} - T_p^{\text{ambient}}$). Mid-ocean ridges (MOR) are thought to undergo passive upwelling, so $T_p^{\text{ambient}}=T_p^{\text{MOR}}$. A T_{ex} with sufficient magnitude to drive active upwelling of mantle material is critical to the thermal buoyancy mechanism of the plume model. Many studies attempted to constrain the value of T_p^{MOR} using a variety of approaches. Most modern attempts have converged on values $T_P^{\text{MOR}} = 1454 \pm 78$ °C (Putirka et al., 2007) though it may be as low as 1280 ^{o}C (McKenzie and Bickle, 1988).

Using the mantle potential temperature of the mid-ocean ridge mantle as a baseline to compare the amount of excess heat at hotspots around the globe, one can then test the thermal

buoyancy theory of the hotspot mantle plumes. However, many hotspot locations have additional complexities. These complexities include hotspot locations proximal to mid-ocean ridge plate boundaries, those that do not show age progressions, those that only erupt short lived pulses of volcanism, and those involving eruptions that occurred during times in which the Earth was assumed to have a higher average internal temperature. Estimates of potential temperatures at ridge-plume interaction volcanoes are particularly problematic and obfuscate the investigation of temperature related to mantle plume volcanism. Nevertheless, many investigations of the mantle potential temperatures of these features have resulted in excess temperatures. Estimates of the mantle potential temperatures of the Iceland hotspot (which interacts with the Mid-Atlantic Ridge) are 1616 ^{o}C (Putirka et al., 2007). This suggest that even with heat loss expected by interaction with the cooler mid-ocean ridge mantle, the Iceland plume exhibits excess temperatures up to 162 ^{o}C, greater than the average estimates of ambient mantle temperature. Mantle potential temperature estimates from the Galápagos hotspot, another location known for plume-ridge interactions, reach up to 1620 ^{o}C (Herzberg and O'Hara, 2002). Mantle potential temperatures under the Hawai'i and Samoa hotspots are identical with T_p of 1500-1700 ^{o}C (Putirka et al., 2007).

The excess mantle potential temperatures at locations of persistent intraplate volcanism suggests these hotspots are in fact due to thermal mantle anomalies. The question then becomes: How long have these hotspots exhibited these anomalous mantle temperatures, and have these temperatures changed with time? In general, it is thought that hotspots cool down with time and magmatic productivity decreases (White and McKenzie, 1989). The Galápagos and Iceland hotspots have presumably undergone secular cooling (Herzberg and Gazel, 2009). This is because hotspots are thought to originate as super-heated plumes producing large volumes of

volcanics (e.g. flood basalts or Archean komatiites; Herzberg, 1995). With time, the superheated plumes' heat supply declines and volcanic activity decreases. The Iceland and Galápagos hotspots have an additional tectonic interaction with mid-ocean ridge systems. This interface with the cooler ambient mantle makes it difficult to separate the heat loss due to secular cooling and the effect that mid-ocean ridge development has on the temporal behavior of these hotspot. The Hawaiian hotspot is an intraplate oceanic island chain far from any plate boundary, distant from any plate margin or continent for more than 70 Myr (Garcia et al., 2015). The relative geologic simplicity makes Hawaii the archetypal example of mantle plume volcanism and the ideal locality to conduct temporal geologic investigations of the hotspot's thermal history.

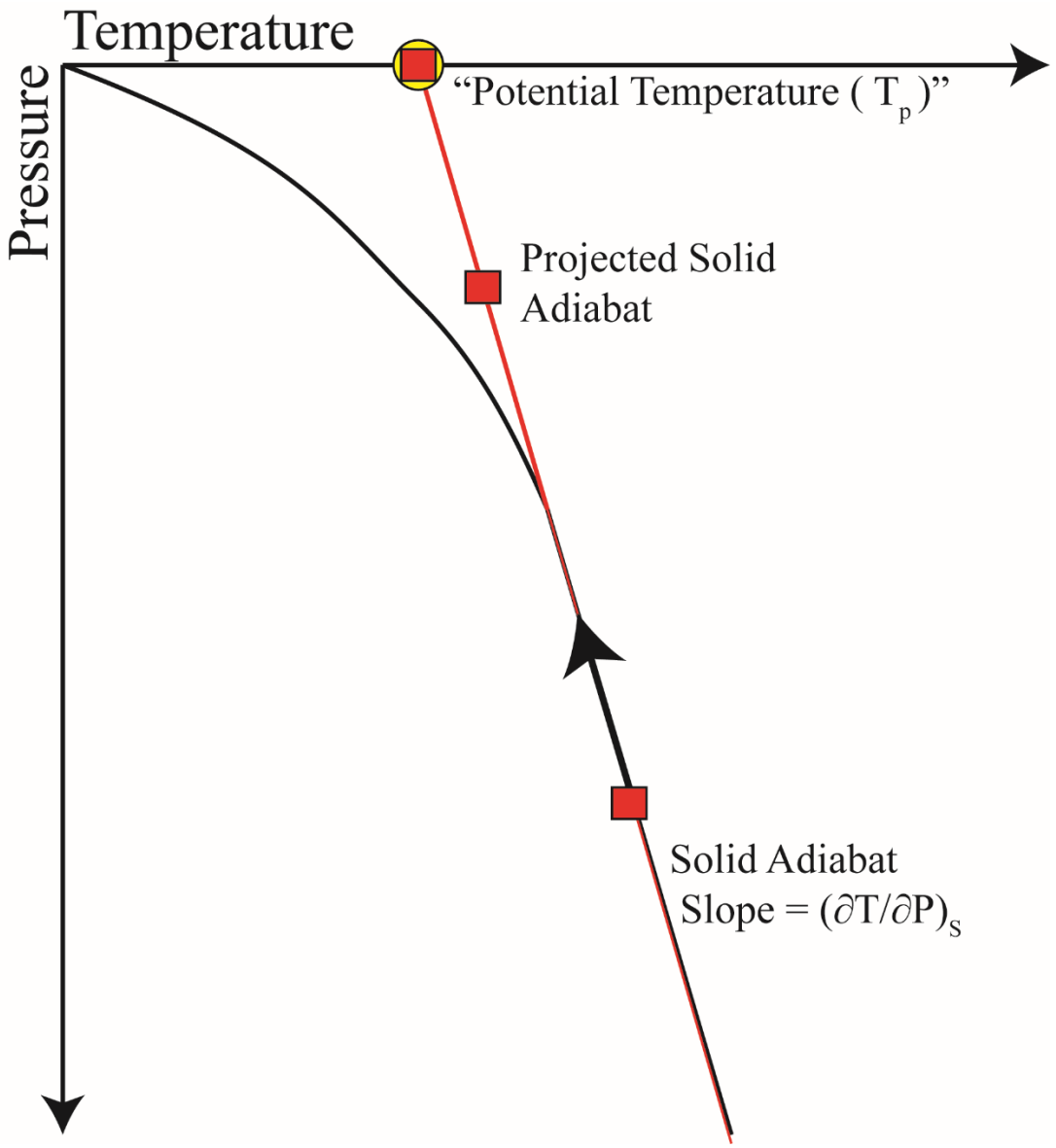

Figure 1. Conceptualization of mantle potential temperature. A parcel of mantle represented by the red box rising in the mantle along a solid adiabat without melting. The temperature of that parcel of solid mantle at the surface is the mantle potential temperature, Tp (circled red box). After Putirka et al. (2007).

2) Introduction

The Hawaiian-Emperor (H-E) chain is a ~6000 km long ridge of submarine and subaerial volcanoes. The chain is subdivided into three segments. The northern 2500 km long Emperor Seamounts segment contains at least 45 volcanoes that form a submarine ridge from Kamchatka to the Hawaiian-Emperor bend (HEB, Figure 2; Clague, 1996). Southeast of the HEB, the axis of the volcanic ridge changes from the predominantly N-S orientation of the Emperor Seamounts to a NW-SE orientation. The middle Northwest Hawaiian Ridge (NWHR) segment extends southeast of the HEB to Middle Bank seamount and includes at least 51 volcanoes stretching over 2800 km (Figure 2). The main Hawaiian Islands form the 700 km southern segment from Ka‘ula to Hawai‘i with 19 volcanoes (Garcia et al., 2015).

Volcano volumes vary significantly along the NWHR (i.e., 1 x 10^3 km^3 for the Unnamed Seamount, and 54 x 10^3 km^3 for Gardner; Bargar and Jackson, 1974; Figure 2). Magma productivity (melt flux) was relatively low after the formation of the HEB (0.2-0.5 m^3 s^{-1}) producing small isolated seamounts (Wessel, 2016; Figure 2). Southeast of Academician Berg, flux rates increased markedly to 4.8 m^3 s^{-1} near Gardner (Figure 2). Melt flux subsequently decreased to relatively moderate rates until Middle bank at the southeastern extent of the NWHR (~2 m^3 s^{-1}; Figure 2). The Hawaiian Islands mark a second increase in melt flux up to 8.8 m^3 s^{-1} at Mauna Loa (Wessel, 2016).

One hypothesis is that variable melting conditions (i.e., temperature/pressure) could have driven melt flux variations, given that melt generation is highly sensitive to small perturbations in the plume’s thermal structure (McKenzie and Bickle, 1988; White, 1993; Lee et al., 2009). Assuming a constant rate of upwelling mantle material, the T_p would require an increase of ~175-200 ^oC over the last ~45 Myr to sustain the observed melt production rates along the

Hawaiian Ridge (White, 1993). The thermal history of the plume has previously been inferred from geodynamic modeling of plume buoyancy flux models to generate the Hawaiian swell topography (e.g., Ribe and Christensen, 1999; Togia, 2015). This method approximates T_p by solving for combinations of mass flux and plume temperature that minimize error in reproducing the swell shape. However, these solutions are non-unique, making it difficult to decouple mass flux and temperature (Togia, 2015). Geochemical approaches to measuring temporal variations in T_p for the Galápagos and Iceland hotspots indicate secular cooling (e.g., Herzberg and Gazel, 2009). Does the Hawaiian hotspot plume show similar evidence of secular cooling over its eruptive history?

Olivine thermometry provides an alternative approach to estimate T_p (Putirka, et al., 2007). Whole-rock and olivine compositions from 25 lavas collected from 10 volcanoes with contrasting melt flux estimates along the NWHR from the HEB to Kauaʻi were utilized to investigate the thermal history of the plume (Figure 2). These olivine-phyric lavas were used to estimate the maximum olivine-liquid temperatures ($T^{ol\text{-}liq}$). The $T^{ol\text{-}liq}$ were corrected for adiabatic decompression and heat of fusion to establish the temporal evolution of T_p of the Hawaiian mantle plume from ~4.5-47.5 Myr. We investigated if a relationship exists between the mantle potential temperature and the variations in melt flux along the NWHR volcanoes. Correlation coefficients used to quantify these relationships indicate that the T_p and the melt flux are strongly correlated at a 95% confidence level. T_p appears to have risen twice since the formation of the HEB along with the pulses of increasing melt flux during the formation of Gardner and Mauna Loa. Thus, we conclude the Hawaiian hotspot shows no evidence of secular cooling.

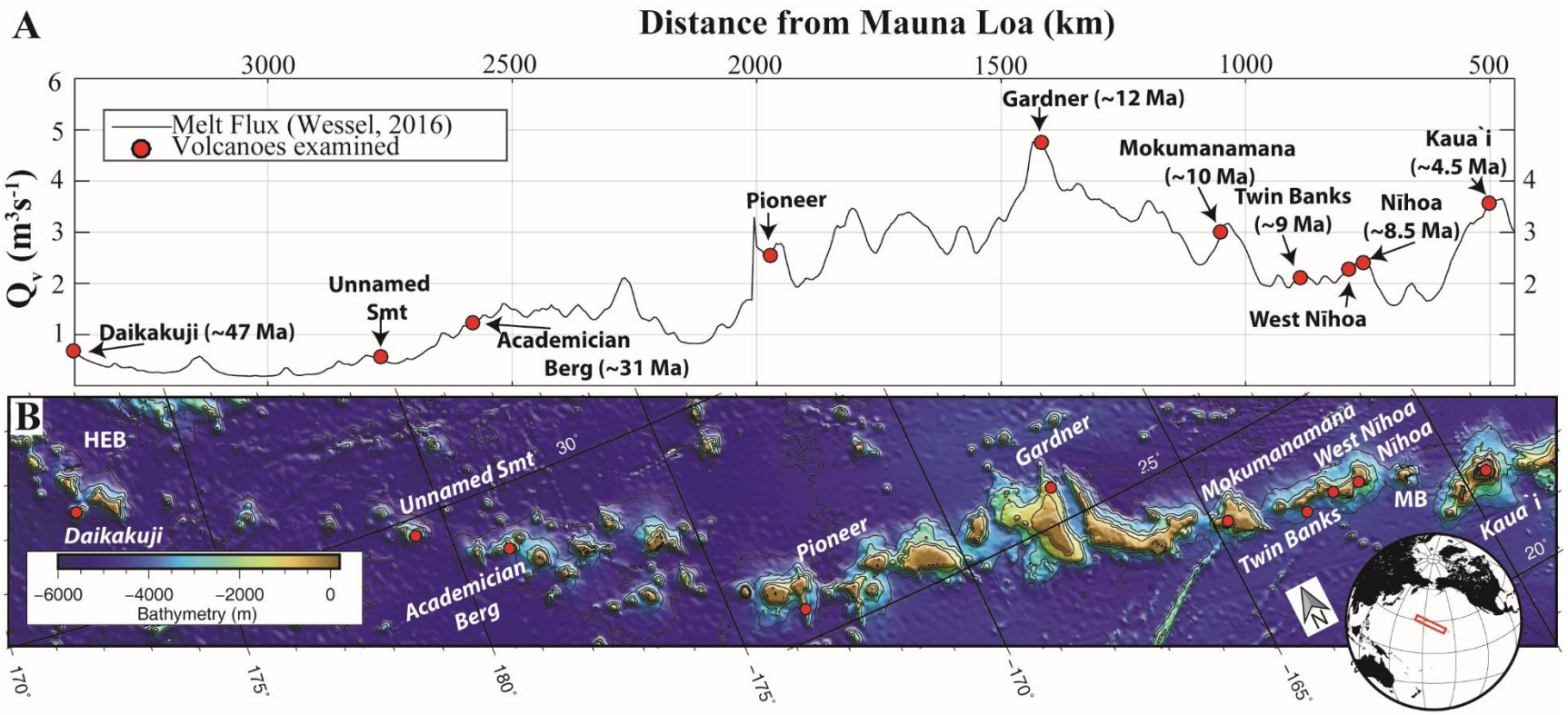

Figure 2. (A) Plot of Melt flux (Q_v) along the NWHR as a function of distance from Mauna Loa. Red circles are the location of the volcanoes examined in this study. (B) Bathymetric map of the Northwest Hawaiian Ridge with 1000 meter contours generated using ETOPO1 (Amante and Eakins, 2009). Red circles show sample locations for this study. HEB—Hawaii-Emperor Bend; MB—Middle Bank. The largest differences in volcanic volume between volcanoes that are examined in this study are the Unnamed Seamount (1 x 10^3 km^3) and Gardner Pinnacles (54 x 10^3 km^3).

3) Samples and Petrography

3.1) Samples

The NWHR sample collection at the University of Hawai‘i at Mānoa (UH) has samples from 17 of the 51 volcanoes. A subset of low to moderately altered olivine-phyric lavas were selected from the UH collection containing 25 submarine and subaerial lavas from 10 NWHR volcanoes. Dredged samples were collected during three UH expeditions in 1972, 1976, and 1984. They are labeled as year-dredge-sample (e.g. 72-20-GG; cruise year 1972, dredge number 20, sample GG). Other UH samples were collected by the PISCES-V submersible during two cruises in 2003 and 2011 (labeled with the prefix P5). Samples were also obtained from the Scripps Institution of Oceanography collection. They include dredged lavas just south of the HEB at Daikakuji (labeled A-55- sample number), and subaerial lavas that were collected on the islands of Nīhoa (labeled with the prefix NIH) and Necker (now called Mokumanamana; labeled with the prefix NEC-).

3.2) Petrography

Modal mineralogy was determined by point counting (Table 1). Olivine is the dominant phase (3.0 to 42.6 total vol %). It showed the greatest variation for phenocrysts (>0.5 mm; 0 to 37.8 vol %), and less variation for microphenocrysts (0.1-0.5 mm; 0 to 12.6 vol % (Table 1). Most of the samples (17/25) are picrites, with > 15 vol % olivine (Table 1). The remaining lavas are olivine-phyric (5-15 vol % olivine phenocrysts) or weakly olivine-phyric (0-5 vol % olivine phenocrysts). The olivine-phyric samples from the two oldest seamounts, Daikakuji and the Unnamed seamount, contain only olivine microphenocrysts (Table 1). Olivine morphologies are most commonly euhedral to subhedral, and less frequently resorbed or skeletal (Appendix 1). Olivine phenocrysts are well preserved, whereas microphenocrysts are commonly altered with

only relict cores. Cr-spinel is common as inclusions in olivine. Clinopyroxene (cpx) phenocrysts are present in two samples and microphenocrysts in five samples (Table 1; Appendix 1). The groundmasses of the NWHR samples are composed of cryptocrystalline material or fine-grained plagioclase, clinopyroxene, and Cr-spinel (Table 1). Vesicularity ranges from < 0.1 to 23 vol % and vesicles are commonly lined with zeolites (Table 1). Most samples (15 out of 25) have low levels of alteration (Table 1; Appendix 1). Moderate alteration referred to samples with alteration rims > 0.1mm around olivine, zeolite clays filling vesicles, and/or common discoloration of matrix. Moderate alteration was observed in the oldest samples (Pioneer to Daikakuji) and three younger samples (Mokumanamana, Twin Banks, and West Nīhoa; Table 1; Appendix 1).

TABLE 1. PETROGRAPHY OF NWHR LAVAS BASED ON 500 POINT MODES

				Olivine		Clinopyroxene		Plagioclase			
Volcano	Age	Ref.	Sample	Ph	Mph	Ph	Mph	Mph	Ves	GM	Alt
Daikakuji	47.5 ± 0.3	1	A-55-1	0.0	12.6	-	-	-	<0.1	CC	mod
			A-55-2	0.0	6.4	-	<0.1	-	<0.1	F	mod
			A-55-4	0.0	6.6	1.4	0.6	2.2	0.6	F	mod
Unnamed	ND		84-28-C	0.0	3.0	-	-	-	17.4	CC	mod
			84-28-D	0.0	3.4	-	-	-	23.2	CC	mod
Academician Berg	31.0 ± 0.2	2	72-20-GG	20.1	2.4	-	-	-	9.4	CC	mod
Pioneer	ND		P5-526-rk2	4.2	12.7	-	-	-	8.3	HP	mod
Gardner	12.3 ± 2.0	3	76-6-7-B	17.9	4.6	-	-	-	0.8	CC	low
			76-6-7-C	20.0	5.1	-	-	-	1.2	CC	low
			76-6-7-F	21.8	3.8	-	-	-	0.8	CC	low
			76-6-7-H	19.6	5.7	-	-	-	1.2	CC	low
			76-6-7-I	15.3	6.7	-	-	-	1.8	CC	low
			76-6-7-J	23.7	3.2	-	1.0	-	0.6	CC	low
Mokumanamana	10.3 ± 0.8	4	NEC-2A	35.2	-	-	2.0	-	8.4	CC	mod
			NEC-3A	27.5	1.1	5.4	1.4	-	9.6	CC	low
Twin Banks	9.6 ± 1.6	3	P5-688-1	31.1	2.5	-	-	-	16.8	CC	mod
West Nīhoa	ND		76-9-11	32.0	-	-	-	-	<0.1	CC	mod
Nīhoa	7.5 ± 0.6	5	NIH-D-1-2	20.8	4.0	-	-	-	<0.1	CC	low
			NIH-D4	19.6	9.6	-	-	-	<0.1	CC	low
			NIH-F-5A	37.8	4.8	-	-	-	16.8	IG	low
			NIH-F-9	32.3	3.5	-	-	-	7.7	CC	low
			NIH-W-11-1	28.4	2.3	-	-	-	23.2	CC	low
Kauaʻi	4.3 ± 0.2	6	KV04-16	24.0	6.0	-	-	-	<0.1	CC	low
			KV04-19	3.2	5.1	-	-	-	6.0	CC	low
			KV04-22	12.6	3.4	-	-	-	<0.1	IG	low

Note: Mineralogy is reported for phenocrysts (Ph; >0.5 mm), and microphenocysts (Mph; 0.1-0.5 mm); Age represents the oldest age (for shield if available); ND—Not Determined; Ref.—Reference for ages: 1—O'Connor et al., 2013; 2—Clague et al., 1975; 3—Garcia et al., 1987; 4—Dalrymple et al., 1987; 5—Dalrymple et al., 1974; 6—Garcia et al., 2010; Ves—vesicularity; GM—groundmass, CC—cryptocrystalline, F—felty, HP—hyalopilitic, IG—intergranular; Alt—Alteration; low—minor alteration of olivine with thin alteration rims 0.0-0.1 mm; matrix is largely unaltered or discolored with minor zeolites or clays lining vesicles; mod— moderate alteration with olivine alterations rims, and frequent matrix alteration and discoloration. This qualitative assessment of alteration is best illustrated by the photomicrographs (Appendix 1).

4) Whole-Rock Geochemistry

Sixteen new lavas were analyzed by X-ray fluorescence (XRF) for whole-rock major and trace element compositions (Table 2). These data were combined with previously published XRF analyses for the other remaining nine lavas (Table 2). Most of the lavas are tholeiitic (18/25 samples), five are transitional, and two are alkalic (Figure 3). The alkalic index (Alk_i), a metric derived by the deviation from the Macdonald-Katsura line (1964), was used to determine the possible eruptive stage of these lavas (Figure 3; Carmichael et al., 1974; Rhodes and Vollinger, 2004). Intraplate tholeiitic magmas form when the volcano is centered over the core of the hotspot where the highest rates of heat supply produce the most voluminous shield stage volcanism. These are defined here as having an alkalic index values less than -0.3, and include 18 tholeiitic basalts, and one picro-basalt (Figure 3). Five other lavas are transitional, defined here as having an alkalic index within the range of $-0.3 \leq Alk_i \leq 0.3$ (Figure 3). These lavas erupted during times of waning heat supply as the volcano moved away from the center of the plume. Two lavas from an Unnamed Seamount (84-28-samples) have $Alk_i = 1.23$ and 1.06 and are assumed to be derived from a cooler magma source. No tholeiites have been collected from the Unnamed Seamount.

The MgO content of the sample suite ranges between 5.7 - 23.0 wt. % (Figure 4). All lavas appear to lie along olivine-only control lines except those from Daikakuji with the lowest MgO content (Figure 4). Two of the higher SiO_2 Daikakuji lavas contain clinopyroxene microphenocrysts and lack olivine phenocrysts (Table 1). The lavas from the Unnamed seamount (84-28-C and 84-28-D) have the highest CaO/Al_2O_3 ratios. High CaO/Al_2O_3 would indicate either clinopyroxene accumulation or plagioclase fractionation, which is inconsistent with the absence of these phases in these samples (Table 1). The increase in Al_2O_3 with decreasing MgO

suggests a negligible effect of plagioclase crystallization, consistent with the rarity of plagioclase phenocrysts and microphenocrysts in these rocks (Table 1). Rhodes (2016) has noted that the strong linear trend in Al_2O_3-MgO is typical in Hawaiian tholeiites. Samples from the NWHR plot along this same trend line (Figure 4). The samples from the Unnamed seamount also lie along the Al_2O_3-MgO trend defined by negligible plagioclase fractionation. The alkalic Unnamed seamount samples plot above the trend line, similar to the elevated Al_2O_3 values for a lower MgO content in Hawaiian post shield lavas found by Rhodes (2016). Most of the NWHR samples plot along two distinct arrays in MgO-TiO_2, indicative of multiple distinct magma melting conditions. Transitional rocks tend to form the elevated TiO_2 array. Elevated TiO_2 contents either reflect more fertile source compositions or different source pressures of magma generation (Putirka et al. 2010).

Geochemical indicators of alteration include substantial mass losses on ignition (LOI > 2%), and K_2O/P_2O_5 (K/P) for tholeiitic samples, which can be used in addition to petrographic indicators (Table 1; e.g. Wright, 1971, Frey et al., 1991). The K/P ratio for unaltered tholeiitic lavas is typically 1.5-2.0 (e.g. Wright 1971; Frey et al. 1990; Rhodes et al. 2012). Tropical weathering causes loss of K_2O, and submarine lavas can undergo P_2O_5 addition by precipitation of zeolites from surrounding seawater, both lowering the K/P ratio. The XRF analyses of the Hawaiian Ridge samples indicate variable degrees of alteration. Most of the NWHR lavas (20/25) have LOI < 2% (Table 2). One of the three oldest samples from Daikakuji has a LOI of 4.44 wt. % and moderate discoloration of the matrix and material (Table 1, Appendix 1). The Unnamed Seamount samples show little alteration; however, their high vesicularity and zeolite-lined vesicles may be the source of the > 2 wt. % LOI (Table 1, Appendix 1). The Pioneer sample has the highest LOI of 4.87 wt. %. This sample's matrix is hyalopilitic and discolored

with clays lining vesicles and is the most likely source of the high LOI (Table 1, Appendix 1). The high LOI from the Nīhoa sample (NIH-F-9) contradicts the petrographic inspection for alteration. This sample has only minor alteration of olivine phenocrysts, well preserved matrix material and no secondary mineralization within vesicles (Table 1, Appendix 1). The K/P in the NWHR tholeiitic lavas ranges from 0.33 to 2.32 and 1.4 to 1.8 for Kaua‘i tholeiites (Table 2). Eight of the tholeiitic lavas have K/P < 1, indicating loss of K_2O (Table 2).

TABLE 2. WHOLE-ROCK X-RAY FLUORESCENCE ANALYSES FOR NWHR LAVAS

Seamount	Sample	SiO_2	TiO_2	Al_2O_3	Fe_2O_3*	MnO	MgO	CaO	Na_2O	K_2O	P_2O_5	Total	LOI	K/P	Lab
Daikakuji	A-55-1	51.05	2.50	12.54	12.21	0.17	8.66	9.15	2.31	0.87	0.40	99.86	1.93	2.17	UM
	A-55-2	47.05	2.96	14.57	14.49	0.17	5.71	10.87	2.43	0.78	1.37	100.35	4.44	2.32	UM
	A-55-4	51.67	2.92	13.54	11.77	0.16	6.65	8.90	2.82	1.32	0.58	100.32	1.86	2.28	UM
Unnamed	84-28-C	43.94	2.55	13.94	12.99	0.19	7.87	14.50	2.02	1.03	0.96	100.00	2.72	1.08	UM
	84-28-D	43.86	2.58	13.89	13.06	0.19	8.04	14.81	1.88	0.98	1.02	100.31	2.63	0.96	UM
Academician Berg	72-20-GG	45.34	2.97	12.40	14.60	0.17	12.80	8.80	2.26	0.37	0.49	100.20	1.77	0.76	UM
Pioneer	P5-526-rk2**	44.35	3.23	11.98	16.04	0.22	11.65	10.41	1.11	0.74	0.22	99.95	4.87	3.29	UH
Gardner	76-6-7-B**	47.61	1.78	10.93	12.48	0.18	16.09	9.10	1.73	0.13	0.17	100.20	1.48	0.76	UM
	76-6-7-C**	47.31	1.78	11.03	12.53	0.18	15.42	9.21	1.75	0.18	0.17	99.55	1.55	1.05	UM
	76-6-7-F**	47.19	1.72	10.79	12.64	0.18	16.73	8.91	1.70	0.13	0.17	100.15	1.17	0.75	UM
	76-6-7-H	47.86	2.03	12.30	12.35	0.20	12.11	10.30	2.06	0.37	0.20	99.77	1.01	1.82	UM
	76-6-7-I	48.04	2.00	11.97	12.22	0.20	12.98	10.15	1.52	0.34	0.20	99.61	1.38	1.70	UM
	76-6-7-J	47.86	1.86	11.50	12.58	0.19	14.92	9.47	1.56	0.15	0.18	100.26	1.87	0.82	UM
Mokumanamana	NEC-2A	45.09	2.26	8.37	15.04	0.22	18.37	8.40	0.93	0.33	0.72	99.73	1.34	0.46	UM
	NEC-3A**	46.38	2.29	9.43	14.04	0.18	17.04	8.34	1.31	0.45	0.50	99.95	1.79	0.89	UM
Twin Banks	P5-688-1**	43.54	1.99	9.93	14.52	0.19	16.24	10.27	1.48	0.21	1.38	99.75	1.33	0.16	UH
West Nīhoa	76-9-11**	45.79	2.49	10.45	14.22	0.20	16.24	7.20	2.11	0.68	0.37	99.75	1.33	1.86	UM
Nīhoa	NIH-D-1-2**	47.57	2.58	9.89	13.34	0.17	15.37	7.77	2.05	0.63	0.37	99.73	0.42	1.69	UM
	NIH-D4	48.10	2.32	11.20	13.00	0.17	13.65	8.87	1.98	0.28	0.29	99.85	0.62	0.96	UM
	NIH-F-5A	44.58	1.60	7.86	14.33	0.18	24.02	5.71	0.99	0.10	0.32	99.69	1.33	0.33	UM
	NIH-F-9**	46.28	1.87	8.90	13.02	0.17	20.45	7.21	1.61	0.21	0.31	100.03	3.49	0.68	UM
	NIH-W-11-1	44.21	1.96	7.80	14.43	0.19	23.03	6.43	1.44	0.19	0.33	100.01	0.53	0.58	UM
Kauaʻi	KV04-16**	47.40	2.15	10.05	12.83	0.17	17.54	7.48	1.73	0.38	0.26	99.99	0.20	1.44	UM
	KV04-19**	50.40	2.37	12.75	11.96	0.17	9.89	9.70	2.20	0.43	0.26	100.12	0.06	1.63	UM
	KV04-22**	50.12	2.28	12.44	12.33	0.17	10.49	9.65	2.01	0.44	0.24	100.16	0.10	1.84	UM

Note: Major elements are in weight percent; LOI — Loss on ignition; Fe_2O_3*—total iron; ** from Garcia et al. (2010) for Kauaʻi, Garcia et al. (2015) for NWHR lavas. Sample preparation methods are similar to Greene et al. (2013; Appendix Section 2). Lab — laboratory for XRF analysis. UM — These lavas plus the nine previously reported samples were analyzed at the University of Massachusetts XRF facilities (for analytical procedures and precision, see Rhodes and Vollinger, 2004). Two samples labeled with the P5- prefix were previously analyzed for major and trace element compositions at University of Hawaiʻi at Mānoa (UH; for analytical procedures and precision, see Sinton et al., 2005).

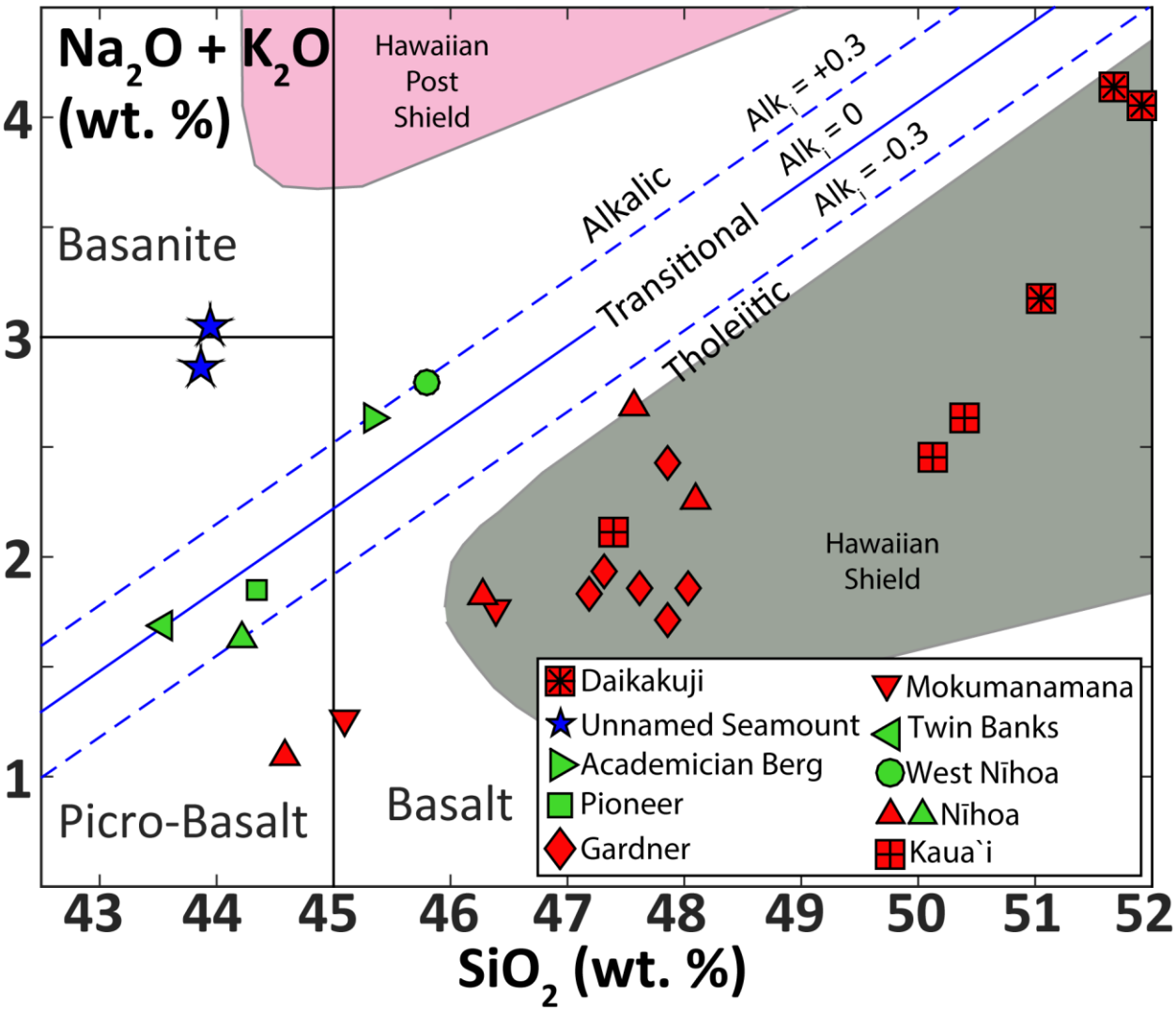

Figure 3. Whole-rock total alkalis versus silica plot (after Le Maître, 2002) for lavas from the NWHR and Kaua‘i from this study. The solid blue dividing line for separating alkalic from tholeiitic lavas is from Macdonald and Katsura (1964). This line is given by the function: $Alk_i = (SiO_2 - 39) * 0.37$, where Alk_i is a lava alkalinity index and SiO_2 is in wt. % (Carmichael et al., 1974, Rhodes and Vollinger, 2004). Shield stage lavas are defined here as having an alkalinity index $Alk_i < -0.3$ and symbols are red. Transitional stage lavas are green and plot on or within the array of the Macdonald-Katsura line (solid blue line) have an alkalinity index of 0 $Alk_i = 0.0 \pm 0.3$. Post-shield lavas are defined here as having $Alk_i > 0.3$, and symbols blue. The pink field represents the common post-shield lavas and the grey field represents shield lavas of Kilauea and Mauna Loa (Clague and Sherrod, 2014).

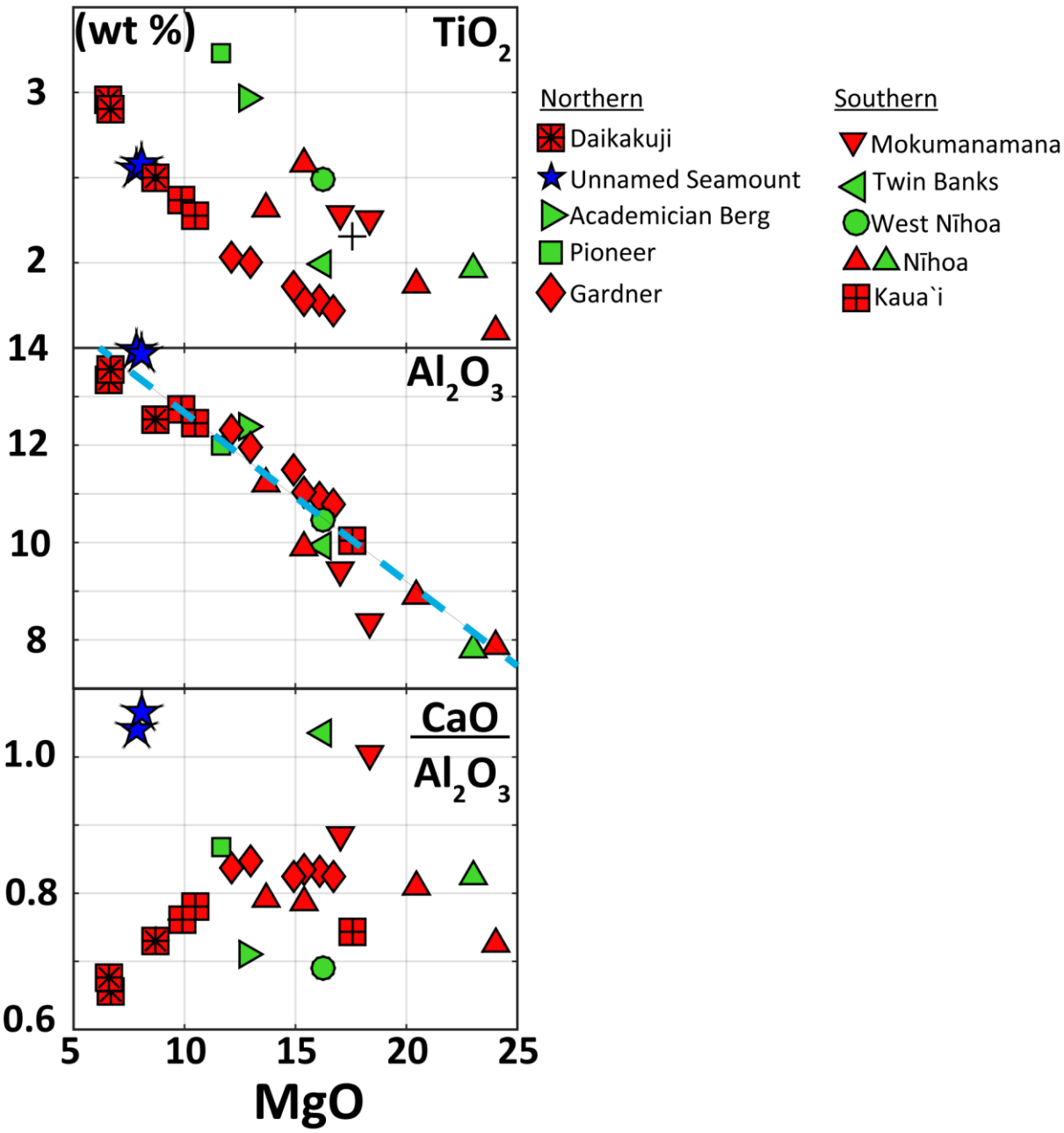

Figure 4. MgO variation plots for the lavas used in this study. Compositions are in weight percent. Most of the samples fall into well-defined arrays in TiO_2 as MgO decreases. There is no systematic relationship for these lavas in the TiO_2 arrays, though most transitional lavas plot higher TiO_2 for any given MgO. CaO/Al_2O_3 is highly variable with no apparent trends. Al_2O_3 increases steadily with decreasing MgO content indicating the plagioclase was not an important phase in their crystallization history. The dashed cyan line for MgO vs. Al_2O_3 is the trend line for Hawaiian lavas from Rhodes (2016). Two σ errors are smaller than the symbol size.

5) Olivine Chemistry and Calculation of Parental Magma Compositions

5.1) Olivine Electron Probe Micro Analysis (EPMA)

Analyses were made for 539 euhedral to subhedral olivine crystals in 25 samples (~20 olivine cores per sample) using the Electron Microprobe at the University of Hawai‘i at Mānoa with a high precision setup (200 nA, 20 keV; 10 µm beam diameter; Si, Mg, Ni, Ca, 100 s on peak, 45 s on both sides of the background; Mn, 60 s on peak, 30s on background; Fe, 30 s on peak, 15 s on background). High-intensity crystals were used to enhance count rates for Ni (LIFH) and Ca (PETH). Calibration standards were San Carlos olivine USNM 111312/444 (SiO_2, MgO, FeO), Verma Garnet (MnO), Kakanui Augite USNM 122142 (CaO), and a synthetic Ni-oxide (NiO). Raw X-ray intensities were converted into weight percent via ZAF corrections (Appendix Table A.2; Armstrong, 1988; Donovan, 2007).

The analytical set up yielded accurate and precise values based on the olivine standards San Carlos USNM 111312 444 and Spring Water USNM 2566 that were measured as unknowns during the analysis sessions (Table 3). Individual sessions showed lower standard deviations for each measured oxide when compared to the standard deviations calculated for the total distribution of measurements (Table 3). This gives high internal precision for each group of sample analyses measured within a session. The greater population standard deviation of all olivine analyses remains well within the variation tolerance needed to generate temperatures when used in further calculations.

Olivine forsterite contents (Fo) vary between 77.3 % (Kaua‘i, KV04-19) and 91.8 % (Gardner, 76-6-7-H; Figures 5 & 6). Lower Fo contents in olivine can be an artifact of not intersecting the core of the olivine (e.g., Pearce, 1984). Most samples range between $Fo_{82\text{-}88}$, except those from Gardner, which have abundant higher Fo olivines (Figure A.1). The $Fo_{91.8}$

from Gardner is the highest value measured in Hawaiian olivine (e.g. previous high, $Fo_{91.3}$ from Mauna Loa; Garcia et al. 1995).

The whole-rock compositions of the NWHR lavas have been affected by either olivine fractionation or accumulation (Figure 5). The most common graphical method to evaluate the extent of these processes is the Rhodes diagram (Rhodes et al. 1979; Figure 5). Olivines which are in equilibrium with the whole-rock Mg # lie within the equilibrium field defined by K_d = 0.345 ± 0.030 (Matzen et al., 2011). Samples from Daikakuji, the Unnamed Seamount, Academician Berg, Pioneer, Gardner, Twin Banks, and Kauaʻi plot above and left of the equilibrium field. These samples are assumed to have undergone olivine fractionation, lowering the whole-rock Mg # from the highest measured Fo equilibrium value. Samples from Mokumanamana, West Nīhoa, Nīhoa, and one sample from Kauaʻi plot below and to the right of the equilibrium field. These samples are assumed to have accumulated olivine, raising the Mg # of the whole-rock composition above the equilibrium value.

5.2) Calculation of parental magma compositions

The parental magma composition that is in equilibrium with the highest olivine forsterite content measured was calculated to determine the maximum $T^{ol\text{-}liq}$ recorded in the NWHR samples for each volcano (Table 4). All olivine cores used in parental magma calculations have CaO ≥ 0.17 wt. %, indicating that they are magmatic in origin and not mantle xenocrysts (Stormer, 1973; Larson and Pederson, 2000). The samples that have apparently accumulated olivine have a small range in Fo content of < 6% (Figure 5). The small range in Fo content suggests that the median Fo olivine composition can be assumed to be representative of the average accumulated olivine composition. Parental magma compositions were estimated by removing small weight fractions (0.01 wt. %) of the median Fo olivine composition from the

XRF whole-rock composition. This process was iterated until the parental magma Mg# was in equilibrium with the highest Fo measured within the sample (Table 5). Three potential parental magma compositions per sample are calculated assuming three K_d values (0.315, 0.345, and 0.375) spanning the equilibrium range reported by Matzen et al. (2011). These parental magma compositions are used to constrain the variation in possible parental magma compositions in a Monte Carlo simulation to calculate olivine-liquid and derive mantle potential temperatures.

Other samples were affected by variable olivine fractionation (Figure 5). Parental magma compositions were obtained by reverse olivine fractionation modeling using Petrolog V3.1.1.3 (Danyushevsky and Plechov, 2011). Equilibrium olivine was added in small steps (0.01 vol. %) to the whole-rock compositions until equilibrium with the highest % Fo was achieved, assuming three constant K_d values (0.315, 0.345, and 0.375). The amount of Fe_2O_3 in the melt was calculated assuming an oxygen fugacity fO_2 of QFM -1 (Rhodes and Vollinger, 2004) using the model of Kress and Carmichael (1988). Calculations were made under isobaric conditions of 1 kbar, ~3 km, a reasonable depth for a Hawaiian tholeiitic magma reservoir (Decker 1987 for Mauna Loa and Kīlauea; Poland et al. 2014 for Kīlauea).

One major assumption of this reconstruction of parental magmas is that the K_d value is constant during the course of these calculations. Recent research, however, suggests that this may not be true, and that K_d is compositionally dependent and not constant while reverse fractionation is taking place (e.g. Toplis 2005). To explore this alternative, the K_d was calculated as the magma composition was being estimated during each iterative step of the parental magma calculation using the equation of Toplis (2005). Parental magma compositions were estimated using Petrolog V3.1.1.3 (Danyushevsky and Plechov, 2011) to equilibrate with the high Fo olivine in two samples (A-55-1 and 76-6-7-H) that yielded the minimum and maximum

temperatures to explore the magnitude of change in the maximum temperature difference. The same parameterization was used for all other variables and K_d was allowed to vary. This method yielded similar final K_d values that are in agreement with the K_d=0.345±0.030 assumption (Table 6). The parental magma compositions for the 76-6-7-H sample from Gardner are less similar to the results obtained from a constant K_d than the parental magmas calculated for Daikakuji. This difference in final parental magma composition results in a minor 23 ºC difference in $T^{ol\text{-}liq}$ for the 76-6-7-H sample (Table 6). $T^{ol\text{-}liq}$ values obtained using the parental magma composition from the compositionally-dependent K_d method are within the 2σ uncertainty discussed in the next section.

TABLE 3. OLIVINE ELECTRON PROBE MICRO ANALYSIS REPRODUCIBILITY

Published standards			SiO_2		FeO		NiO		MnO		MgO		CaO		Total	Fo
NMNH 11312-444	SC		40.81		9.55		0.370		0.140		49.42		0.050		100.29	90.221
USNM 2566	SW		38.95		16.62		0.000		0.300		43.58		0.000		99.47	82.379
Sample Group		n	μ	σ	μ	σ	μ	σ	μ	σ	μ	σ	μ	σ		
A-55-1 A-55-2	SC	12	40.91	0.21	9.56	0.04	0.3616	0.0020	0.1378	0.0032	49.51	0.16	0.0721	0.0022	100.55	90.231
	SW	12	39.77	0.11	16.68	0.04	0.0010	0.0010	0.3107	0.0030	43.98	0.07	0.0000	0.0000	100.75	82.457
A-55-4 84-28-C 84-28-D	SC	21	40.75	0.18	9.59	0.05	0.3478	0.0026	0.1358	0.0036	49.29	0.23	0.0701	0.0012	100.18	90.166
	SW	23	39.53	0.17	16.68	0.04	0.0004	0.0007	0.3082	0.0035	43.92	0.05	0.0000	0.0000	100.43	82.442
P5-526-2 72-20-GG 76-6-7-B 76-6-7-F 76-6-11 P5-688-1	SC	56	40.20	1.87	9.54	0.29	0.3705	0.0047	0.1365	0.0040	49.17	1.32	0.0716	0.0025	99.49	90.184
	SW	54	39.13	0.21	16.70	0.05	0.0006	0.0008	0.3091	0.0045	43.75	0.05	0.0000	0.0000	99.89	82.364
76-6-7-H 76-6-7-I 76-6-7-J	SC	19	40.45	0.13	9.55	0.02	0.3703	0.0028	0.1373	0.0027	49.40	0.19	0.0729	0.0015	99.99	90.214
	SW	19	39.34	0.13	16.71	0.03	0.0005	0.0009	0.3092	0.0037	43.84	0.14	0.0000	0.0000	100.19	82.389
NEC-2A NEC-3A	SC	9	40.75	0.14	9.55	0.03	0.3628	0.0028	0.1352	0.0025	49.26	0.03	0.0725	0.0027	100.13	90.196
	SW	9	39.50	0.09	16.67	0.04	0.0013	0.0016	0.3011	0.0046	43.75	0.05	0.0000	0.0000	100.22	82.389
76-6-7-C NIH-D-1-2 NIH-D4 NIH-F-5A NIH-F9 NIH-W-11	SC	30	40.09	1.17	9.45	0.09	0.3683	0.0043	0.1349	0.0035	49.29	0.12	0.0707	0.0028	99.40	90.292
	SW	25	38.66	1.28	16.52	0.12	0.0006	0.0009	0.3034	0.0049	43.67	0.13	0.0000	0.0000	99.16	82.499
KV04-16, 19, 22	SC	20	40.43	0.23	9.61	0.02	0.3393	0.0019	0.1369	0.0031	49.68	0.10	0.0733	0.0009	100.27	90.211
	SW	20	39.27	0.25	16.79	0.02	0.0011	0.0011	0.3112	0.0034	44.20	0.04	0.0000	0.0000	100.57	82.439
SUMMARY	SC	167	40.40	1.20	9.54	0.20	0.363	0.012	0.136	0.004	49.30	0.80	0.072	0.002	99.83	90.217
	SW	172	39.2	0.60	16.70	0.10	0.001	0.001	0.308	0.005	43.80	0.20	0.000	0.000	100.04	82.422

Note: Summary of the mean (μ) and standard deviation (σ) for the number of analyses (n) run on the two standards of San Carlos (SC; NMNH 11312-444) and Springwater (SW; USNM 2566) olivine. Oxide compositions are in weight percent. The San Carlos and the Spring Water olivine compositions are from Jarosewich, et al. (1980); Fo – Percent forsterite. Samples are grouped based on the analysis session that the calibration represents (i.e., day they were analyzed). Within each group of analyses, the samples are ordered in ascending distance to Kilauea to best match their order in Table 1.

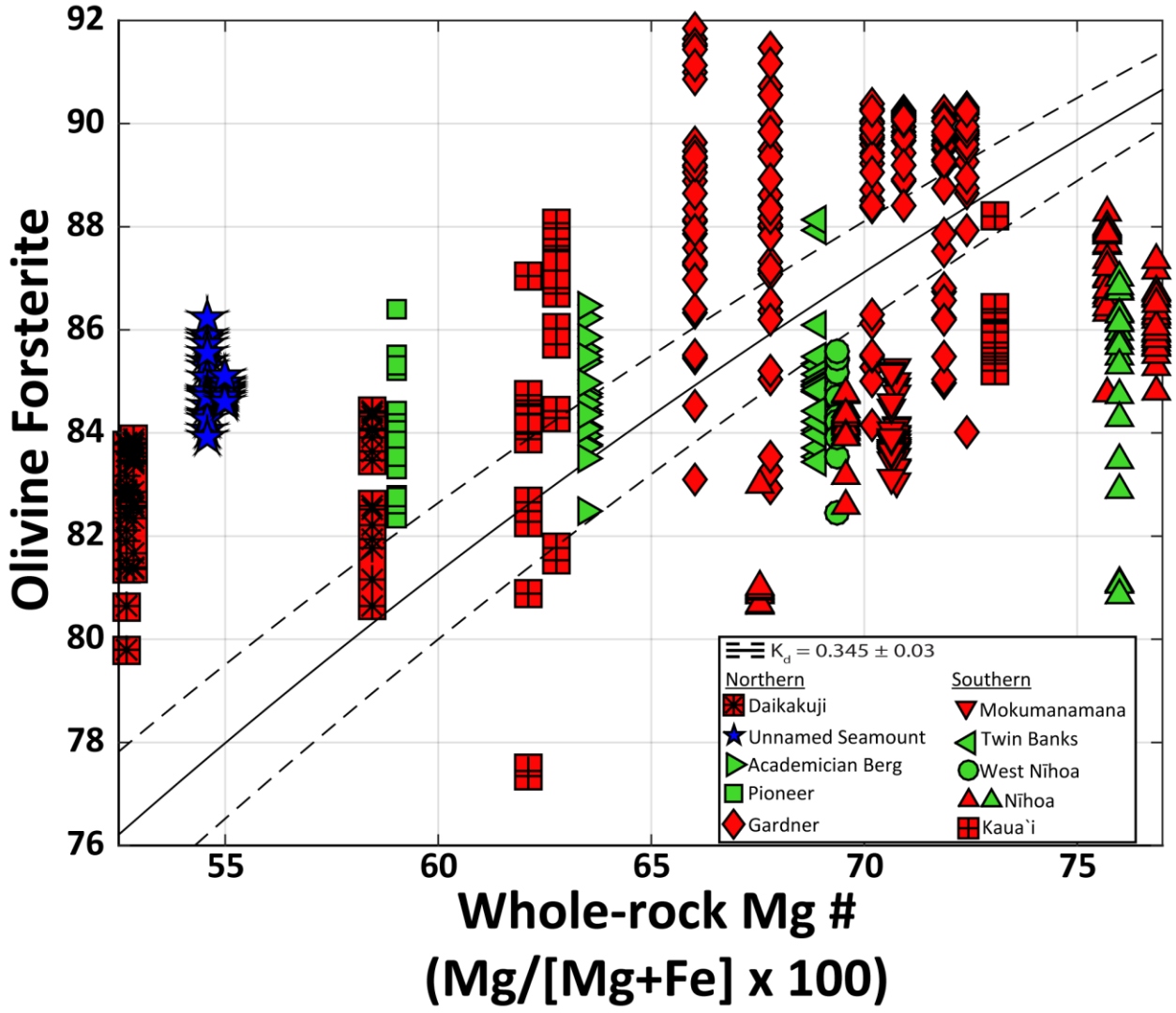

Figure 5. Rhodes diagram (Rhodes et al. 1979) of whole-rock Mg # (Mg # = mol % Mg/(Mg+Fe)); (FeO_t = 0. 9*Fe_2O_3) vs. olivine forsterite content to evaluate olivine compositions for NWHR lavas assuming the Fe-Mg exchange K_d = 0.345 ± 0.030 (1 σ = 0.009; Matzen et al., 2011).

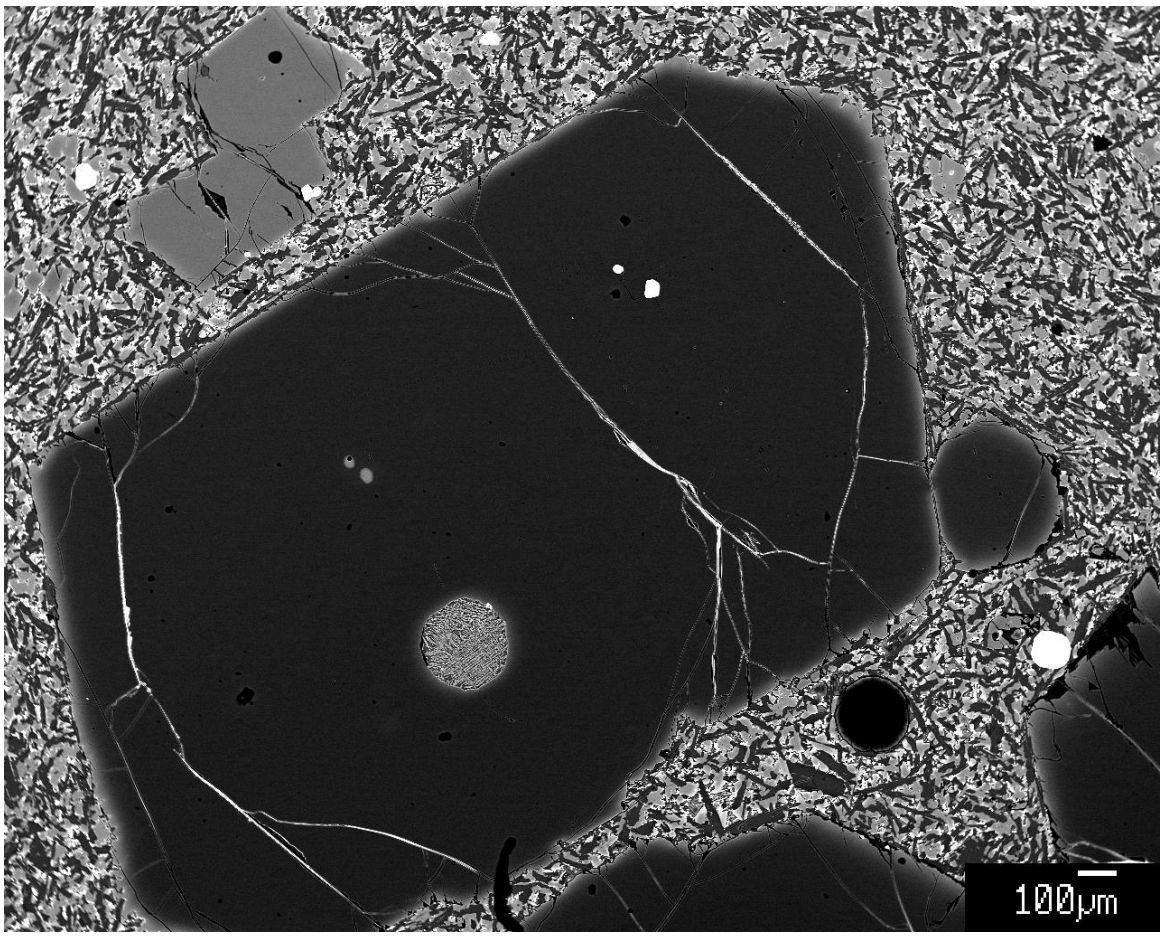

Figure 6. Backscatter electron image of the $Fo_{91.8}$ olivine measured in the 76-6-7-H sample. Note the minimal alteration around the Fe-rich rim and euhedral morphology of the crystal. Most of the phenocrysts in this section are darker gray while the microphenocrysts in the upper left of this image are lighter gray. Their light gray color indicates higher iron content.

TABLE 4. OLIVINE COMPOSTIONS FOR MAXIMUM FORSTERITE MEASURED FROM 25 NWHR LAVAS

Seamount	Sample	SiO_2	FeO	NiO	MnO	MgO	CaO	Total	Fo
Daikakuji	A-55-1(6)	39.64	14.50	0.47	0.17	44.08	0.19	99.05	84.42
	A-55-2(3)	39.75	15.22	0.45	0.19	44.19	0.19	99.98	83.81
	A-55-4(12)	39.25	15.08	0.42	0.18	44.05	0.19	99.16	83.89
Unnamed	84-28-C(17)	39.75	13.11	0.23	0.21	46.02	0.38	99.70	86.22
	84-28-D(20)	39.70	14.14	0.22	0.23	45.27	0.41	99.97	85.09
Academician Berg	72-20-GG(19)	39.89	13.01	0.35	0.17	46.68	0.18	100.29	86.48
Pioneer	P5-526-rk2(10)	39.70	13.01	0.38	0.17	46.34	0.22	99.81	86.40
Gardner	76-6-7-B(14)	40.41	9.54	0.40	0.14	49.44	0.22	100.15	90.24
	76-6-7-C(6)	40.55	9.44	0.39	0.13	49.09	0.21	99.81	90.26
	76-6-7-F(27)	40.50	9.47	0.41	0.14	49.53	0.22	100.25	90.31
	76-6-7-H(11)	40.27	7.95	0.45	0.12	50.25	0.21	99.25	91.85
	76-6-7-I(27)	40.26	8.32	0.45	0.12	49.98	0.22	99.36	91.46
	76-6-7-J(30)	40.26	9.31	0.40	0.14	49.04	0.22	99.37	90.37
Mokumanamana	NEC-2A(18)	39.53	14.01	0.27	0.19	45.48	0.27	99.74	85.26
	NEC-3A(2)	39.55	13.97	0.27	0.19	45.17	0.21	99.36	85.21
Twin Banks	P5-688-1(20)	40.17	11.48	0.40	0.15	47.91	0.17	100.29	88.15
West Nīhoa	76-9-11(10)	39.58	13.74	0.31	0.18	45.77	0.24	99.82	85.59
Nīhoa	NIH-D1-2(1)	36.82	14.68	0.33	0.18	44.73	0.21	96.95	84.45
	NIH-D4(12)	38.76	17.77	0.29	0.22	42.04	0.23	99.30	80.83
	NIH-F-5A(9)	39.66	12.09	0.40	0.16	46.85	0.19	99.35	87.36
	NIH-F-9(4)	39.87	11.25	0.39	0.15	47.45	0.20	99.31	88.26
	NIH-W-11-1(6)	40.02	12.39	0.38	0.16	46.60	0.20	99.75	87.02
Kauaʻi	KV04-16(01)	40.19	11.46	0.35	0.16	48.11	0.18	100.45	88.21
	KV04-19(01)	39.72	12.52	0.39	0.16	47.17	0.20	100.16	87.04
	KV04-22(15)	40.04	11.62	0.40	0.16	48.10	0.18	100.49	88.06

Note: Olivine compositions are in weight percent. The number within the parentheses after the sample name corresponds to the olivine measurement number in all of the measured olivine compositions (i.e. sample # (olivine measurement #; Appendix Table A.2). Fo is mol % forsterite.

TABLE 5. PARENTAL MAGMA COMPOSITIONS IN EQUILIBRIUM WITH HIGHEST FO OLIVINE AT $K_d = 0.345$

Seamount	Sample	SiO_2	TiO_2	Al_2O_3	Fe_2O_3	FeO	MnO	MgO	CaO	Na_2O	K_2O	P_2O_5
Daikakuji	A-55-1	50.96	2.38	11.92	1.10	10.43	0.16	10.94	8.70	2.20	0.83	0.38
	A-55-2	50.97	2.68	12.06	1.12	10.37	0.15	10.34	8.14	2.48	1.18	0.51
	A-55-4	50.74	2.64	12.25	1.12	10.38	0.14	10.40	8.05	2.55	1.19	0.52
Unnamed	84-28-C	43.62	2.20	11.73	1.33	11.37	0.18	13.76	12.50	1.58	0.86	0.88
	84-28-D	43.38	2.32	12.37	1.34	11.29	0.20	12.46	13.69	1.59	0.77	0.58
Academician Berg	72-20-GG	45.68	2.83	11.41	1.29	12.21	0.16	15.07	8.38	2.15	0.35	0.47
Pioneer	P5-526-rk2	44.31	2.82	10.46	1.39	13.44	0.19	16.51	9.09	0.97	0.65	0.19
Gardner	76-6-7-B	47.59	1.68	10.32	1.10	10.27	0.17	18.37	8.59	1.63	0.12	0.16
	76-6-7-C	47.46	1.66	10.27	1.11	10.36	0.17	18.46	8.57	1.63	0.17	0.16
	76-6-7-F	47.27	1.64	10.27	1.11	10.40	0.17	18.76	8.48	1.62	0.12	0.16
	76-6-7-H	46.50	1.52	9.24	1.09	10.00	0.15	21.79	7.73	1.55	0.28	0.15
	76-6-7-I	47.09	1.60	9.60	1.06	10.00	0.16	20.71	8.14	1.22	0.27	0.16
	76-6-7-J	47.45	1.67	10.32	1.08	10.33	0.17	18.77	8.50	1.40	0.13	0.16
Mokumanamana	NEC-2A	45.88	2.55	9.41	1.69	13.47	0.22	15.13	9.42	1.05	0.37	0.81
	NEC-3A	47.17	2.55	10.52	1.57	12.36	0.18	13.88	9.27	1.46	0.5	0.56
Twin Banks	P5-688-1	44.14	1.97	9.82	1.33	12.04	0.19	17.33	10.16	1.46	0.21	1.36
West Nīhoa	76-9-11	46.28	2.64	11.10	1.51	12.73	0.20	14.54	7.63	2.24	0.73	0.39
Nīhoa	NIH-D-1-2	48.52	2.81	10.77	1.45	11.77	0.17	12.75	8.44	2.23	0.68	0.40
	NIH-D4	49.17	2.58	12.46	1.45	11.04	0.16	10.47	9.84	2.20	0.31	0.32
	NIH-F-5A	46.31	2.11	10.38	1.89	12.75	0.18	17.03	7.47	1.31	0.14	0.42
	NIH-F-9	45.96	2.00	9.83	1.79	12.79	0.18	18.57	7.09	1.24	0.13	0.40
	NIH-W-11-1	46.44	2.87	11.38	2.10	10.82	0.17	14.03	9.34	2.10	0.27	0.47
Kaua‘i	KV04-16	47.59	2.20	10.31	1.32	11.55	0.17	16.77	7.67	1.77	0.39	0.27
	KV04-19	49.87	2.18	11.71	1.07	10.16	0.16	13.21	8.91	2.02	0.39	0.24
	KV04-22	49.38	2.03	11.09	1.19	10.37	0.15	14.80	8.60	1.79	0.39	0.21

Note: Compositions are normalized to 100%. Parental magmas are reported for $K_d = 0.345$ because this value is assumed to be representative of the average parental magma compositions in all later steps for Monte Carlo simulations and temperature calculations.

TABLE 6A. PARENTAL MAGMA COMPOSITION USING CONSTANT K_d DURING OLIVINE ADDITION

Seamount	Sample	K_d	SiO_2	TiO_2	Al_2O_3	Fe_2O_3	FeO	MnO	MgO	CaO	Na_2O	K_2O	P_2O_5
Daikakuji	A-55-1	0.345	50.96	2.38	11.92	1.10	10.43	0.16	10.94	8.70	2.20	0.83	0.38

PARENTAL MAGMA COMPOSITION USING K_d CALCULATED USING THE EQUATION OF TOPLIS (2005)

Seamount	Sample	K_d	SiO_2	TiO_2	Al_2O_3	Fe_2O_3	FeO	MnO	MgO	CaO	Na_2O	K_2O	P_2O_5
Daikakuji	A-55-1	0.353	50.85	2.35	11.81	1.11	10.48	0.16	11.24	8.62	2.18	0.82	0.38

Temperature Results	P (GPa)*	$T^{ol\text{-}liq}$ (°C)
Constant at 0.345	3.00	1425
Not Constant; Calculated using Toplis (2005)	3.00	1433

TABLE 6B. PARENTAL MAGMA COMPOSITION USING CONSTANT K_d = 0.345 DURING OLIVINE ADDITION

Seamount	Sample	K_d	SiO_2	TiO_2	Al_2O_3	Fe_2O_3	FeO	MnO	MgO	CaO	Na_2O	K_2O	P_2O_5
Gardner	76-6-7-H	0.345	46.50	1.52	9.24	1.09	10.00	0.15	21.79	7.73	1.55	0.28	0.15

PARENTAL MAGMA COMPOSITION USING K_d CALCULATED USING THE EQUATION OF TOPLIS (2005)

Seamount	Sample	K_d	SiO_2	TiO_2	Al_2O_3	Fe_2O_3	FeO	MnO	MgO	CaO	Na_2O	K_2O	P_2O_5
Gardner	76-6-7-H	0.323	46.80	1.60	9.71	1.09	10.01	0.16	20.42	8.13	1.63	0.29	0.16

Temperature Results	P (GPa)*	$T^{ol\text{-}liq}$ (°C)
Constant at 0.345	3.00	1605
Not Constant; Calculated using Toplis (2005)	3.00	1582

*Pressure of 3.00 GPa is the value used when calculating the $T^{ol\text{-}liq}$ in Eqn. 1, not the pressure value (1 kbar) used in parental magma calculations which was the same condition during both simulations

7) Olivine Liquid and Mantle Potential Temperatures

7.1) Monte Carlo simulation methods

A Monte Carlo approach was used to estimate the olivine-liquid and mantle potential temperatures. Details on the Monte-Carlo model can be found in Appendix 3. This method allows for easy quantification of uncertainties during calculation of $T^{ol\text{-}liq}$ and T_p. Olivine-liquid temperatures ($T^{ol\text{-}liq}$) reflect the temperature at which the maximum Fo olivine phenocryst is in equilibrium with the calculated parental magmas. Olivine liquid temperatures were calculated using the thermometer of Putirka et al. (2007; Eqn. 1, Appendix 3). The $T^{ol\text{-}liq}$ value is then used as an input for the mantle potential temperature (T_p) correction. The T_p correction accounts for the change in temperature due to fusion (ΔT_{fus}) and then decompression along an adiabat to the surface ($P\frac{\partial T}{\partial P}$; Putirka, 2016; Eqn. 4, 6-8; Appendix 3). The 2σ uncertainties in temperatures are the product of propagated uncertainties from (1) the variance in analytical measurements of olivine using EPMA, (2) the range in K_d that is assumed when finding parental magma compositions, and (3) the assumptions made for the melting conditions (melt fraction and pressure) when correcting for the mantle potential temperature (Appendix 3).

7.2 Sensitivity of calculated olivine-liquid temperature to alteration

Chemical alteration and removal of certain major elements can artificially increase values of $T^{ol\text{-}liq}$ by reducing the network forming and network modifier variables in the thermometer (Appendix 3). Lipman et al. (1990) showed removal of the major elements SiO_2, CaO, K_2O, and Na_2O in highly altered tholeiitic basalts from Mauna Loa. To assess the sensitivity of the calculated $T^{ol\text{-}liq}$ to chemical alteration, fractions of SiO_2, CaO, K_2O, and Na_2O were removed from an original composition in iterative steps, and the $T^{ol\text{-}liq}$ was recalculated. The degree of alteration simulated in these calculations would have resulted in obvious petrographic indicators such as complete

discoloration of the matrix and replacement of olivine by clays. This high level of alteration was not acceptable for this study (Table 1). Removing 20 iterations (1 wt.% of each oxide / iteration) of the original composition of CaO, K_2O, and Na_2O resulted in a ~2 ^oC increase in the calculated $T^{ol\text{-}liq}$ (Figure 7). Temperature changes ≤ 52 ^oC, the standard estimate of error from calibration of the thermometer by Putirka et al. (2007), cannot be resolved. Olivine liquid temperatures are most sensitive to the removal of SiO_2. Removing 10% of the original SiO_2 content resulted in a $T^{ol\text{-}liq}$ increase of ~ 23 ^oC (Figure 7). This sensitivity analysis gives confidence that even in the moderately altered rocks of this suite, the calculated temperatures remain within the 2σ uncertainty in $T^{ol\text{-}liq}$ and T_p that is derived from uncertainty in analytical measurement or valid ranges in parental magma compositions.

7.3) Olivine-liquid and mantle potential temperature results

The $T^{ol\text{-}liq}$ range for volcanoes with multiple samples is 3 ^oC (Unnamed Seamount) to 160 ^oC (Nīhoa). Only one suitable sample per volcano was identified for Academician Berg, Pioneer, Twin Banks, and West Nīhoa within the UH collection. Thus, temperature ranges and inter-sample variability cannot be assessed for these volcanoes. The $T^{ol\text{-}liq}$ and the consequent T_p for these locations are interpreted as maxima in all further discussion, though higher temperatures are possible.

The two approaches used to calculate the $T^{ol\text{-}liq}$ of these lavas used a constant pressure of 3.00 ± 0.15 GPa similar to the approach used by Putirka et al., (2007) as well as the calculated pressure from a Si-activity barometer (Putirka, 2008; Eqn. 2 and 3, Appendix 3). The range in maximum $T^{ol\text{-}liq}$ between volcanoes using the constant pressure was 1425 ± 28 ^oC from Daikakuji to 1605 ± 30 ^oC at Gardner (2σ uncertainty; Appendix Table A.1). Correcting $T^{ol\text{-}liq}$ to T_p using melt fractions of 8-24% yields a maximum difference in T_p of 197 ^oC between Daikakuji and Gardner

(Figure 8; Appendix Table A.1). The calculated pressures from the barometer varied between 1.16 GPa and 3.21 GPa from Daikakuji to Gardner (Figure 8; Appendix Table A.1). Using the calculated pressures produces an even larger $T^{ol\text{-}liq}$ difference between Daikakuji and Gardner (279ºC, Appendix Table A.1). Correcting these $T^{ol\text{-}liq}$ for T_p using the values from the barometer with calculated melt fractions (Appendix Table A.1), a 329 ºC range was found in T_p (1374 ± 34 ºC for Daikakuji to 1703 ± 56 ºC for Gardner; Table 7). The maximum T_p for Gardner is slightly higher but not statistically different than the 1690 ºC estimates for Mauna Loa (Putirka et al. 2010, which used similar values when correcting for T_p).

The NWHR lavas reveal two regional trends of increasing T_p (Figure 8). Potential temperatures gradually increase from 1374 ºC at Daikakuji (near the HEB), peaking at 1703 ºC for Gardner. This trend, however, includes two volcanoes with only one sample to estimate T_p (Academician Berg and Pioneer). The T_p decreases for the NWHR volcanoes southeast of Gardner (Mokumanamana to Nīhoa). Potential temperatures range between 1517 ºC for West Nīhoa to 1632 ºC for Nīhoa for this section and do not show any systematic trend (Figure 8; Table 7). The second increase begins in the main Hawaiian Islands with the T_p of 1567 ºC for Kaua‘i rising to the current 1690 ºC T_p estimate of Mauna Loa (Figure 8; Table 7) .

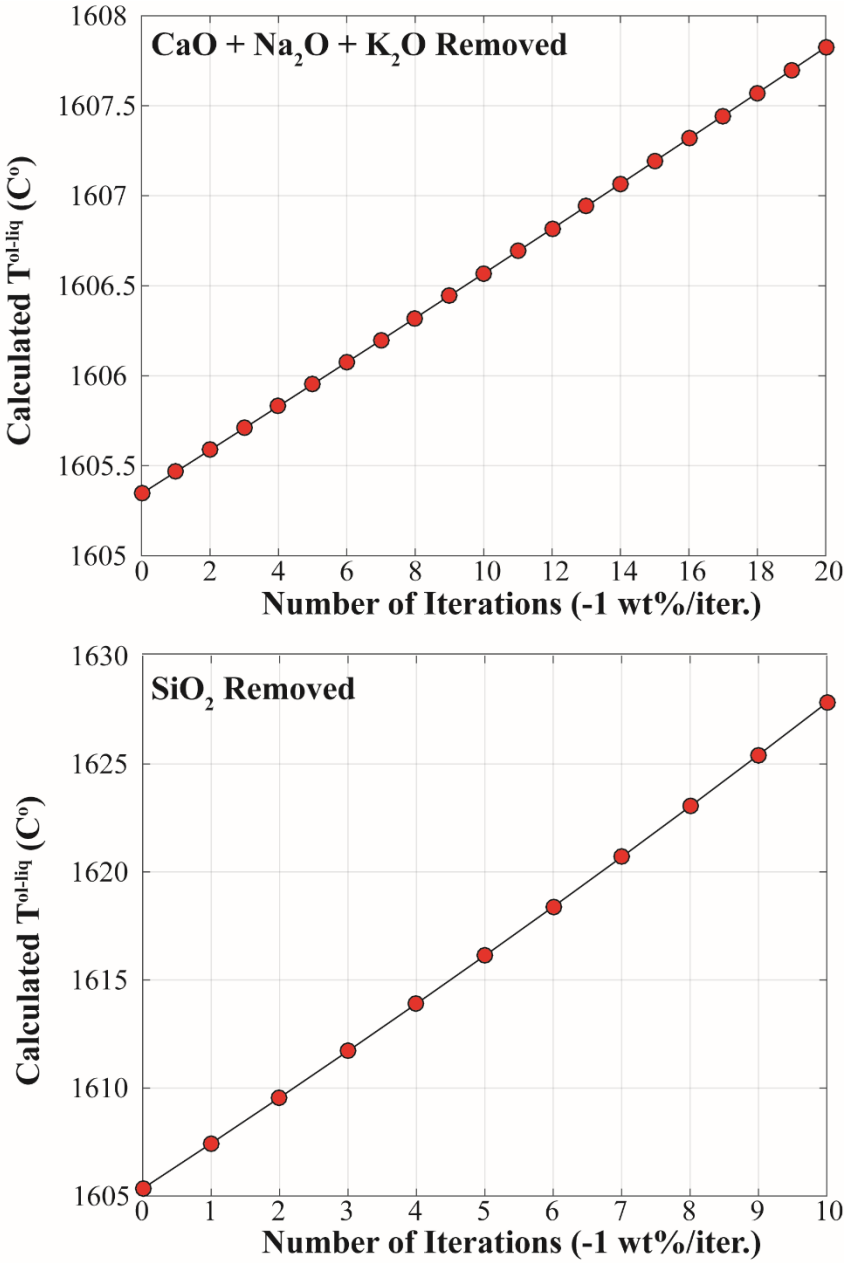

Figure 7. Plots showing the sensitivity of olivine-liquid temperatures to chemical alteration. The largest increase in the calculated temperature (~23 ºC) results from alteration SiO2 content. Combined with the minor 2º increase from removing the other alteration sensitive oxides, CaO, Na_2O, and K_2O, this level of weathering would result in an increase of ~25 ºC for any sample which is still within the 2σ uncertainties in the true calculated temperatures. This degree of weathering would have strong petrographic indicators of highly altered matrix and olivine phenocrysts, and thus, a sample with this degree of chemical alteration would not have been used in this study.

TABLE 7. MAXIMUM MANTLE POTENTIAL TEMPERATURE ESTIMATES FOR SELECTED NWHR VOLCANOES

Seamount	Sample	Distance to Mauna Loa (km)	Volcanic Volume (x 10 km^3)	Melt Flux (m^3s^{-1})	Pressure (GPa)	Melt Fraction	$\mu T^{ol\text{-}liq}$ (^oC)	1σ	μT_p (^oC)	1σ
Daikakuji	A-55-1	3395	3	0.68	1.16	0.12	1335	13	1374	24
Unnamed	84-28-D	2770	1	0.57	2.43	0.03	1458	15	1468	29
Academician Berg	72-20-GG	2580	8	1.24	2.46	0.12	1480	13	1509	27
Pioneer	P5-526-rk2	1970	15	2.55	2.66	0.15	1515	14	1557	29
Gardner	76-6-7-H	1420	54	4.76	3.21	0.24	1614	13	1703	28
Mokumanamana	NEC-2A	1050	13	3.00	1.94	0.16	1466	13	1521	25
Twin Banks	P5-688-1	890	5	2.11	2.86	0.16	1541	11	1587	22
West Nīhoa	76-9-11	790	9	2.28	2.11	0.20	1441	14	1517	27
Nīhoa	NIH-F-9	760	13	2.40	2.22	0.25	1527	13	1632	27
Kauaʻi	KV04-16	500	29	3.57	2.10	0.20	1489	10	1567	21

Note: Distance to Mauna Loa (M. Loa) was measured from the center of Mokuʻāweoweo Crater along a great circle to the center of each volcano. Volcanic Volume is from Bargar and Jackson (1974); Melt Flux is from Wessel (2016); Pressure (P) was calculated using the Si-activity barometer of Putirka (2008); Melt Fraction was calculated using the equations of Putirka (2016); $\mu T^{ol\text{-}liq}$ was calculated using the Olivine-liquid thermometer of Putirka (2007); μT_p was calculated using the formulation of Putirka (2016).

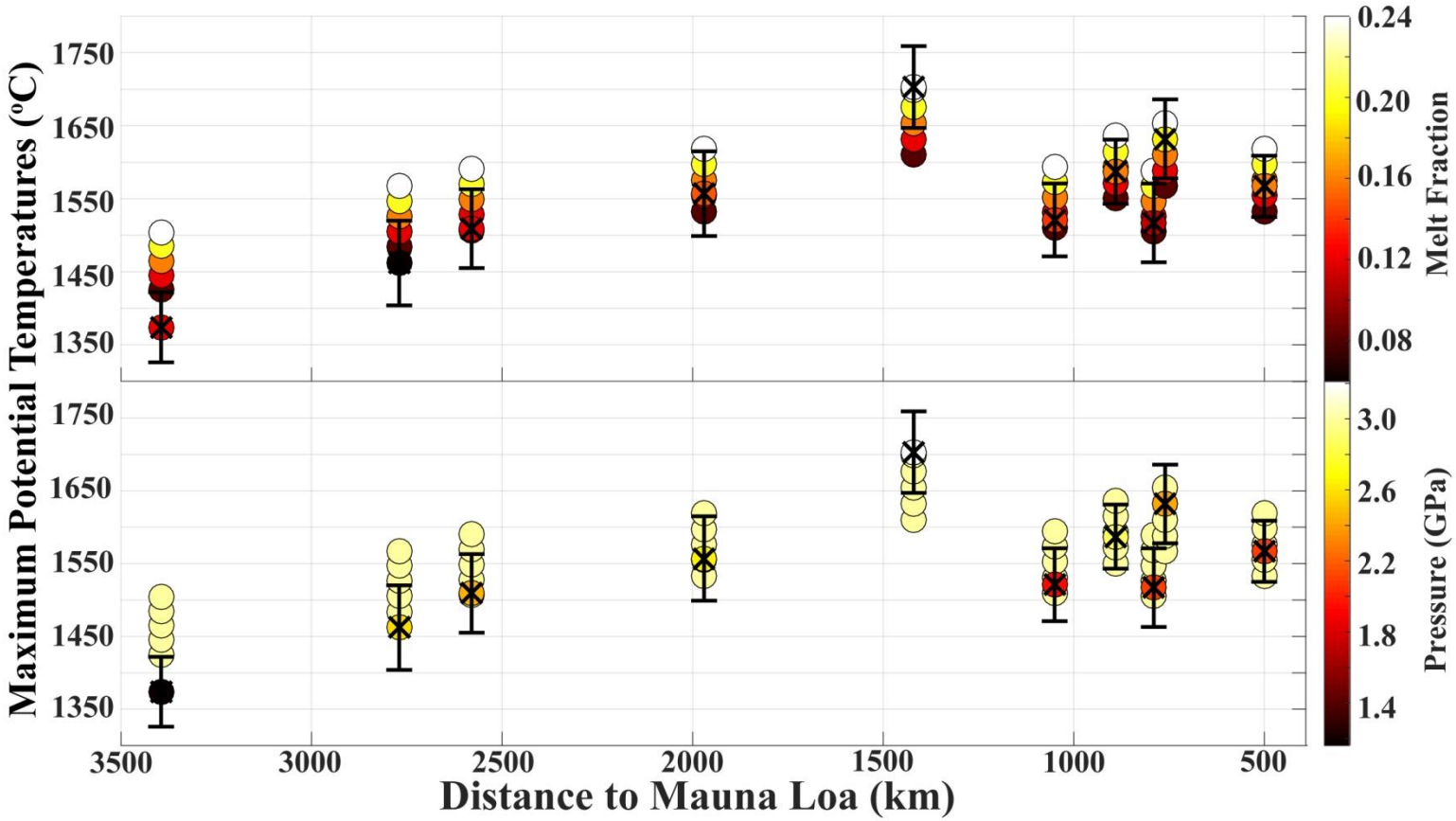

Figure 8. Plots of the maximum T_p calculated from each volcano using the parameterization summarized in the Appendix Table A.1. The circles without an x inside of them are results obtained by assuming a Pressure of 3.00 GPa and a range assumed melt fractions (minimum melt fraction from Norman and Garcia, 1999; maximum from Putirka et al. 2010). These symbols are colored to depict the variable results obtained from these assumptions. The circles with an x-symbol and error bars are the T_p estimates using Eqns. 2-8 to estimate pressure and melt fraction. The error bars mark the 2σ confidence interval about that estimate. Each circle is colored using the melt fraction and pressure values listed in Appendix Table A.1. Note that for each T_p estimated using Eqns 4-8, there is at least one other T_p estimate assuming a pressure of 3 GPa and some value of melt fraction that lie within the 2σ confidence interval.

8) Discussion

8.1) Comparison to previous estimates of T_p for Hawaiian volcanoes

The mantle potential temperature of the Hawaiian hotspot has been estimated using multiple approaches: geochemical and petrological modeling (e.g. Herzberg and Asimow, 2008, Lee et al. 2009, Putirka et al. 2010; Xu et al. 2014), seismic velocity modeling (e.g. Wolfe et al., 2011), and geodynamic modeling (e. g. Ballmer et al., 2013; Togia, 2015). These approaches gave a range of mantle potential temperature beneath Hawaii of ~1500-1700 ^{o}C (see Putirka et al. 2010). Values of T_p for older Hawaiian volcanoes (> 2Ma) were not known. New estimates from this study revealed only two NWHR volcanoes, Nīhoa and Gardner, have T_p estimates within the range found for the maximum T_p from volcanoes that make up the island of Hawaii (1632 ^{o}C $\geq T_p \geq$ 1690 ^{o}C, Figure 9; Putirka et al., 2010). The lower T_p for the NWHR volcanoes are similar to the 1550 ± 25 ^{o}C estimate for Mauna Kea lavas found by Herzberg and Asimow (2008) using a different thermometer and formulation of T_p.

These new estimates of plume temperature for NWHR volcanoes provides insight into Hawaiian plume dynamics. Variations in Hawaiian plume buoyancy flux can be attributed to changes in either the material flux (Q) or excess temperature ($T_{ex} = T_p^{hot\ spot} - T_p^{ambient} = \Delta T_p$) of the plume (Ribe and Christensen, 1999; Togia, 2015). The method used by Togia (2015) which sought to minimize error when reproducing the bathymetric swell shape resulted in non-unique solutions for estimating T_p and mass flux. Non-unique solutions from plume buoyancy flux modelling make estimating T_p difficult to decouple from estimates of mass flux. The T_p estimates using olivine thermometry from this study are independent of mass flux influences, are from volcanoes that represent large variations in volcanic volumes and consequently, large variation in swell shape on the surrounding seafloor. Thus, these new estimates of T_p can provide valuable constraints on the

excess temperatures of the NWHR and greatly improve the certainty of relative contributions of excess temperature and mass flux for modelling buoyancy of the Hawaiian mantle plume.

The total range in T_p for the NWHR is bound by two shield stage tholeiites from Daikakuji and Gardner (1374 ± 48 ^oC; 1703 ± 56 ^oC). No systematic variation between T_p and the alkalic index of lavas for these volcanoes (Figure 9). The T_p estimate for Gardner represents the highest current estimate for the Hawaiian mantle plume (e.g., Putirka et al., 2010). The parental magma of the Gardner lava yielded the highest calculated pressure and second highest melt fraction (P = 3.21 GPa; F = 24 %; Table 7). The next highest calculated pressure was from the Twin Banks (P = 2.86 GPa) and the highest calculated melt fraction was from Nīhoa (F = 25%). The T_p estimate for Nīhoa is the second highest for the NWHR (1632 ± 54 ^oC). The T_p estimate for Nīhoa is anomalously high for the southeastern portion of the NWHR (Figure 9 & 11). The T_p of Mokumanamana (1521 ± 50 ^oC), a volcano with similar volcanic volume to Nīhoa (13 x 10^3 km^3) is 111 ^oC cooler in T_p (Table 7). This potential temperature – volcanic volume discrepancy may indicate that the lower T_p estimates for the southeastern portion of the NWHR is an artifact from under sampling (i.e.: Twin Banks and West Nīhoa only had one sample to estimate T_p).

Daikakuji lavas have unradiogenic Pb, low εNd, and high $^{87}Sr/^{86}Sr$ isotopes (Regelous et al., 2003), which are characteristic of the Loa component (Weis et al., 2011). The denser pyroxenite component would have caused the plume to lose heat during a slower ascent before erupting these lavas (e.g. Ballmer et al., 2015). Lower $T^{ol\text{-}liq}$ is indicative of Loa-type primary magmas for Penguin Bank lavas (Xu et al., 2014). The $T^{ol\text{-}liq}$ range for Loa-type primary magmas was 1480-1520 ^oC (using the thermometer of Putirka et al. 2007) and a pressure range of 1.68-2.14 GPa (using the model of Lee et al. 2009; Xu et al., 2014). Their calculated pressures are 0.48 GPa to 0.95 GPa greater and their temperatures are 145 ^oC to 185 ^oC higher than the maximum pressure and $T^{ol\text{-}liq}$

measured for Daikakuji lavas (Table A.1). The lavas from the Unnamed seamount, Academician Berg, Pioneer, Mokumanamana, and West Nīhoa have $T^{ol\text{-}liq}$ <1520 ºC (Table 7). If maximum olivine-liquid temperatures are an indication of source components, the lower olivine-liquid temperatures from these NWHR volcanoes suggest the Loa-type component may be a significant source contribution to magma compositions for these volcanoes. New $^{208*}Pb/^{206*}Pb$ isotopic compositions of NWHR lavas with Loa-type components are consistent with the lower temperatures of West Nīhoa and Mokumanamana, however, it is inconsistent with the Kea-type isotopic compositions of the Unnamed seamount, Academician Berg, and Pioneer (Harrison et al., in review).

The two oldest seamounts have the lowest T_p (Unnamed seamount: 1468 ± 60 ºC and Daikakuji: 1374 ± 48 ºC; Table 7). Their potential temperatures are more similar to estimates of mid-ocean ridges (T_P^{MOR} 1454 ± 78 °C; e.g. Putirka et al., 2010; Table 7). The parental magma compositions of Daikakuji lavas (Table 7) resulted in the lowest calculated pressure depressing the magnitude of temperature increase when correcting for T_p. Higher pressure and melt fraction (i.e., P = 3.00 GPa, F = 24%) results in a T_p of 1504 ± 36 ºC, only 50 ºC higher than the average T_P^{MOR} estimates (Table A.1). No tholeiites were available from the Unnamed seamount in the NWHR sample suite; only a moderately altered, alkalic picro-basalt. The parental magma composition of the Unnamed seamount lava yielded the lowest calculated melt fraction (F = 3%; Table 7) and a pressure of 2.43 GPa using the Si-activity barometer, similar to pressure estimates for other NWHR volcanoes (Table 7). The low melt fraction for the Unnamed seamount lava resulted in only a 10 ºC increase in temperature when correcting $T^{ol\text{-}liq}$ to T_p (Table 7). The lower temperature may be the result of lower melting conditions for this volcano or a sampling artifact. Lavas from the Unnamed seamount and Daikakuji lack olivine phenocrysts, whereas all other olivine analyses were

conducted on phenocryst grains (Table 1). The lack of olivine phenocrysts in these samples could indicate that these samples are representative of shallow processes.

8.2) Correlation of T_p with time, melt flux and volcanic volume

Spearman's rank correlation coefficients were calculated to evaluate the significance of correlations between T_p and (1) distance from Mauna Loa, (2) the melt flux, and (3) volcanic edifice volume (Figure 10). This non-parametric one-sided correlation test uses the critical t-value of the student t-distribution of 95% ($t_{95\%}$). The hypothesis is that the two variables are not correlated, and have a correlation coefficient (ρ) equal to zero (Myers and Well, 2003). The correlation coefficient is used to calculate a corresponding t-value that is compared to the critical t-value from the student t-distribution to establish the level of confidence of the correlation. Therefore, if the calculated t-value obtained from the correlation coefficient is greater than the value of the 95% quantile of the t-distribution, we can reject the null hypothesis that the two variables are not correlated, and that the correlation coefficient is significant. Each of the three variables have t-values that are greater than the critical t-value at a 95% confidence level ($t_{95\%,9} = 1.83$). Thus, the null hypothesis that these variables share no correlation, can be rejected (Figure 10). These statistical results show that the correlation between these variables is real.

The thermal history derived from the calculation of T_p along the NWHR is in agreement with the temporal changes in melt flux (Figure 9). There are two sections of the NWHR that show increasing melt flux: between the HEB and Gardner, and Kauaʻi to Mauna Loa. Both instances of increasing melt flux are accompanied by increasing T_p. The 329 ^oC increase in T_p from Daikakuji to Gardner shows that T_p strongly correlates with melt flux between ~47 and 12 Ma (Figure 9). The T_p and melt flux decreased from Gardner to Nīhoa (Figure 9). The lower T_p of Kauai and marks the second increase in melt flux and T_p along the volcanoes of the main Hawaiian Islands (Figure 9).

The overall 329 ºC increase in T_p of since formation of the HEB to Gardner is greater than the 175-200 ºC increase in T_p needed sustain the melt flux increase along the NWHR predicted by White (1993; Figure 11). After the formation of Gardner, T_p decreases but still remains above the T_p predicted by White (1993) to sustain the melt production (Figure 11). The two instances of increasing T_p and melt flux for the Hawaiian plume contrasts markedly with the recent evidence for cooling and decreasing magma production trends at other hotspots. For example, T_p estimates from the Galápagos hotspot have decreased by 60-120 ºC since the Cretaceous (Herzberg and Gazel, 2009). Iceland has a similar history of cooling from T_p = 1520-1570 ºC in Cretaceous to 1460 ºC at present (e.g.: Herzberg and O'Hara, 2002, Herzberg et al., 2007). However, new estimates for the thermal history of Iceland suggest that the cooling trend only occurred from 60 Ma to 35 Ma. Since 35 Ma, the Iceland hotspot has been increased in T_p from 1314 ºC at 13-14 Ma to 1368 ºC for modern Icelandic lavas (Spice et al., 2016). The magnitude of increase is relatively minor (54 ºC; e.g., Spice et al., 2016) and only constrained by Icelandic lavas of two ages (0 Ma and 13-14 Ma), raising doubt to this increasing trend. Moreover, the thermal histories of the Galapagos and Iceland are compromised due to the interactions with a mid-ocean ridge making interpretation of temporal changes in temperature convoluted.

The Louisville Ridge, a hotspot distant from any MOR, is tectonically similar to the Hawaiian hotspot (Lonsdale, 1988). Melt flux for the Louisville Ridge was relatively constant (3-4 x 10^3 km^3/yr) from 70 Ma to 20 Ma (Figure 12; Lonsdale, 1984). The older (> 20 Ma) Louisville volcanoes formed islands whereas younger volcanoes (< 20 Ma) failed to reach sea level and are conical pointed seamounts (Figure 12; Lonsdale, 1984). Older NWHR volcanoes southeast of the HEB near Kammu to Helsley seamount northwest of Academician Berg (31.9 Ma < volcano age < 43.7 Ma; ages from O'Connor et al., 2013) did not form volcanic islands and individual

volcano spacing is the largest for the entire Hawaiian-Emperor chain. At ~ 30 Ma in the Hawaiian Ridge near Academician Berg, the Hawaiian hotspot began increasing in melt flux and temperature forming the first Hawaiian Islands since the Emperors (Figure 9). At 20 Ma, the Hawaiian hotspot was forming islands with carbonate platforms like Northampton and Laysan Island (Figure 12). During the formation of Gardner and the French Frigate Shoals volcanoes at 10-12 Ma, the Hawaiian hotspot continued forming larger islands and extensive carbonate platforms bridging multiple volcanic centers. Concurrently, magma production at the Louisville hotspot was dramatically waning and distances between individual volcanoes became longer (Figure 12).

The reason for the contrasting difference melt flux variations between the Hawaiian and Louisville hotspots is not clear at this time. If both of these plumes arose from the core-mantle boundary (CMB), as some have previously hypothesized (e.g., Morgan, 1971; Weis et al. 2011), then perhaps there was a shift in the heat flux point source location. With the additional heat injection to drive the vigor of local convection near the stem, the Hawaiian plume could sustain higher mass flux in the plume leading to dramatic increases in the melt flux near the surface. The observed increase in melt flux and mantle potential temperature over time makes the Hawaiian hotspot unusual. Future research should focus on the longer scale evolution of the Hawaiian mantle plume and investigate the mantle potential temperature – melt flux relationship during the formation of the Emperor seamounts to investigate a part of the chain which varies little in melt flux. Additionally, a joint-inverse approach to modelling the time-dependent melt flux of two thermo-chemical plumes from the same source region could yield insight in to this unknown mechanism in the lower mantle and the physical parameters that determine the changes observed at the surface.

8.3) Remaining uncertainties in critical variable assumptions of this study

There are several sources of uncertainty when estimating T_p for the NWHR. Perhaps the largest source of uncertainty is whether the available samples are representative of individual volcanoes' maximum T_p. Sampling gaps still remain in critical areas like the smallest seamounts between the HEB and Academician Berg. Recent efforts to increase the number of volcanic samples from the NWHR have been conducted by the Ocean Exploration and Research group of the National Oceanic and Atmospheric Association. A total of 24 ROV dives on NWHR volcanoes have retrieved 2 volcanic samples per dive location. These new samples are from volcanoes of small to moderate volumes during the pulse in high melt flux and T_p near Gardner. Critical sample collections from Pioneer, Northampton, Maro Reef, Gardner and St. Rogatien can yield valuable additional data to this critical portion of the NWHR where melt flux pulsed to a maximum during the formation of the NWHR. Investigation of the T_p of these volcanoes could yield insight in to the relationship of mantle potential temperature and melt flux between ~7-20 Ma.

In calculating the $T^{ol\text{-}liq}$ and T_p of the NWHR volcanoes, the another source for uncertainty was associated with the range in K_d values when generating the hypothetical sample populations of parental magma compositions (Appendix 3). This is because the variation in parental magma compositions propagates uncertainty in calculation of critical variables in all subsequent calculations, specifically the melt fraction and pressure. The range of parental magma compositions that were incorporated in the temperature calculations and spanned the range of more than 3σ of the average K_d value found by Matzen et al. (2011; Figure A.1). If one were to reduce that range in parental magma compositions to only those within the equilibrium range of $K_d = 0.345 \pm 0.009$ (1σ), the uncertainty in $T^{ol\text{-}liq}$ and subsequent correction to T_p would be greatly reduced. Simplistically, reducing the variability in parental magma compositions by half of that assumed in

this study (i.e., $K_d = 0.345 \pm \textit{0.15}$) would translate in to a ~50 % reduction in the standard deviations in final temperature calculations.

The next largest source of uncertainty in calculating T_p is the pressure and melt fraction. The precision of T_p would increase if future studies used the trace element compositions of these lavas to estimate the melt fraction of the parental magmas (e.g., Pietruszka et al., 2013). The uncertainty in pressure is more difficult to constrain due to the fact that reconstructed parental liquids are likely representative of the average composition of mixed liquids from considerable depth ranges within the melting column (Wright and Klein, 2006). Putirka (2008) showed good agreement between the pressures calculated from pyroxene-liquid thermobarometers and the Si-activity barometer used in this study. An independent assessment of these Si-activity pressures and olivine-liquid temperatures using other thermometers and barometers could provide additional support for the range in olivine-liquid temperatures and equilibration pressures found here (e.g., Spice et al, 2016). In addition to the uncertainties in these variables, the approach to correcting $T^{ol\text{-}liq}$ to T_p is not consistent among published values of T_p for Hawaii (e.g. Putirka et al., 2007 vs. Herzberg and O'Hara, 2002). Thus, external consistency in the methods to derive parental magma compositions and approach to calculating mantle potential temperature could ease the difficulty of comparing results from various studies.

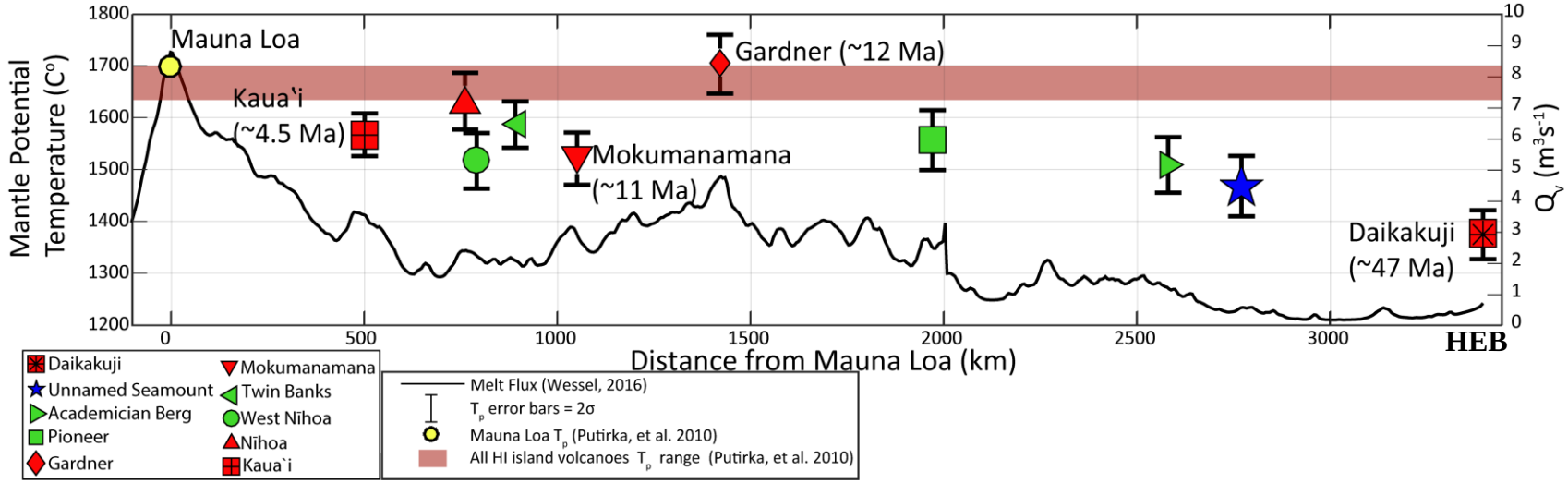

Figure 9. Plot of the maximum potential temperatures along with the melt flux along the distance of the NWHR from the Hawaiian-Emperor Bend (HEB) to Mauna Loa. The red horizontal band represents the range in T_p in Hawaiian volcanoes from Putirka et al. (2010) and the yellow dot is the maximum mantle potential temperature at Mauna Loa of 1690 ºC. Red symbols are tholeiitic lavas ($Alk_i < -0.3$). Green symbols are transitional lavas ($-0.3 \leq Alk_i \leq 0.3$). The alkalic lava from the Unnamed seamount is a blue star ($Alk_i > 0.3$).

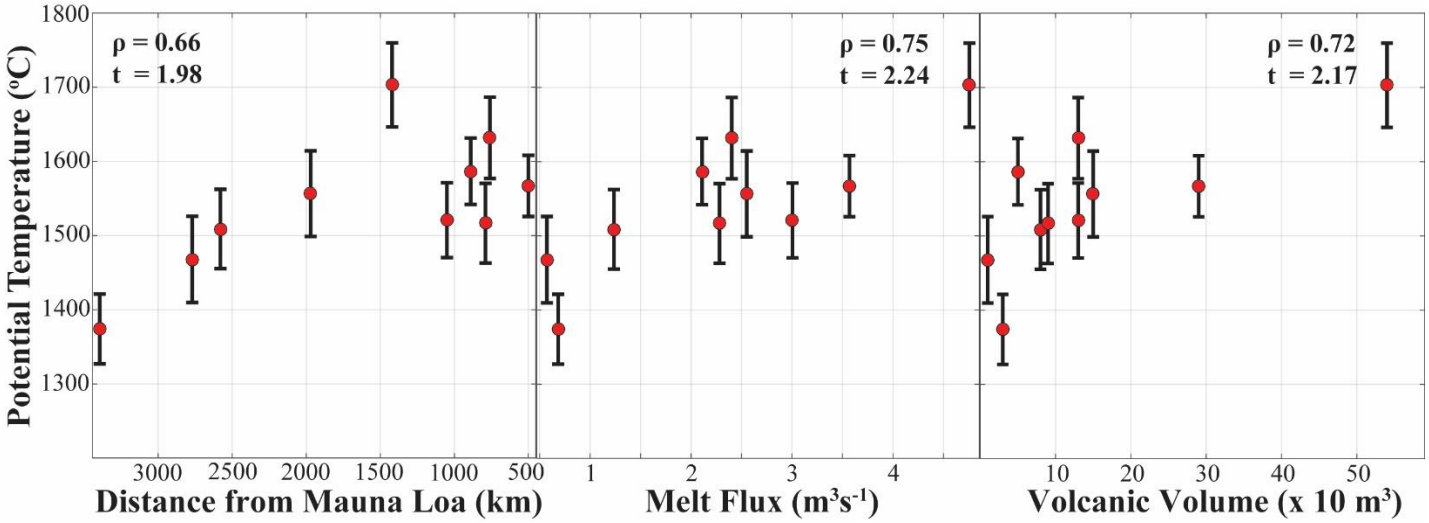

Figure 10. Plots of the maximum mantle potential temperatures calculated for each volcano against the distance from Mauna Loa, melt flux, and the volcanic volumes. Each comparison was tested for significance of correlation using the non-parametric Spearman's correlation coefficient (ρ). By defining the level of confidence of 95% for this statistical value, one can test the significance of these correlation coefficients using the student's t-distribution. The critical t-value for a confidence level for 95% is 1.83. If the calculated t-value for the Spearman's rank correlation coefficient is greater than this critical t-value, one can reject the null hypothesis that these pair of variables are not correlated (i.e. H_o: $\rho = 0$; H_1 : $\rho \neq 0$). Thus, the coupling between mantle potential temperatures vs. distance, melt flux, and volcanic volume can be assessed.

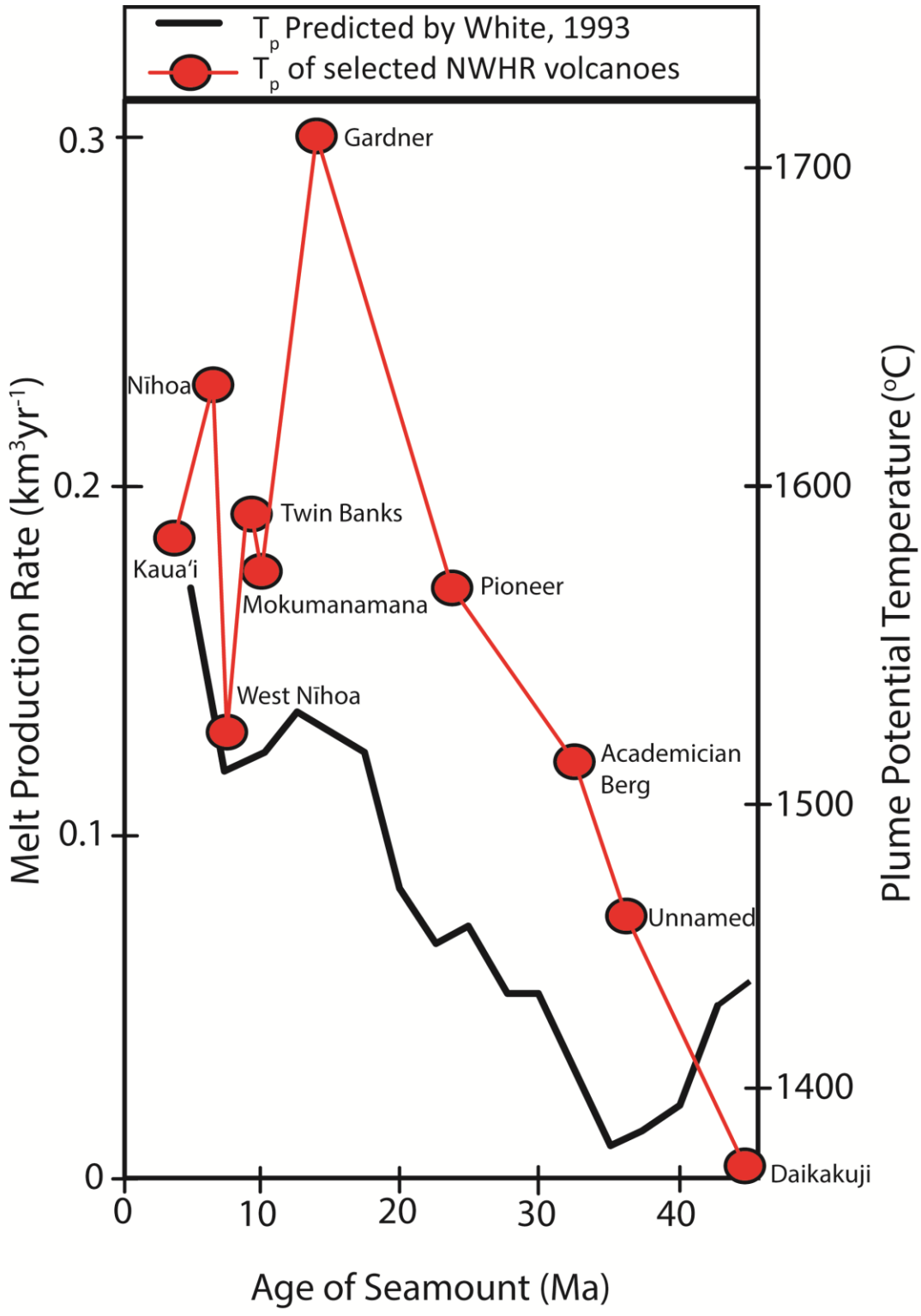

Figure 11. Plot of plume potential temperature and melt production vs the age of the seamount along the NWHR. The red dots and line show new T_p estimates from this study. The black line are the approximate potential temperatures predicted by White (1993) that are needed to sustain the melt production rates assuming constant mass flux of the upwelling plume material deduced from Watson and McKenzie (1991).

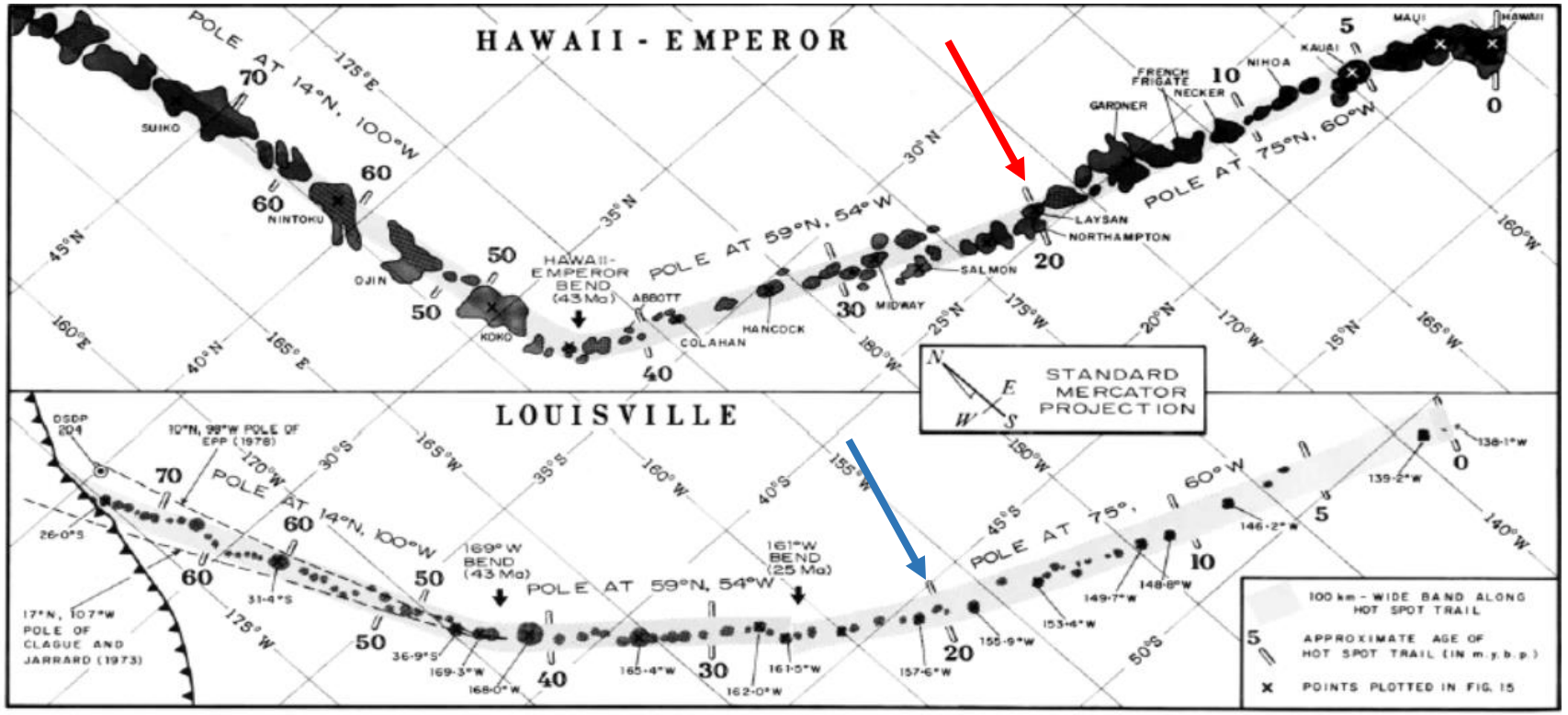

Figure 12. Comparison charts of the Hawaii-Emperor and Louisville chains on the same scale showing the dramatic differences in melt flux of the Hawaiian and Louisville hotspots from 0 to ~70 Ma (from Lonsdale 1988). The white bars outline in black along the Hawaiian and Louisville ridges are the approximate ages of the hotspot at those locations. The blue arrow indicates the location where the Louisville hotspot magma production began a dramatic decrease seen by the relatively smaller volcanoes spaced at greater distances in the eastern portion of the ridge compared to those produced in the western > 20 Ma portion of the ridge. The volcanic volumes for < 20 Ma Louisville volcanoes is 0.3 x 10^3 km^3 – 3.3 x 10^3 km^3. The 20 Ma age and location of the Hawaiian hotspot is shown with the red arrow. NWHR volcanoes produced closely spaced and mostly large volcanic islands during this time while the Louisville volcanoes failed to break the sea surface. NWHR volcanic volumes for volcanos 5 – 20 Ma are 6.6 x 10^3 km^3 to 54 x 10^3 km^3 (Bargar and Jackson, 1974)

9) Conclusion

This study set out to answer two questions: 1) Has the mantle potential temperature of the Hawaiian mantle plume changed over time? and 2) How do the mantle potential temperature estimates relate to melt flux variations? To determine the long term Hawaiian hotspot thermal history, this study used 25 samples from ten volcanoes spanning the range in volcanic volumes and geographic extent of the NWHR. Using olivine thermometry and a Monte Carlo simulation, the mantle potential temperatures and uncertainties that arose from equilibrium condition assumptions for K_d made in estimation of parental magma compositions were calculated. These results revealed strong temporal variations. There was an increase in T_p between the HEB and Gardner followed by a second increase in T_p for the main Hawaiian Islands. The synchronous increase of mantle potential temperature and melt flux yielded a statistically significant correlation suggesting a strong coupling between magmatic productivity and plume temperature. The 329 ^oC increase in potential temperature from the Hawaiian-Emperor Bend to Gardner is more than the 175-200 ^oC increase predicted by White (1993) that was needed to sustain the increase in melt production along the leeward Hawaiian Ridge. Plume potential temperatures decreased along with melt flux after the formation of Gardner, showing no systematic trends until the main Hawaiian Islands. A second increase of 123 ^oC between Kauai and Mauna Loa was revealed from the new T_p estimates for Kauai lavas. The occurrence of two cycles of increasing plume potential temperature and melt flux since the Cretaceous make the Hawaiian hotspot unique from other hotspots, which usually display secular cooling thermal histories. The potential temperature estimates from 4.5 to 47.5 Ma of the Hawaiian plume from this study provides an independent constraint on the excess temperatures used in modelling plume dynamics. Additionally, the lower $T^{ol\text{-}liq}$ estimates along with new isotopic compositions for

Daikakuji, Mokumanamana, and West Nīhoa samples is indicative of a Loa-type source component that had a significant contribution in the generation of the magmas that formed these volcanoes (e.g., Harrison et al., in review).

Appendix: *Photomicrographs, Monte Carlo methodology, Olivine-liquid temperatures and mantle potential temperature results for all samples and parameterizations*

---

1) Photomicrographs of representative olivine and textures for samples

Representative photomicrographs of NWHR samples showing texture and extent of alteration. Top image is in plain-polarized light and bottom image is in cross-polarized light Scale bars are located in the top left corner of each image. The images are organized as listed in Table 1 (distance from Mauna Loa).

Daikakuji; A-55-1

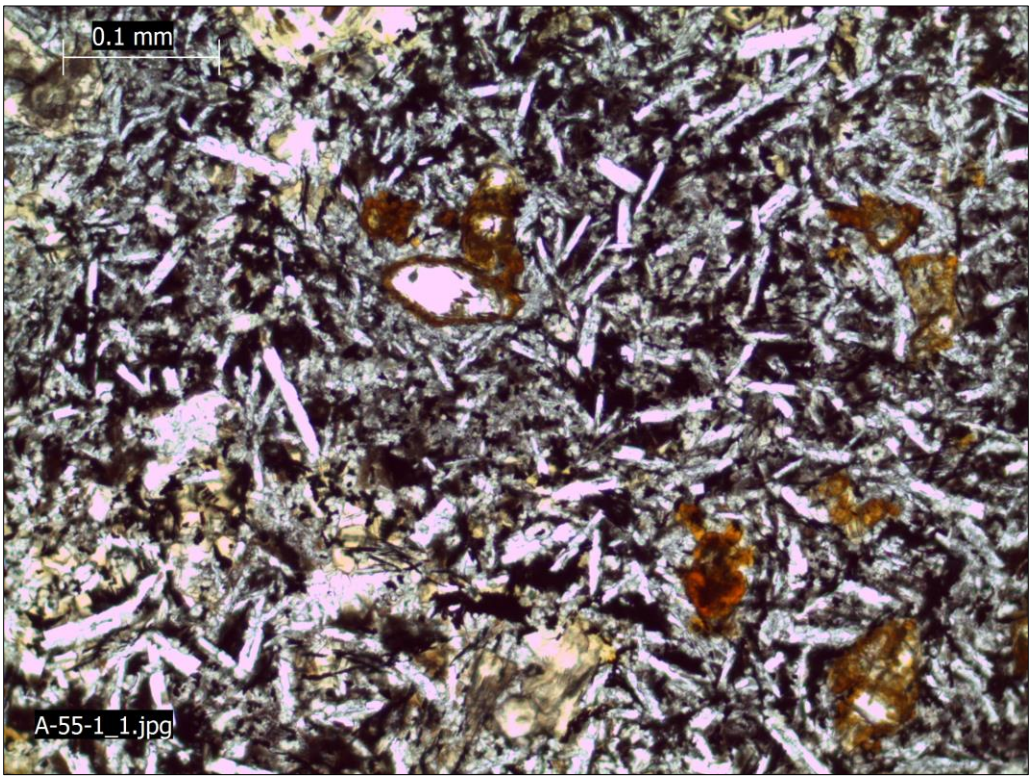

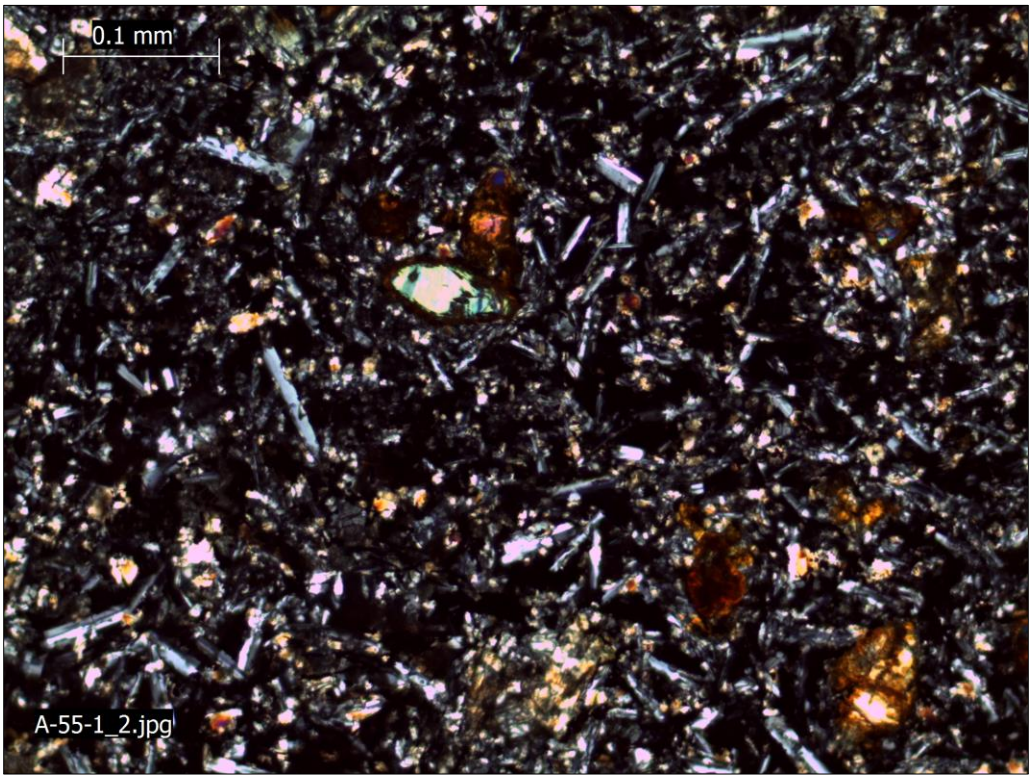

Daikakuji; A-55-2

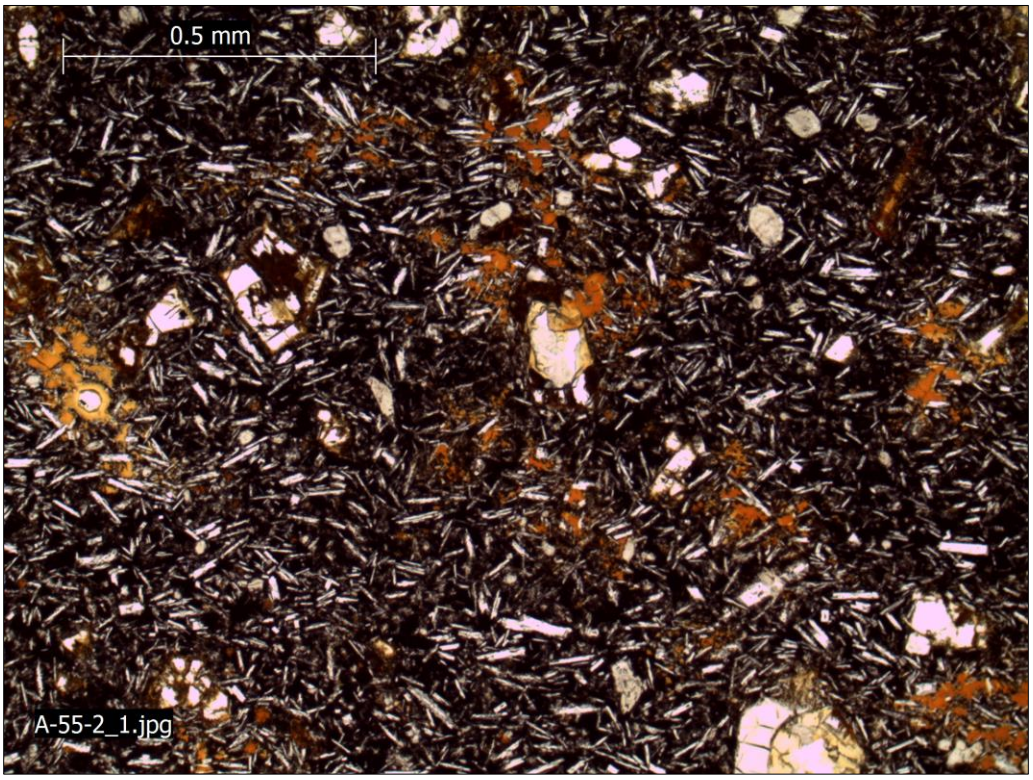

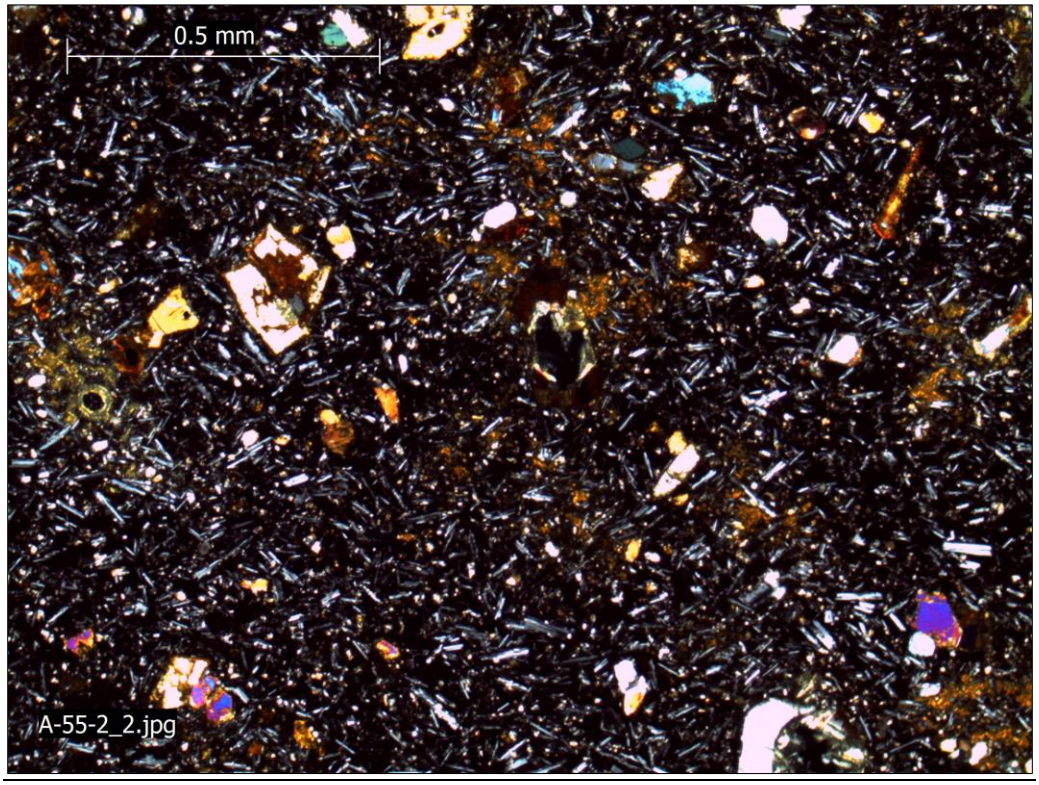

Daikakuji; A-55-4

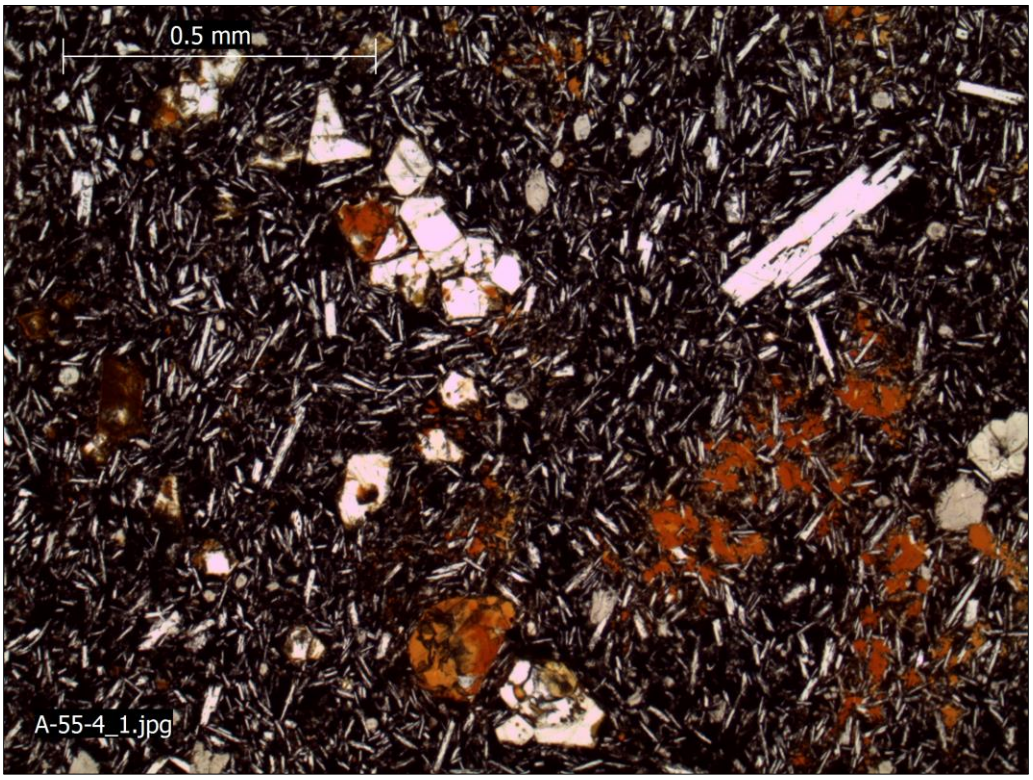

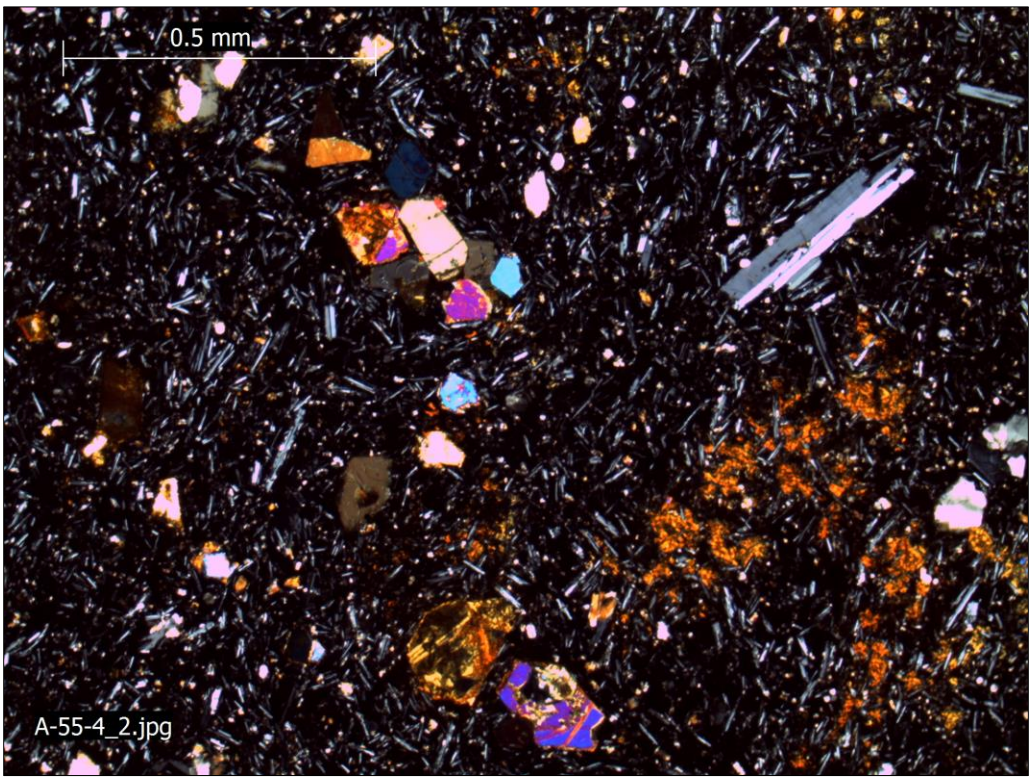

Unnamed Seamount; 84-28-C

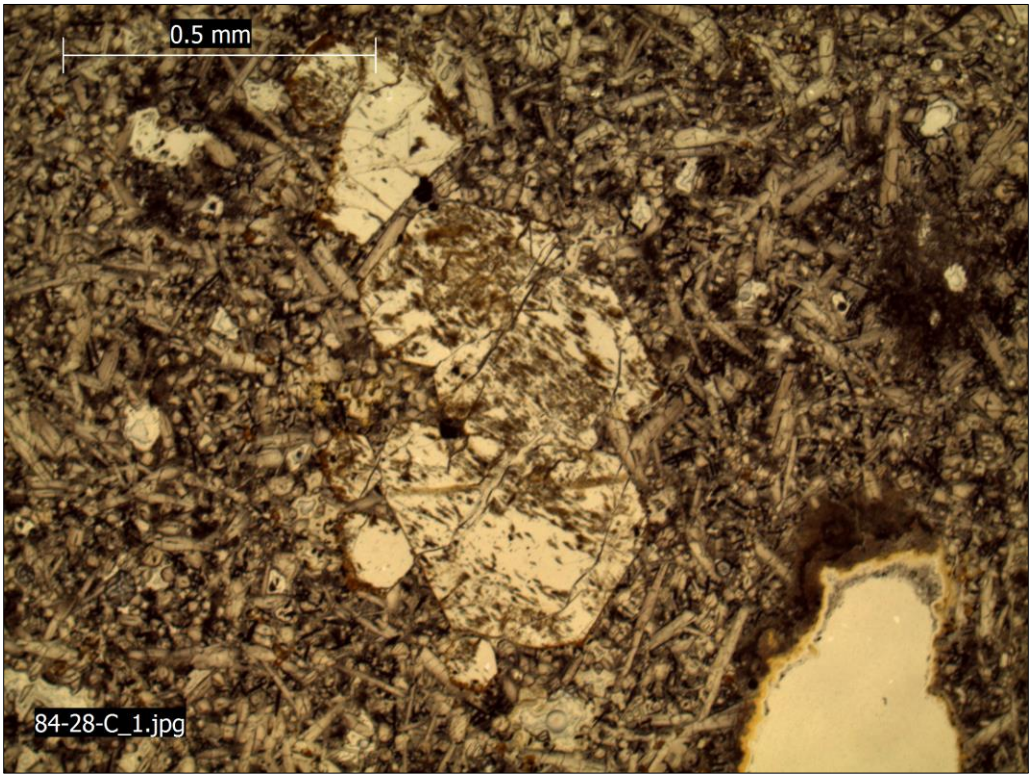

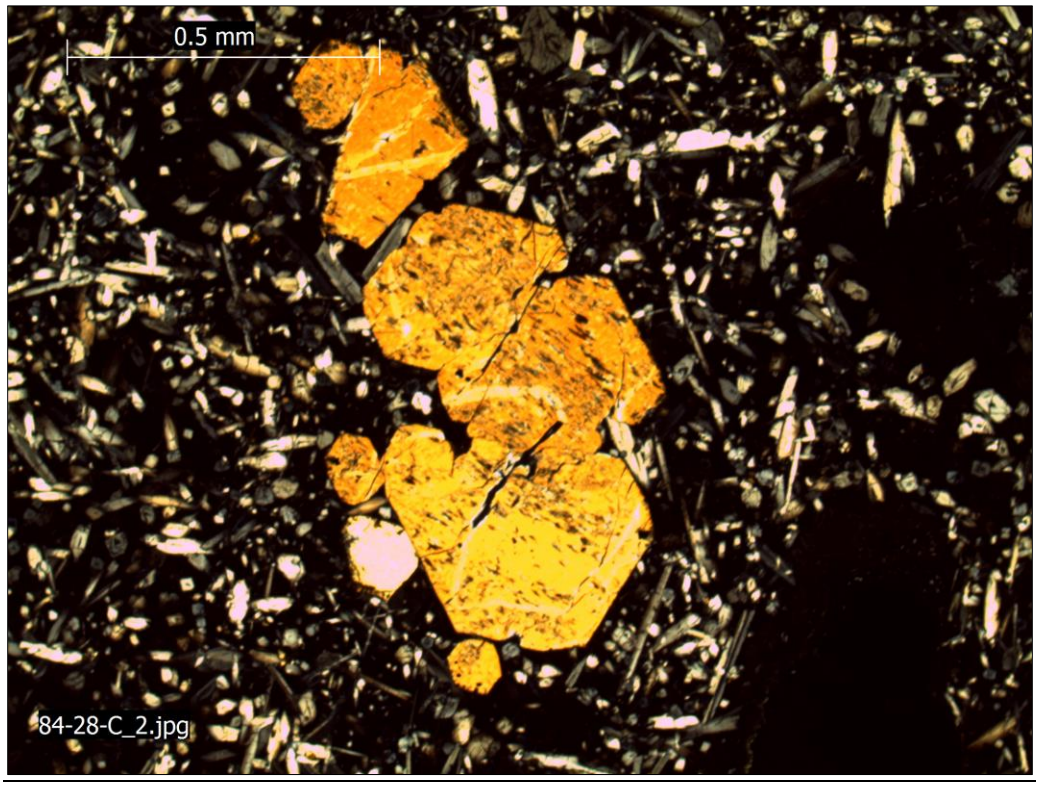

Unnamed Seamount; 84-28-D

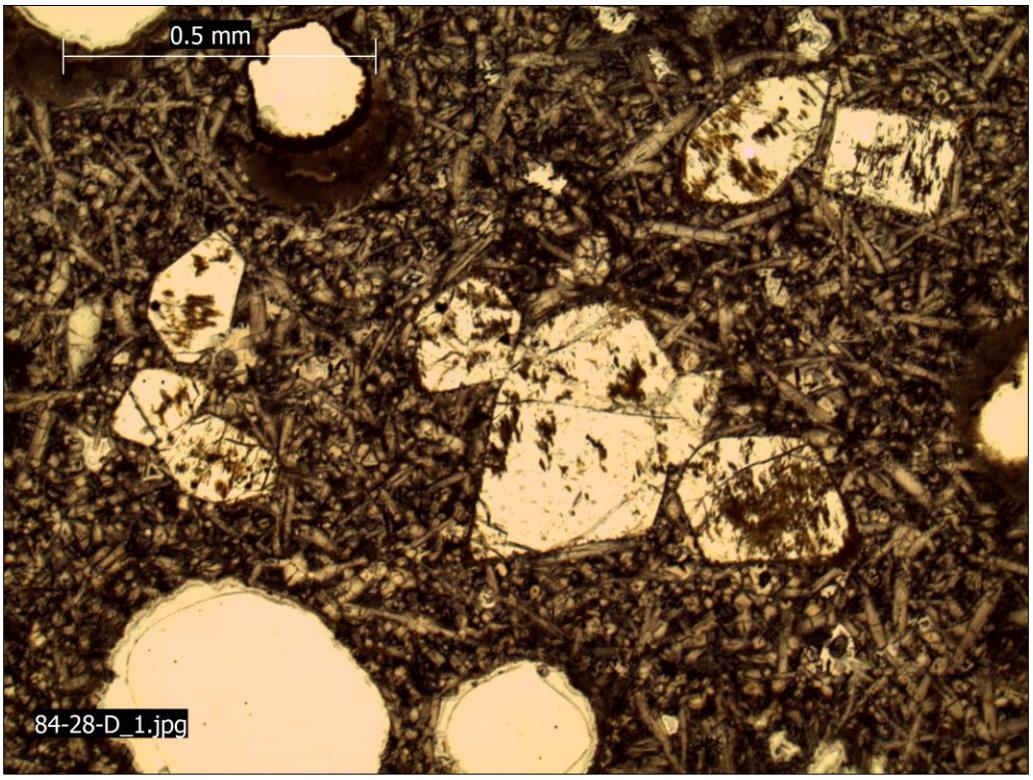

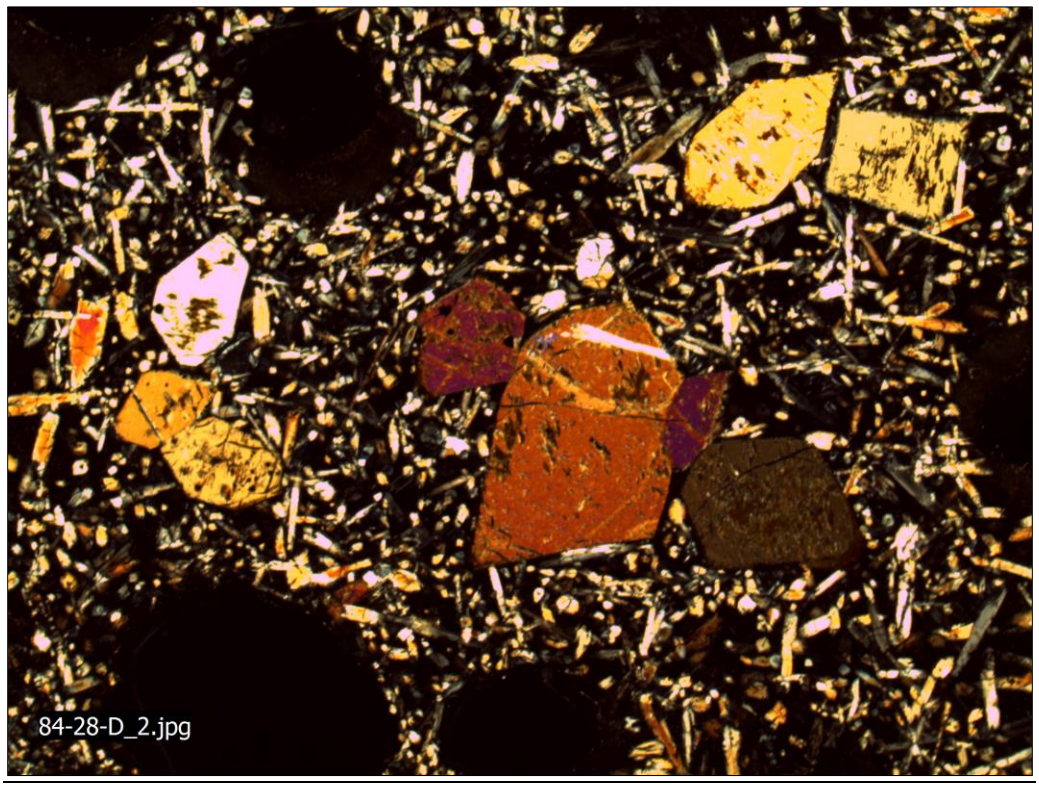

Academician Berg; 72-20-GG

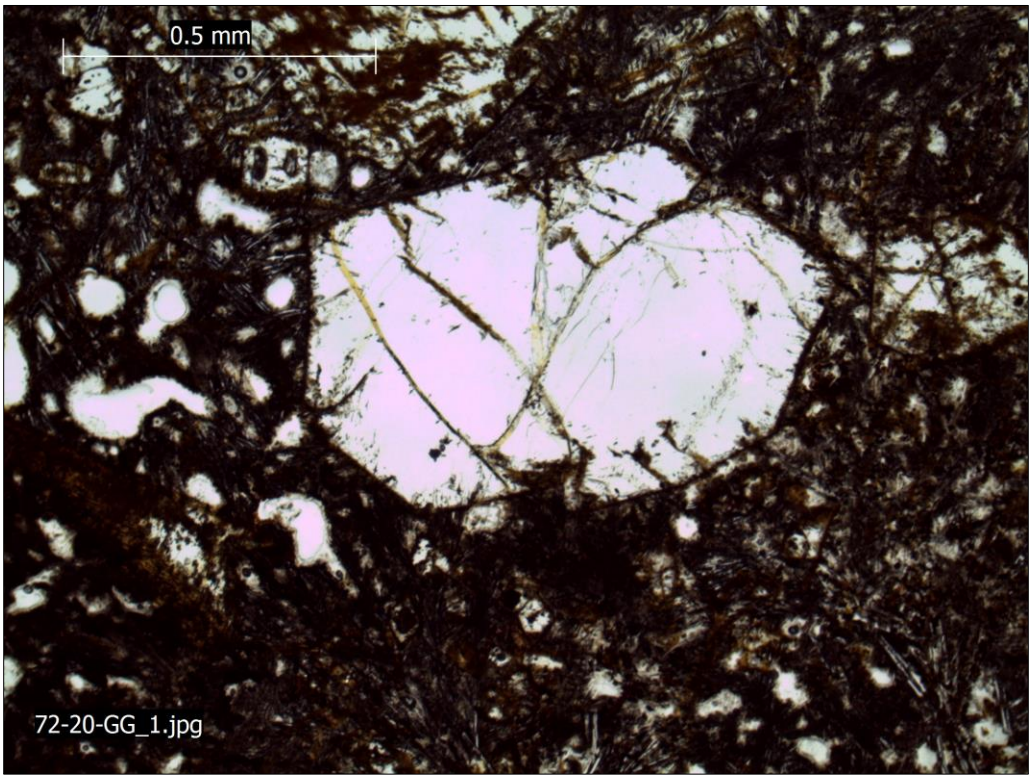

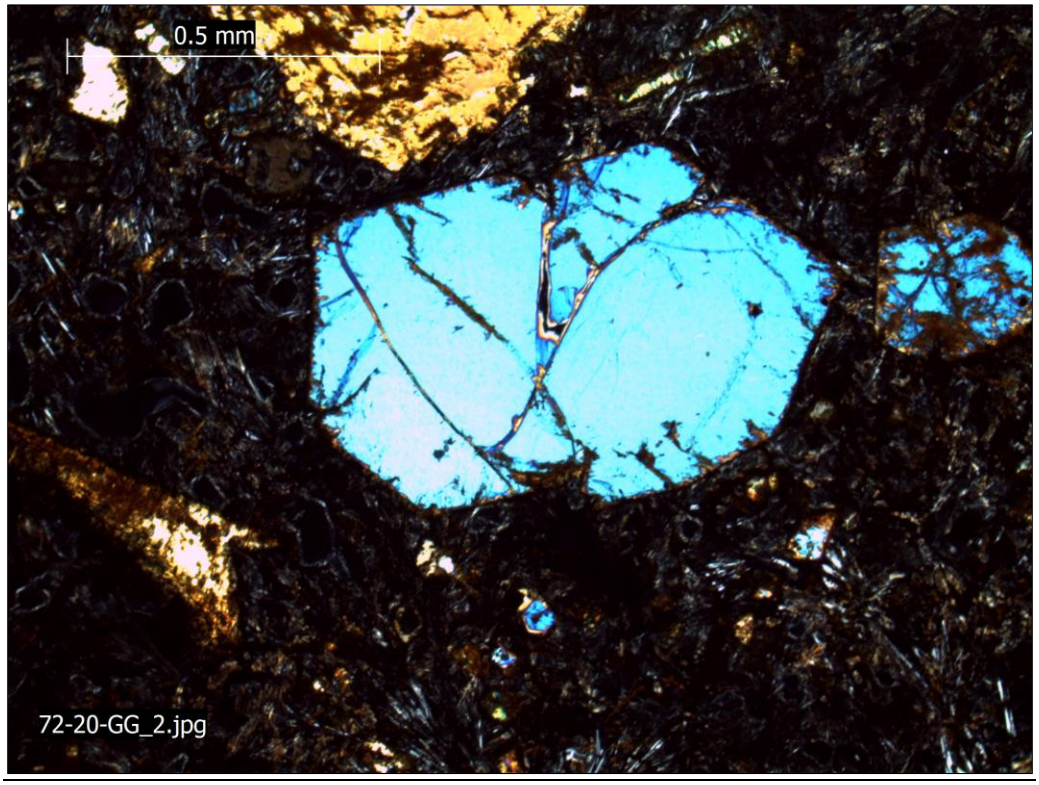

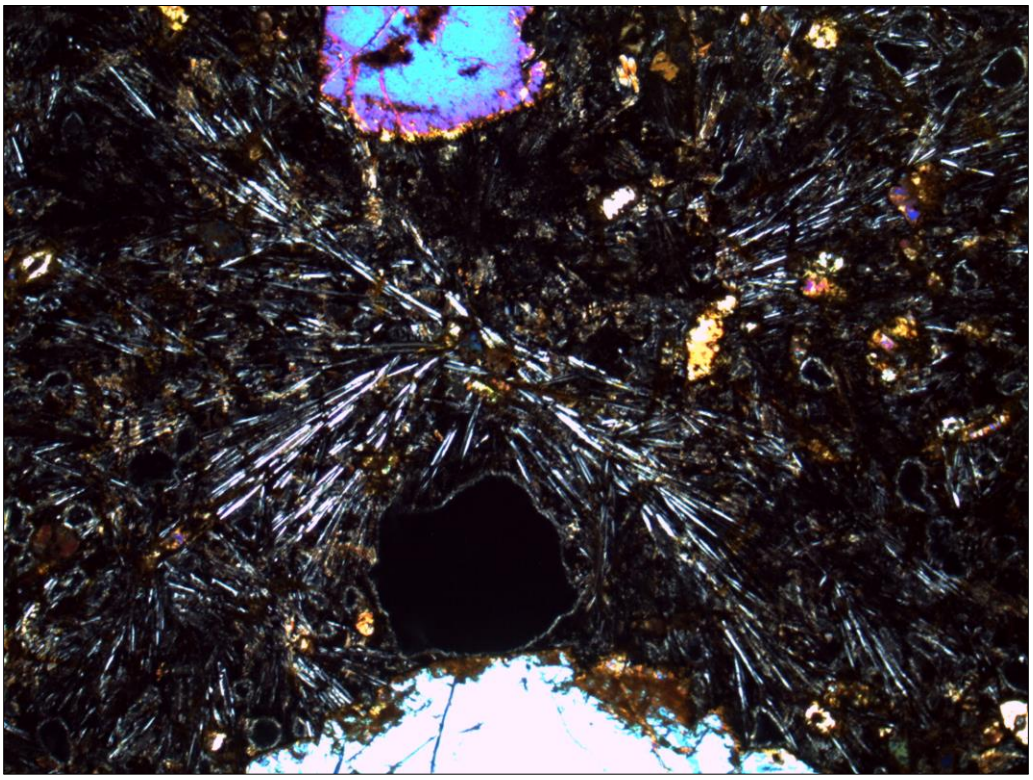

Pioneer; P5-526-2

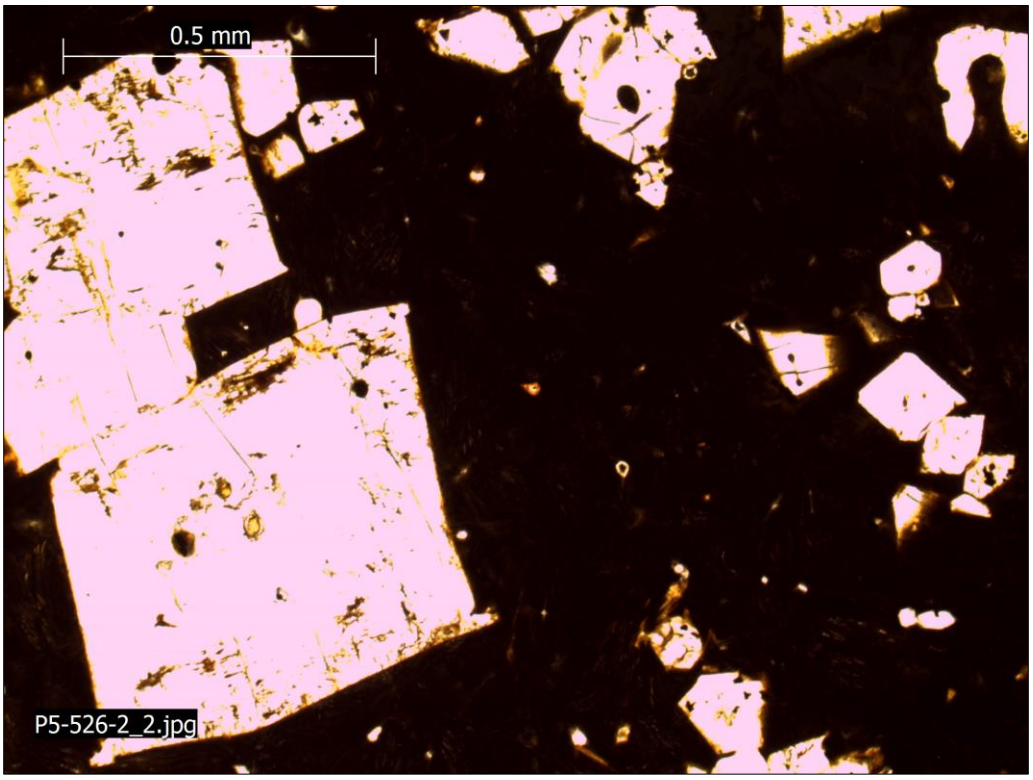

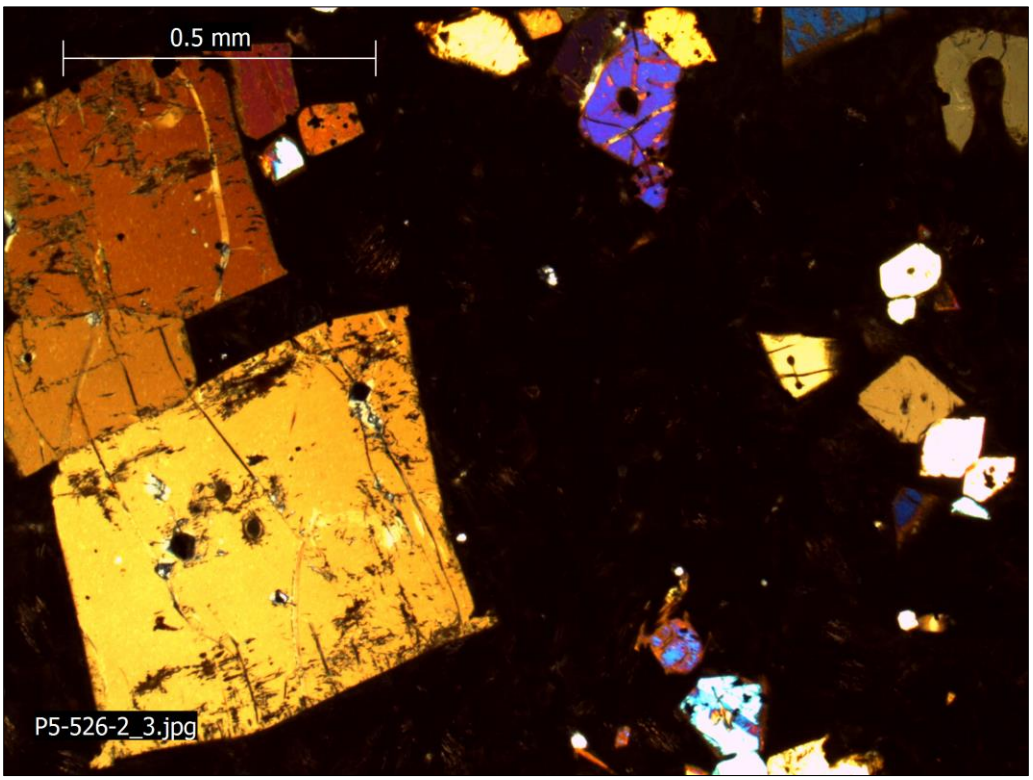

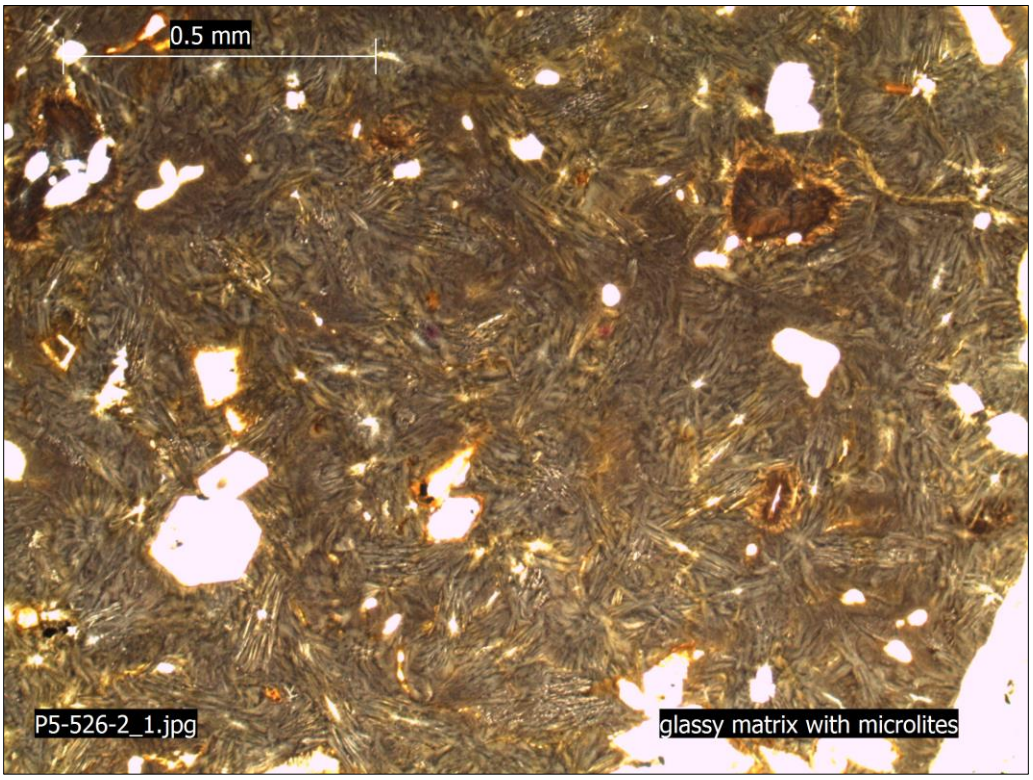
0.5 mm
P5-526-2_1.jpg
glassy matrix with microlites

Gardner; 76-6-7-(multiple samples with same texture)

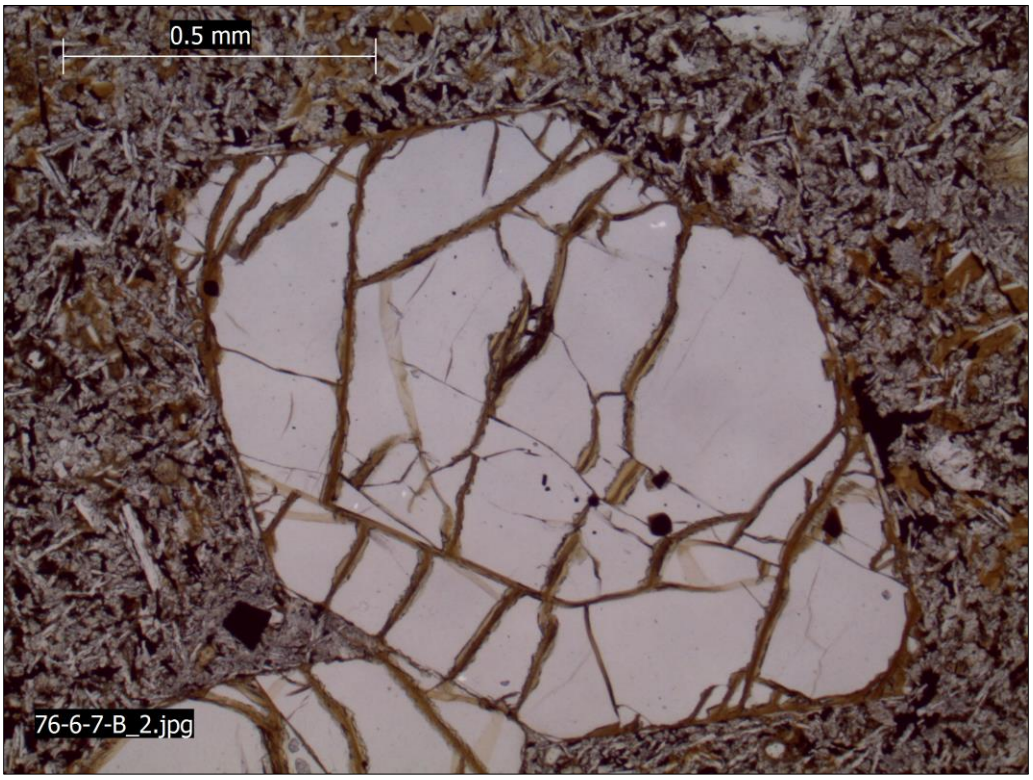

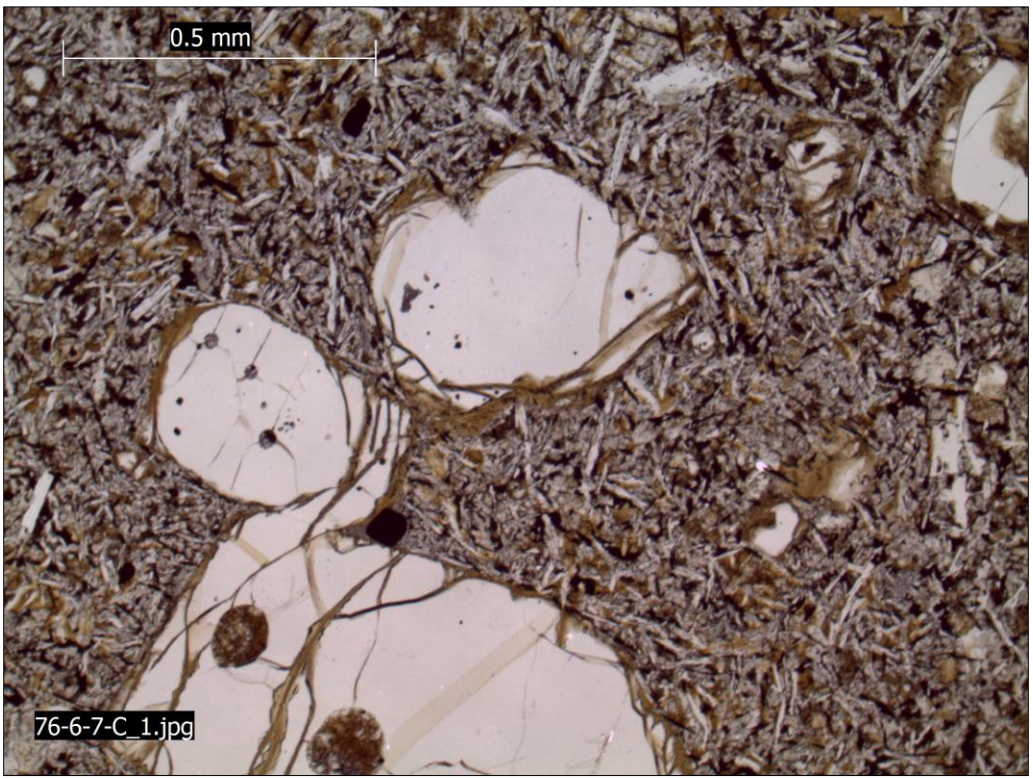

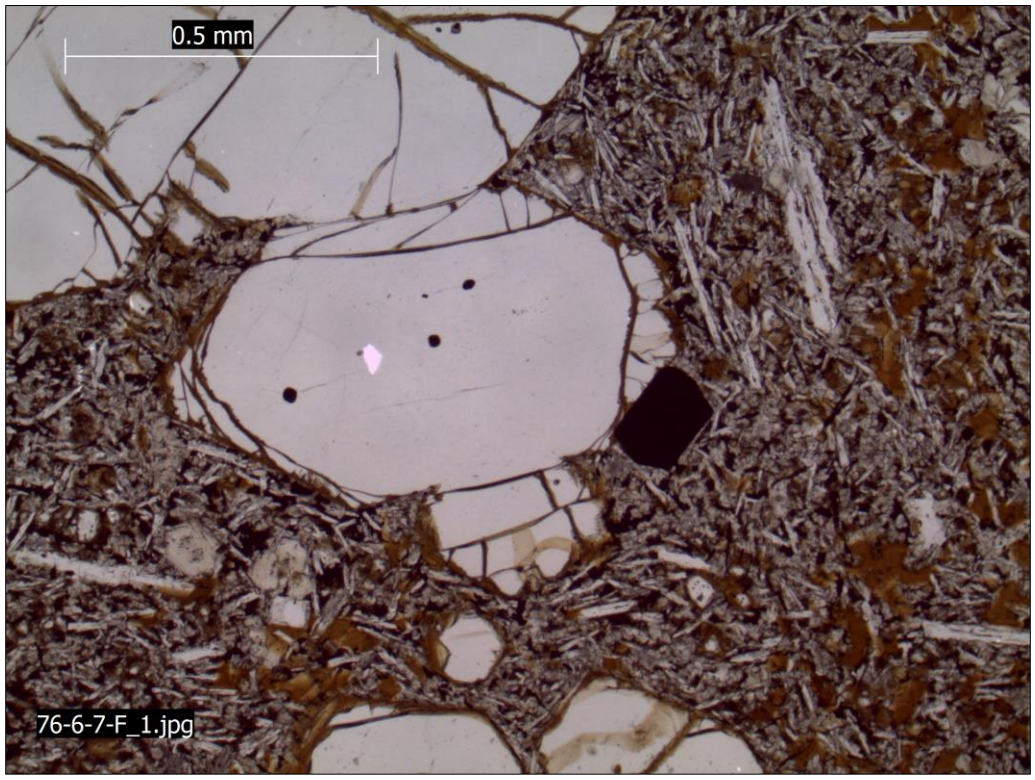
0.5 mm
76-6-7-F_1.jpg

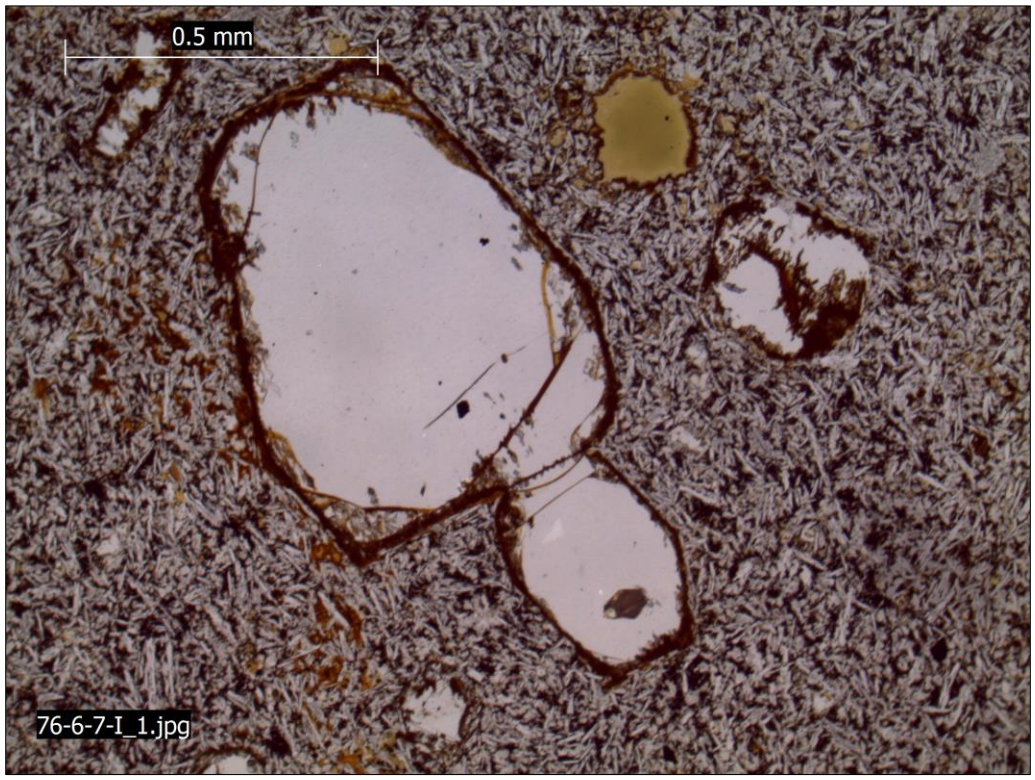
0.5 mm
76-6-7-I_1.jpg

Gardner; 76-6-7-H (Fo 91.85 Olivine)

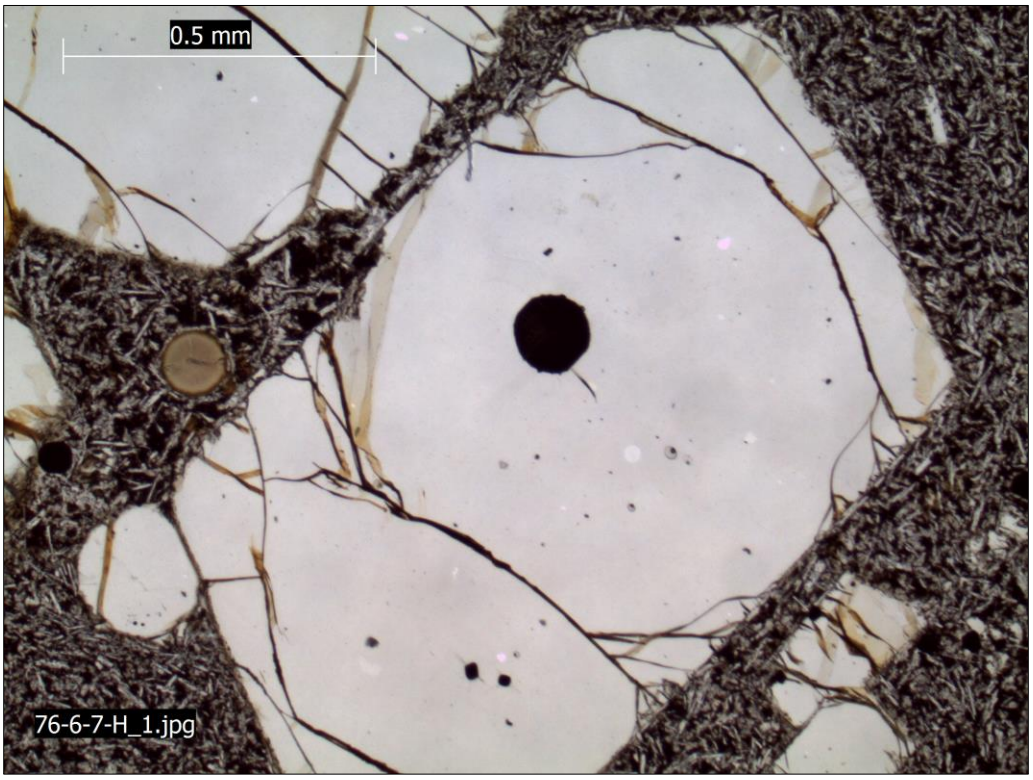

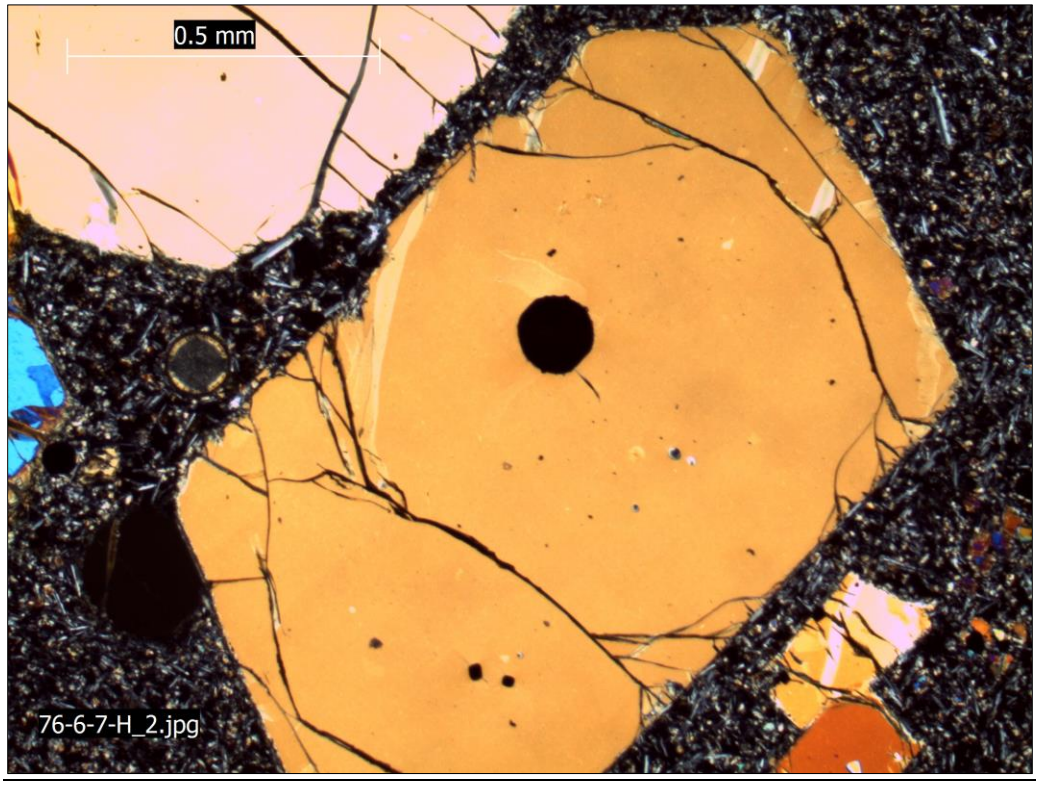

Mokumanamana (Necker); NEC-2A

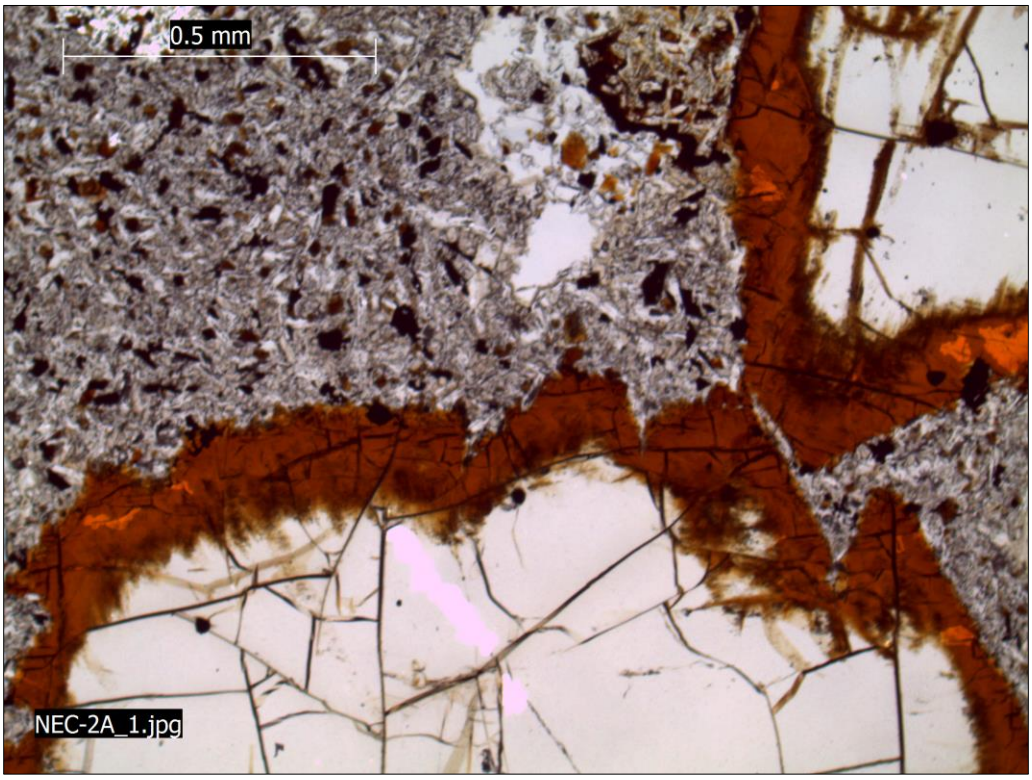

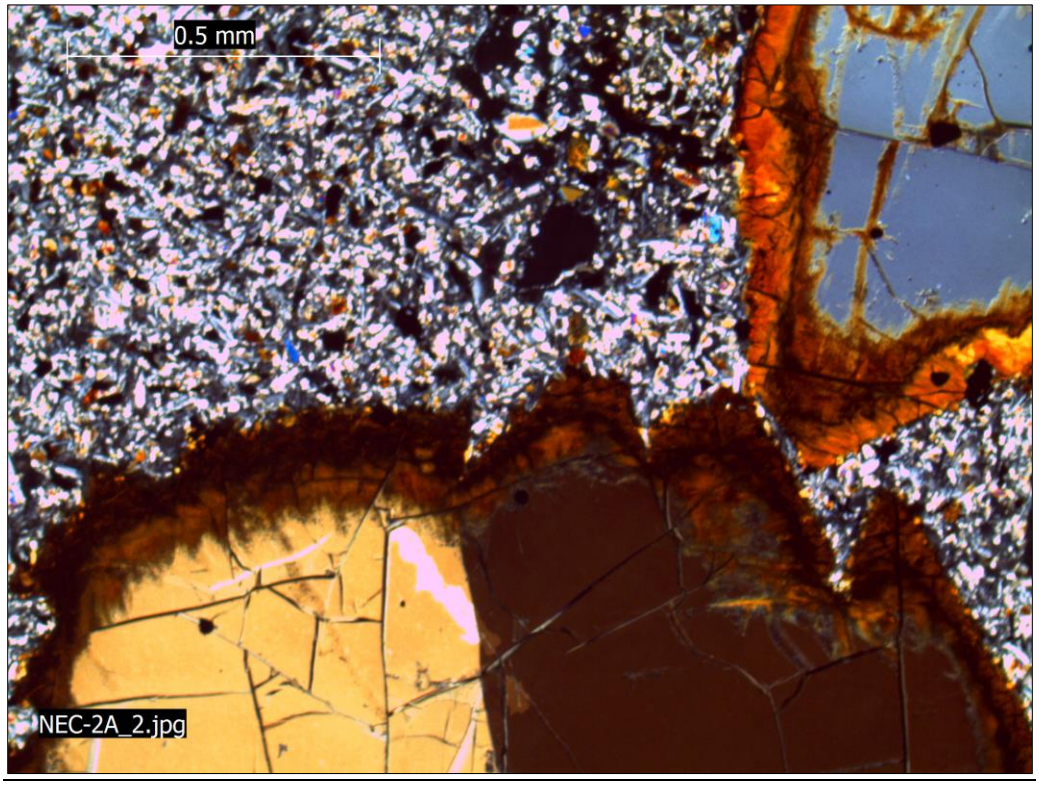

Mokumanamana (Necker); NEC-3A

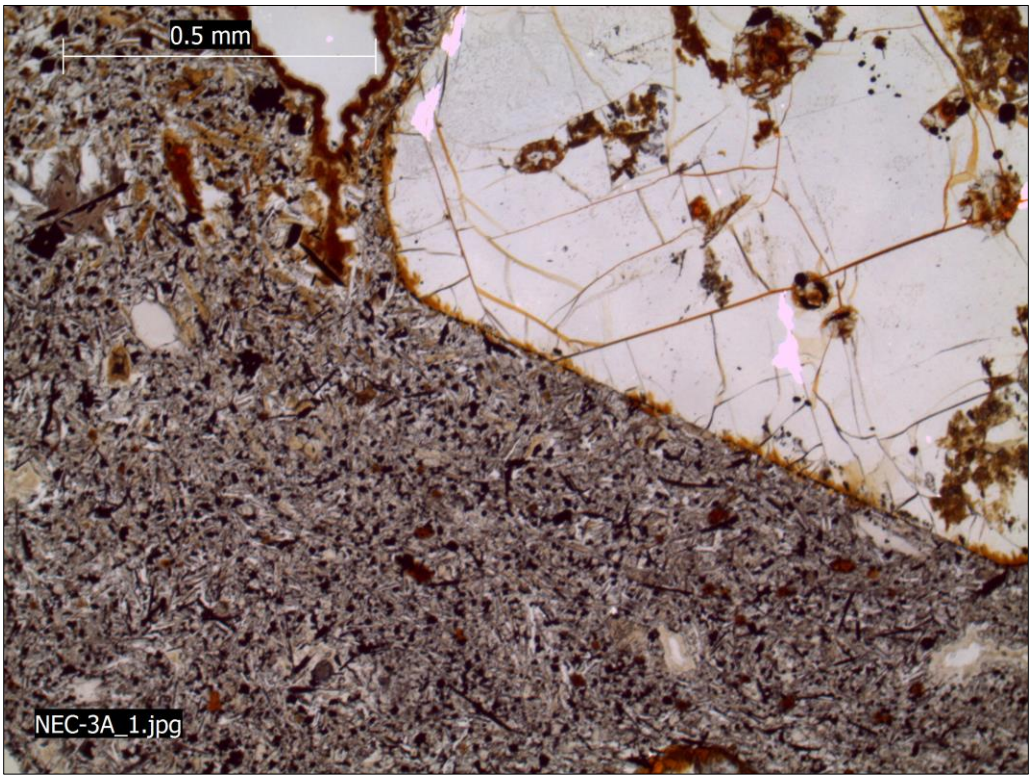

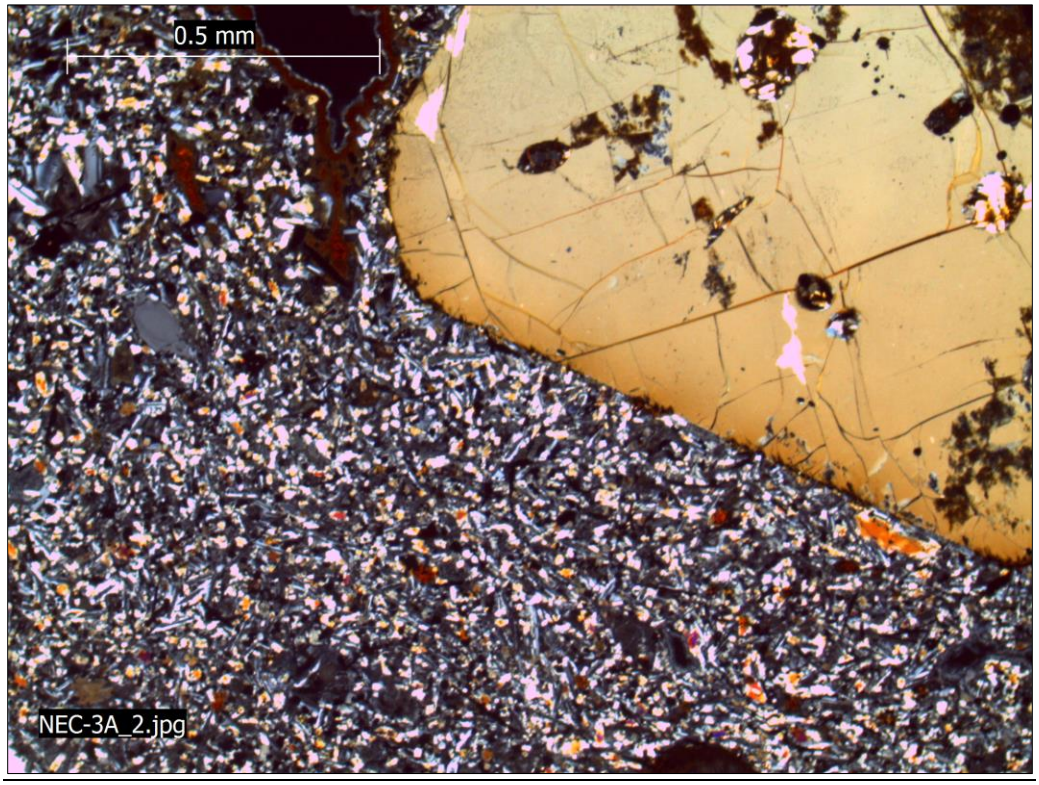

Twin Banks; P5-688-1

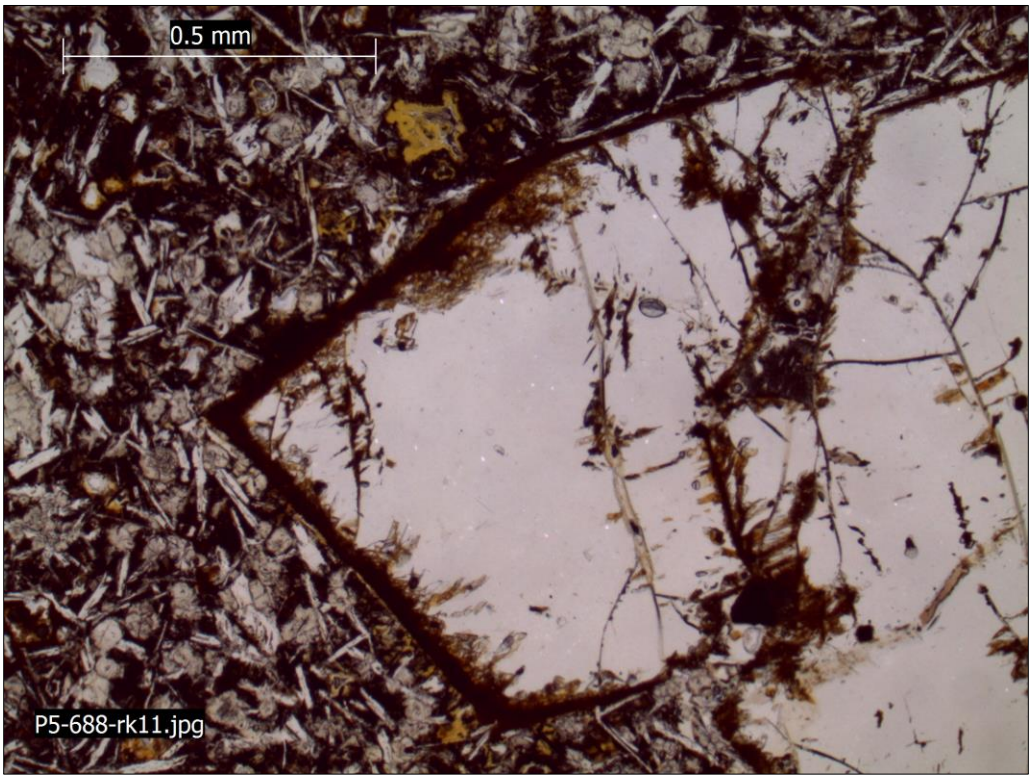

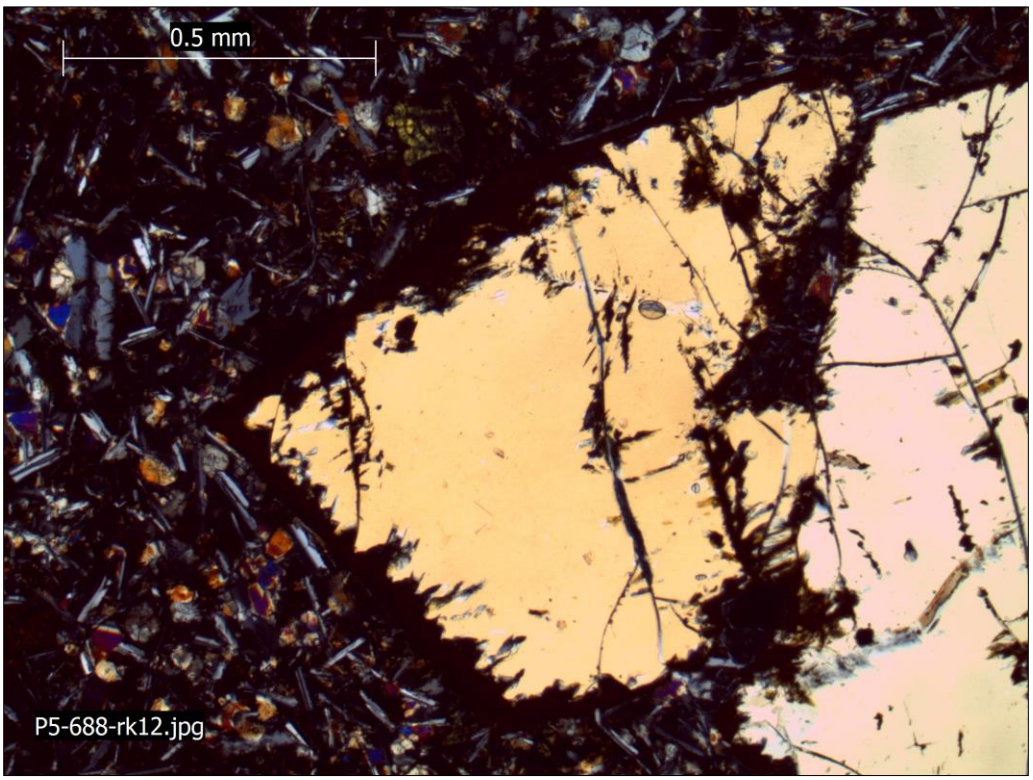

West Nīhoa; 76-9-11

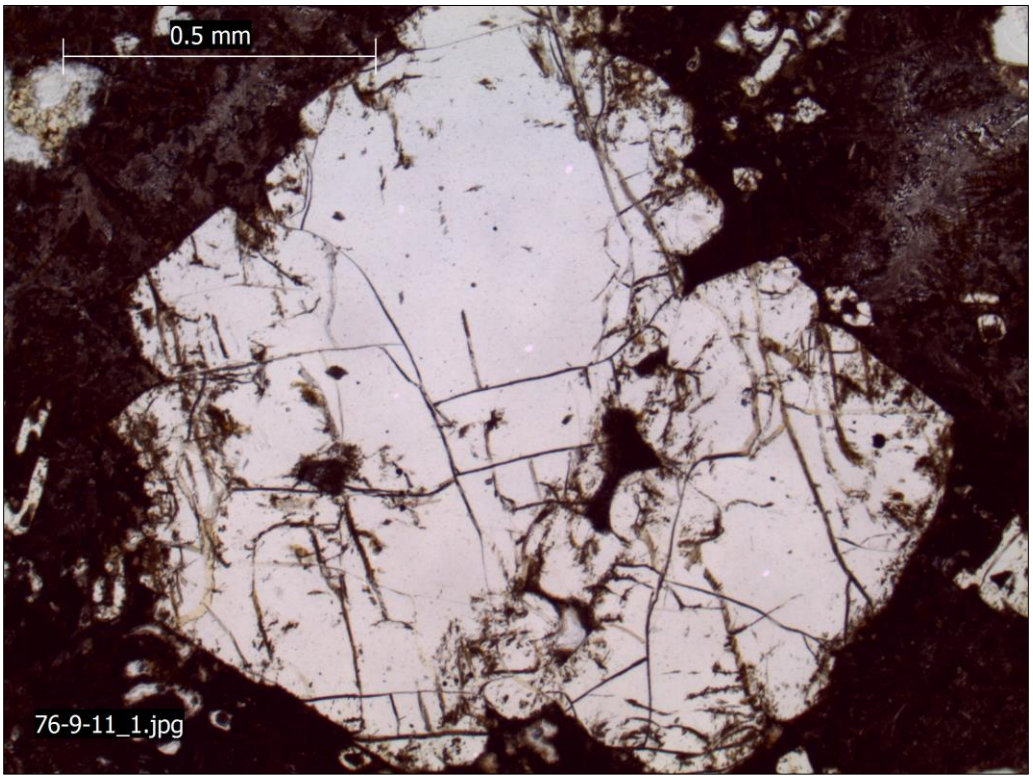

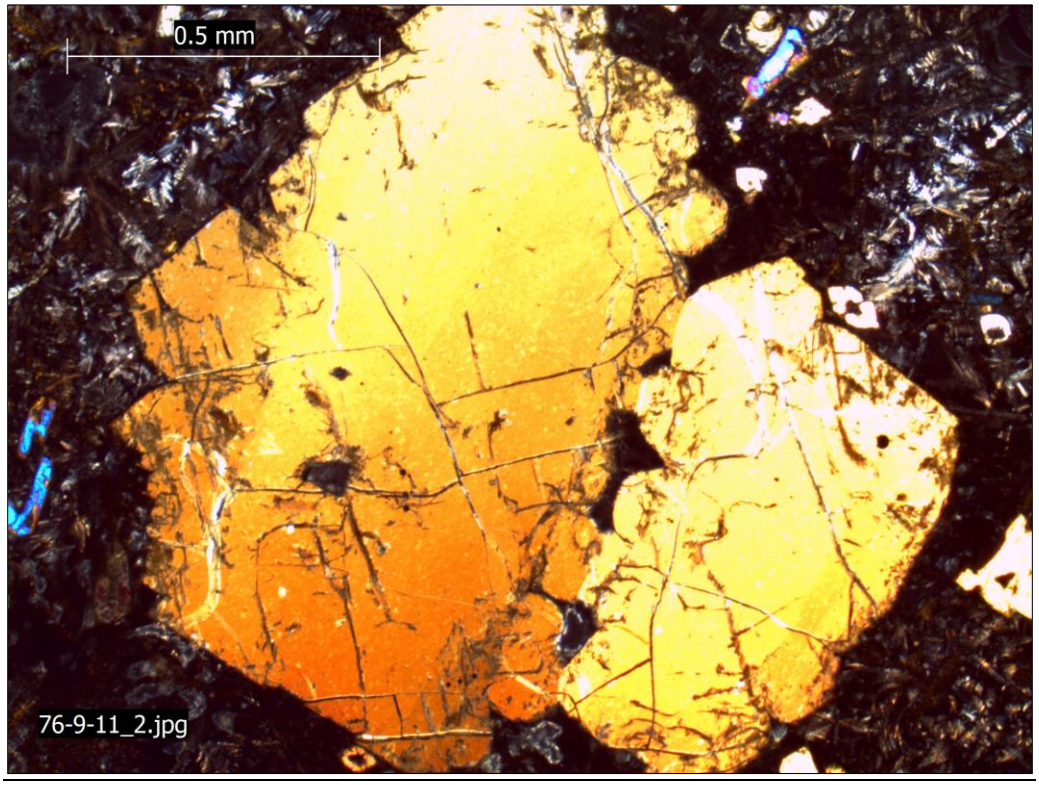

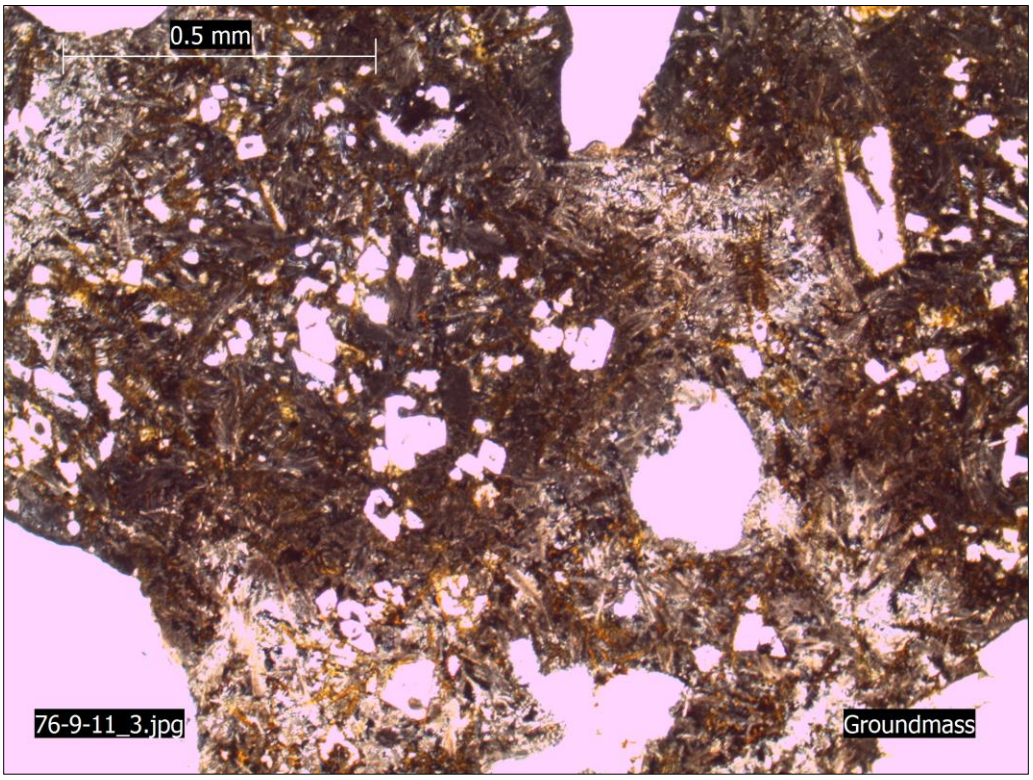
0.5 mm
76-9-11_3.jpg
Groundmass

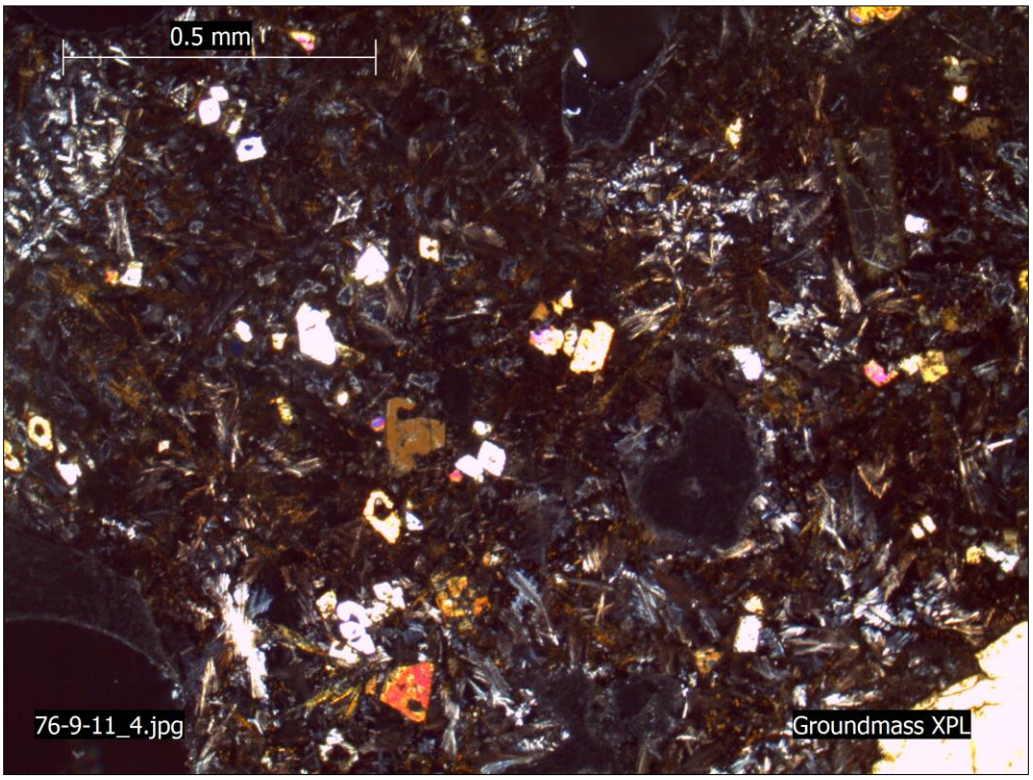
0.5 mm
76-9-11_4.jpg
Groundmass XPL

Nīhoa; NIH-D1-2

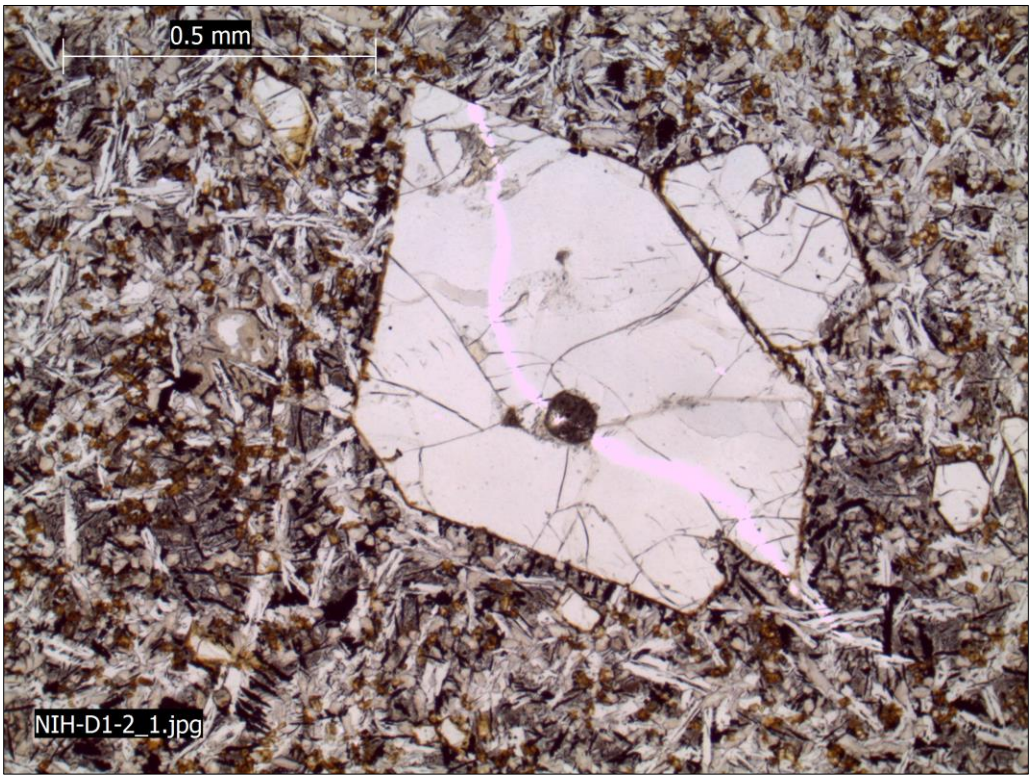

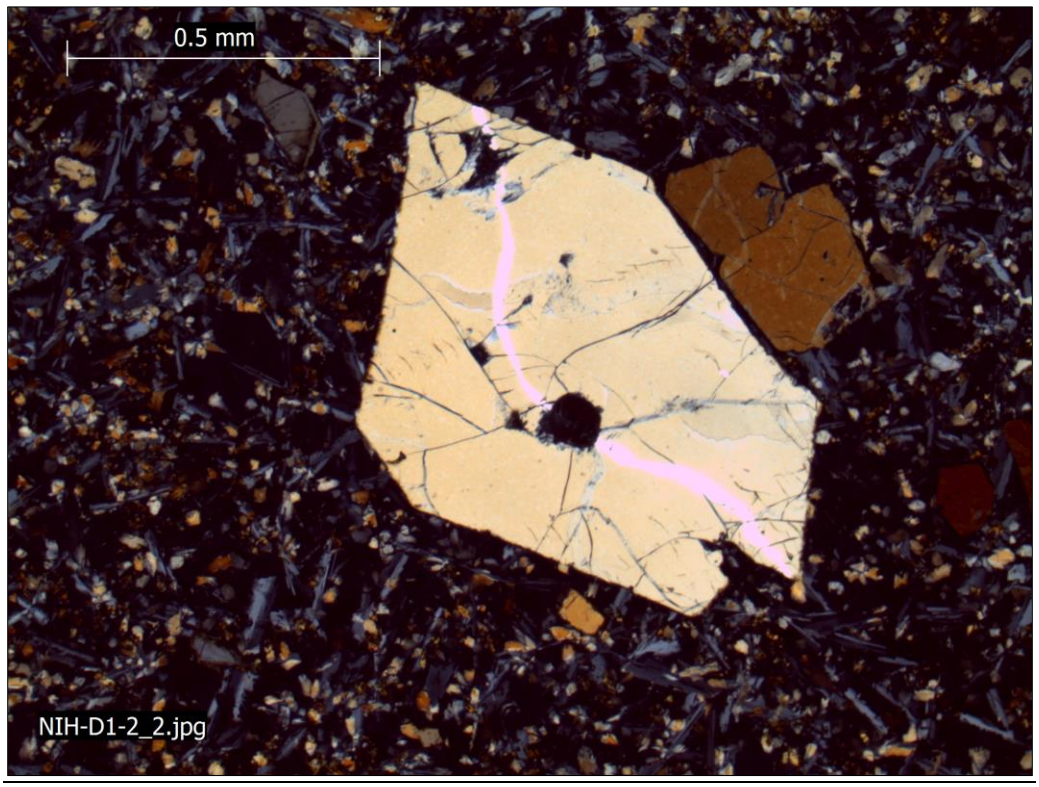

Nīhoa; NIH-D1-4

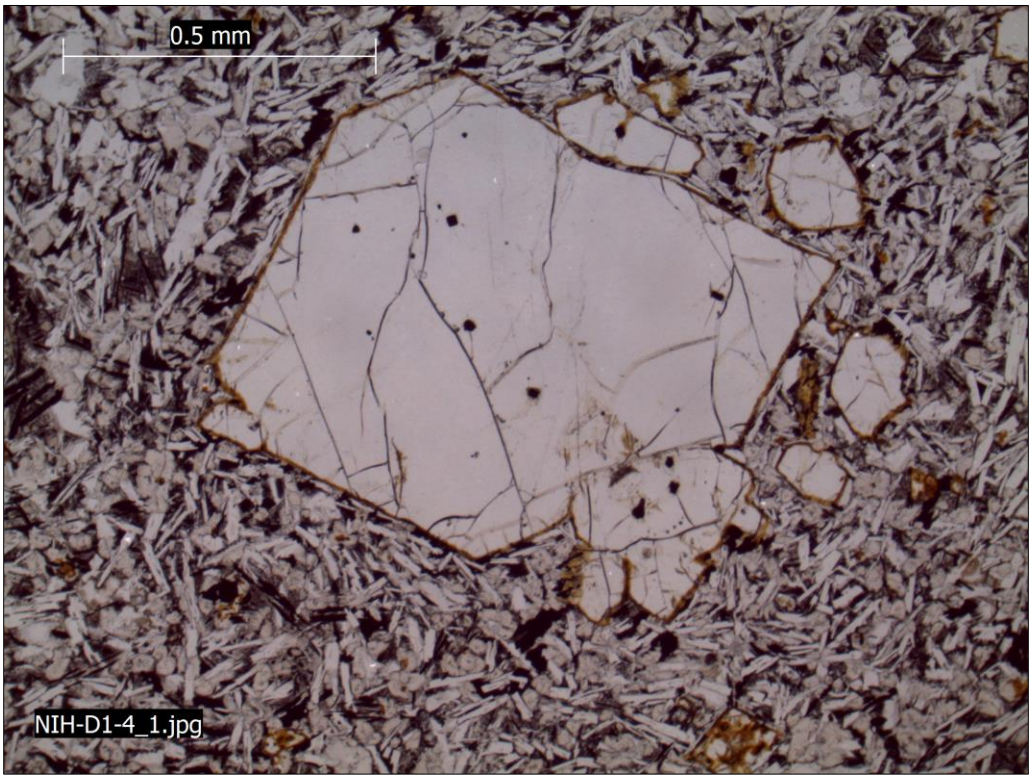

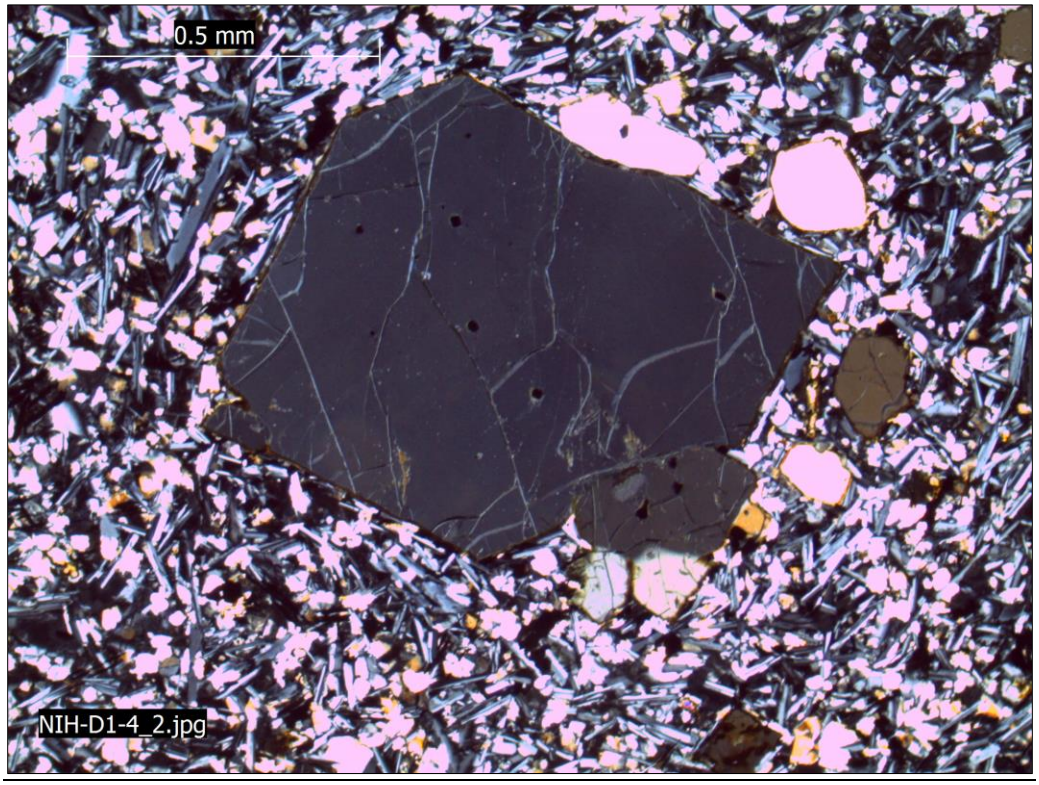

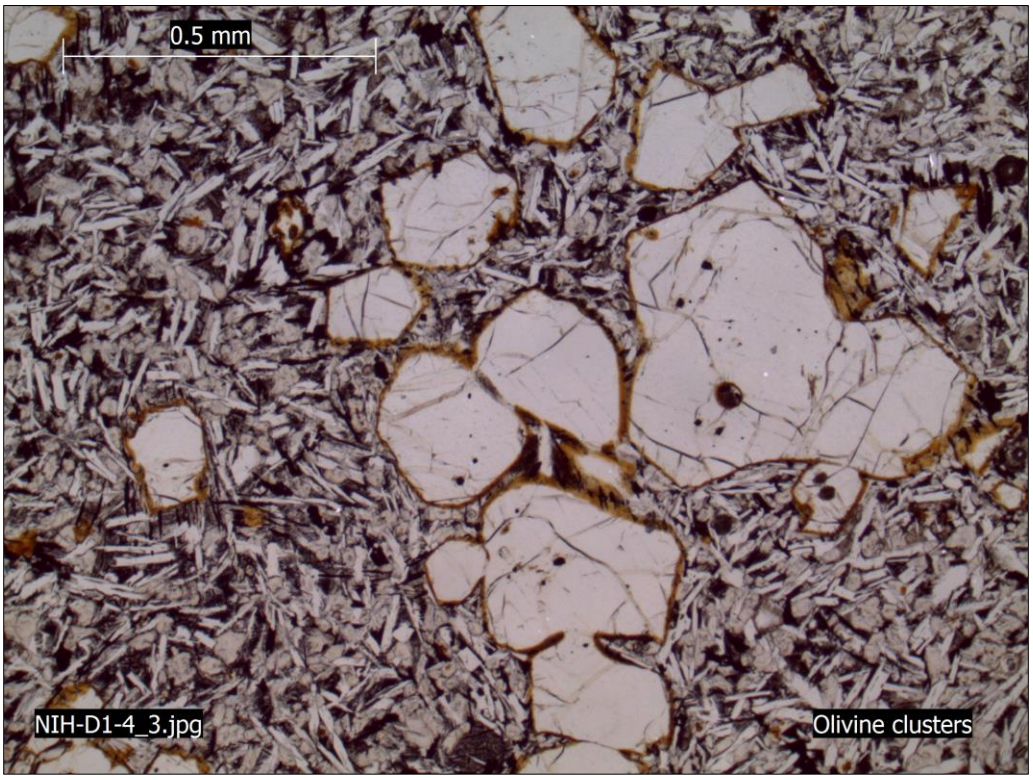
0.5 mm
NIH-D1-4_3.jpg
Olivine clusters

Nīhoa; NIH-F5

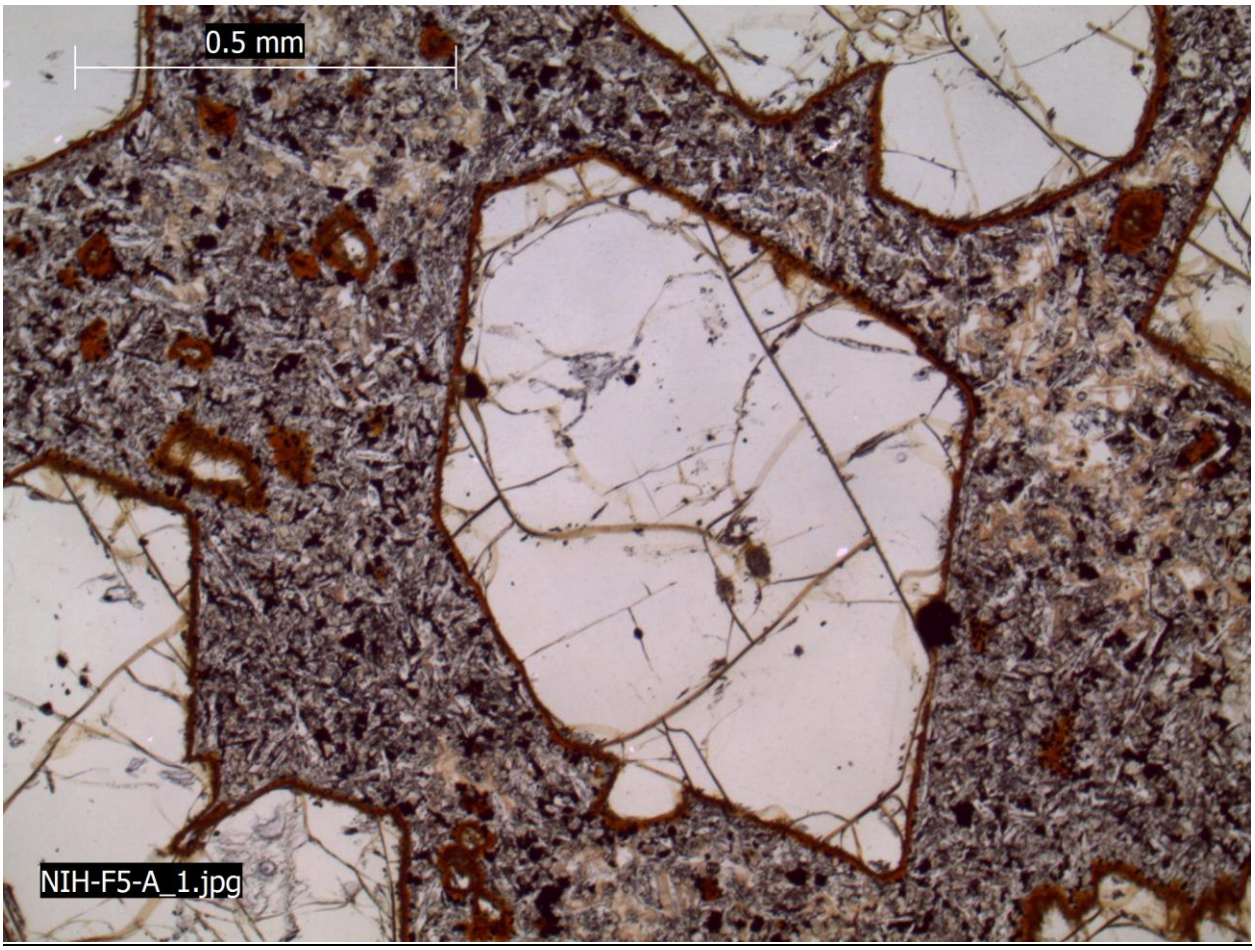

Nīhoa; NIH-F9

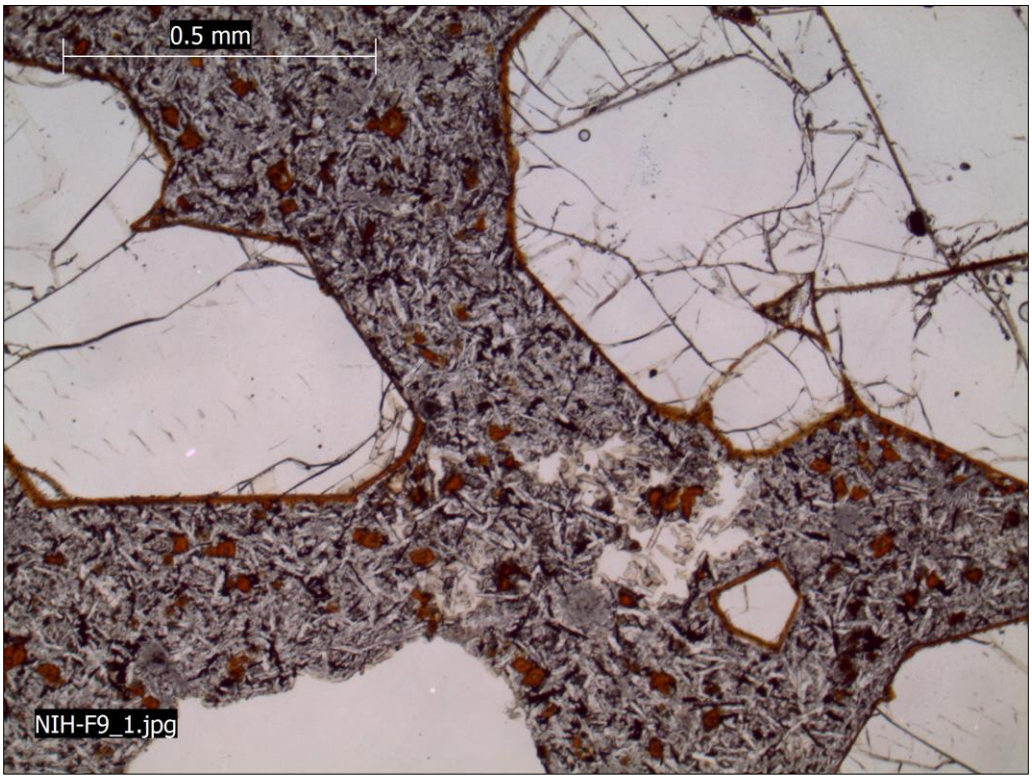

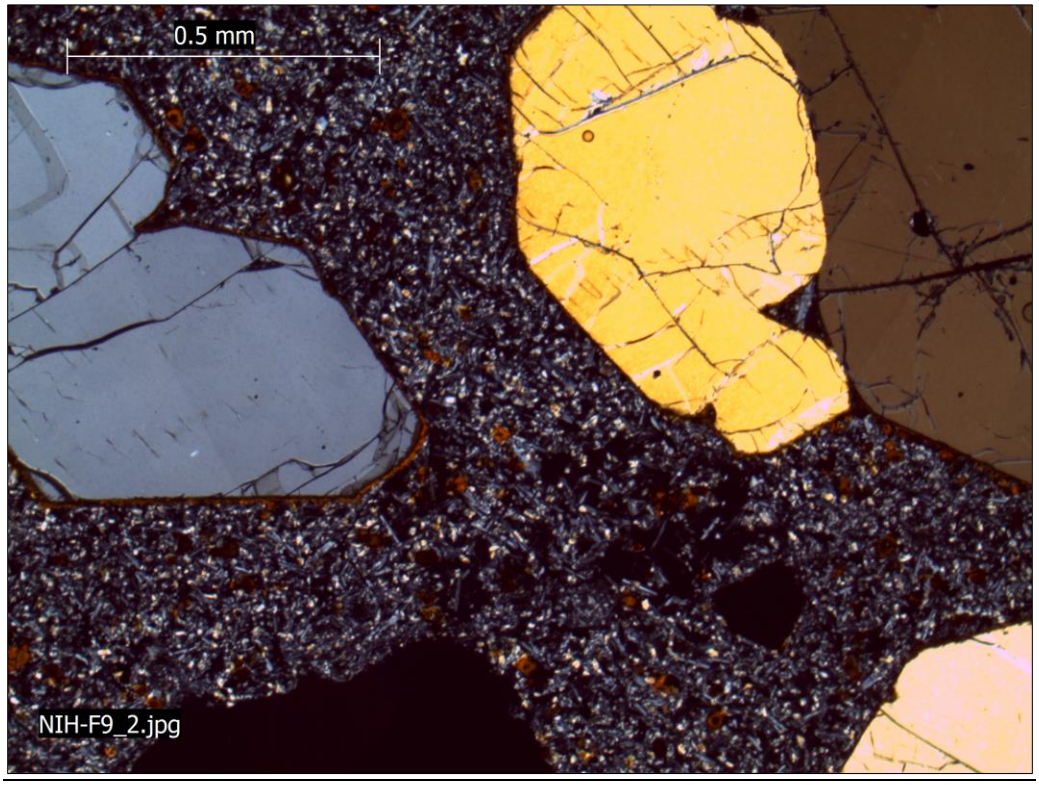

Nīhoa; NIH-W-11

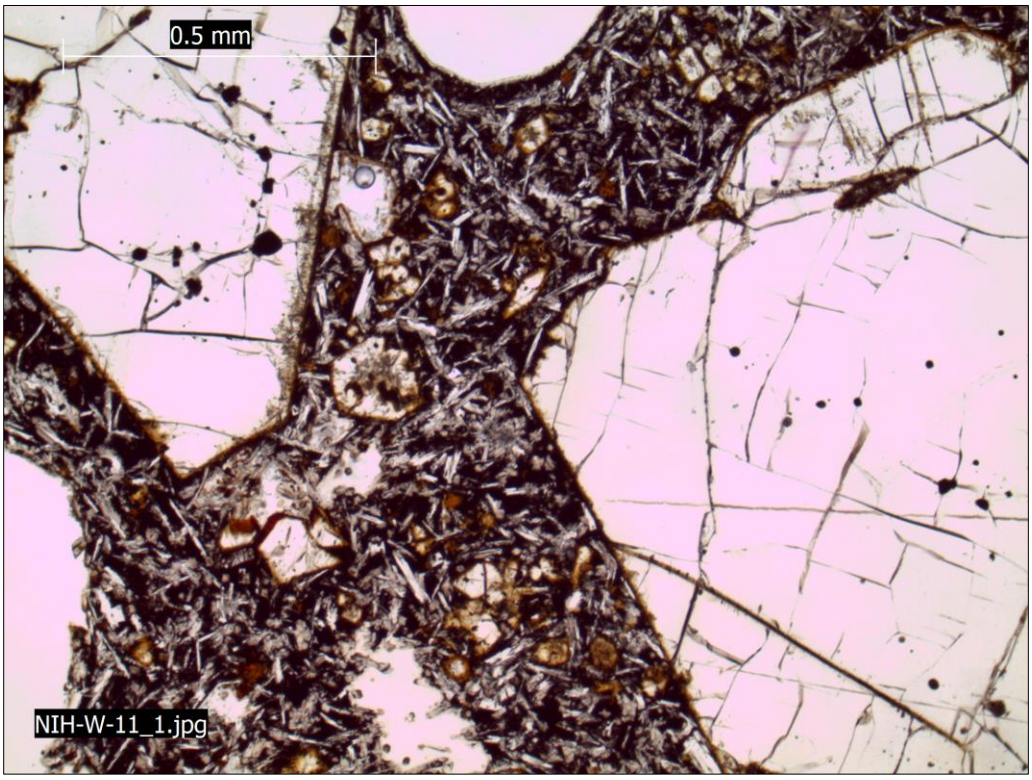

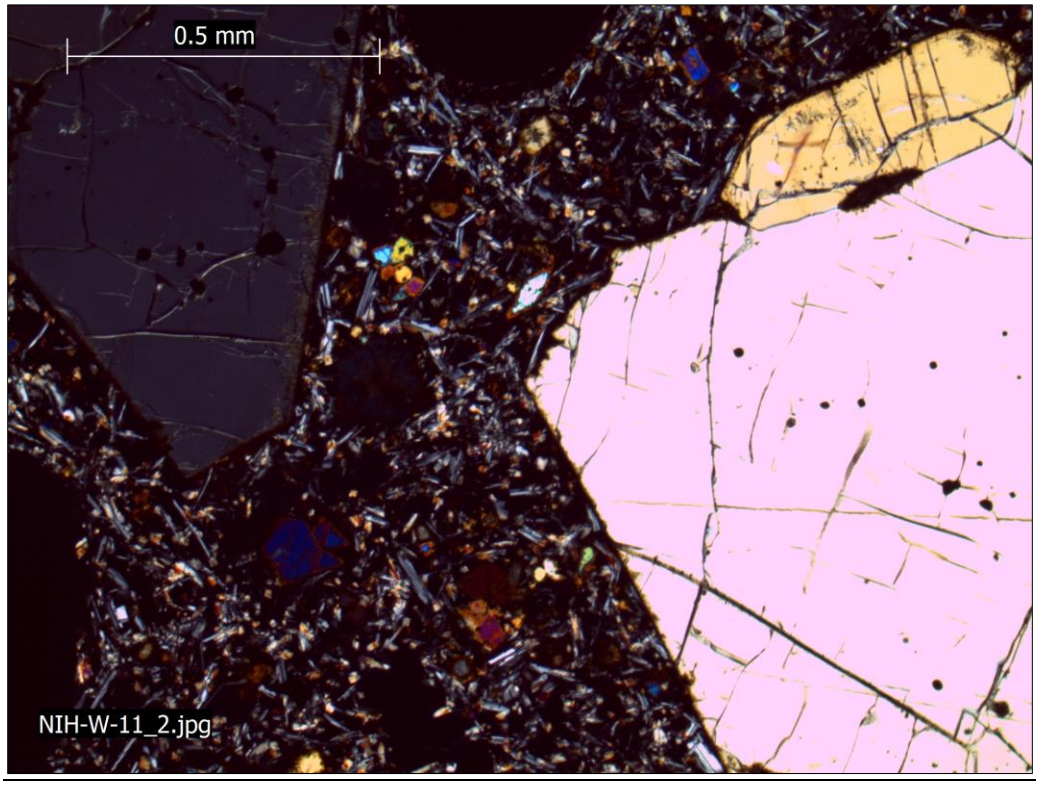

Kauaʻi; KV04-16

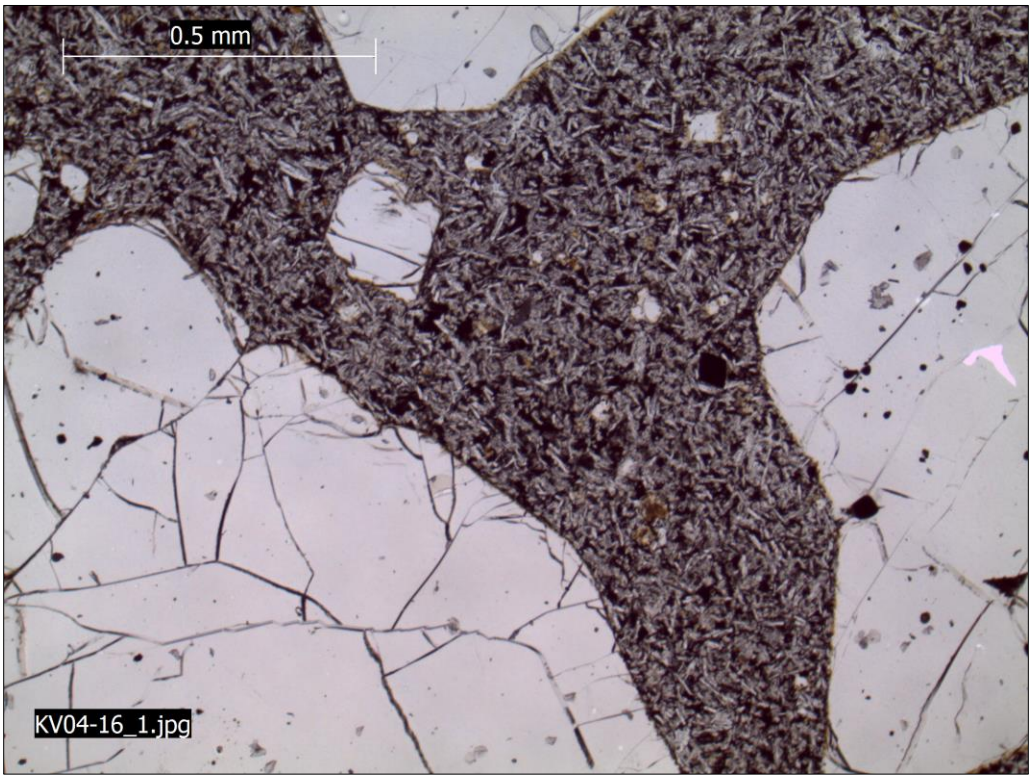

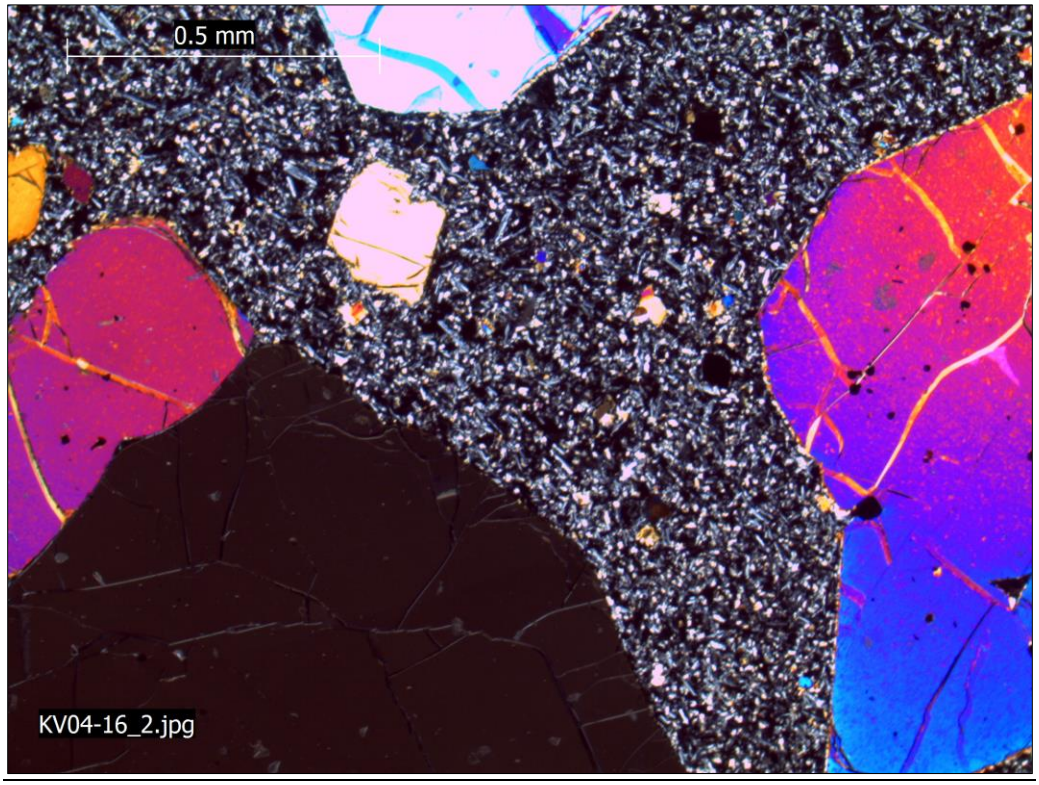

Kauaʻi; KV04-19

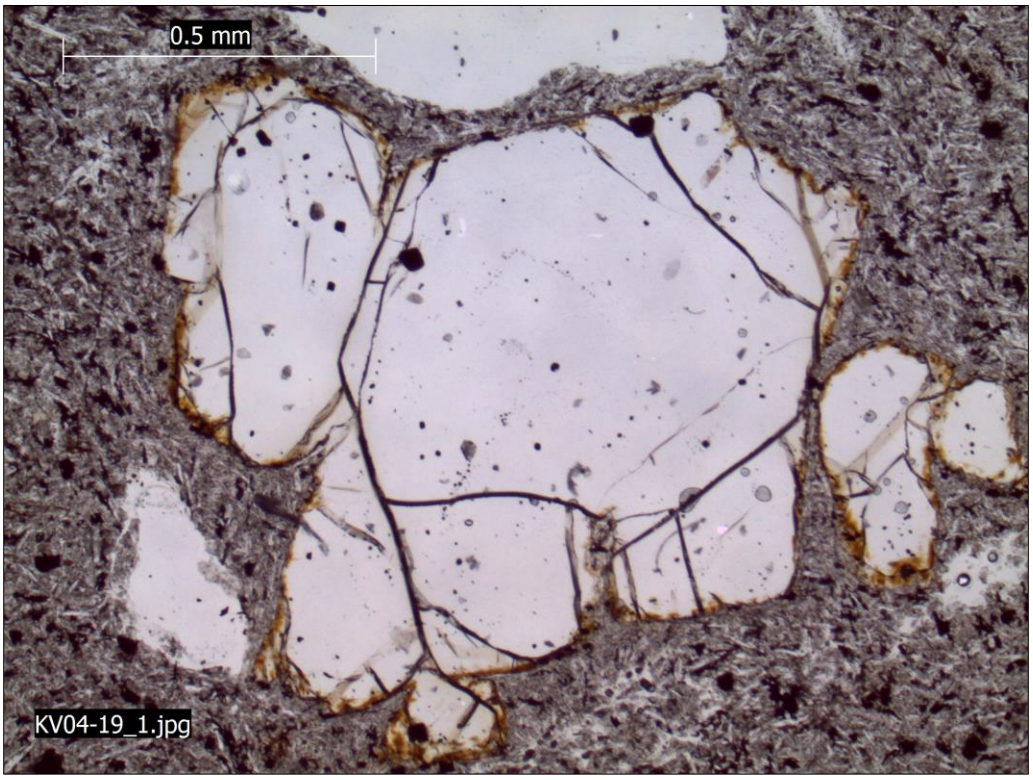

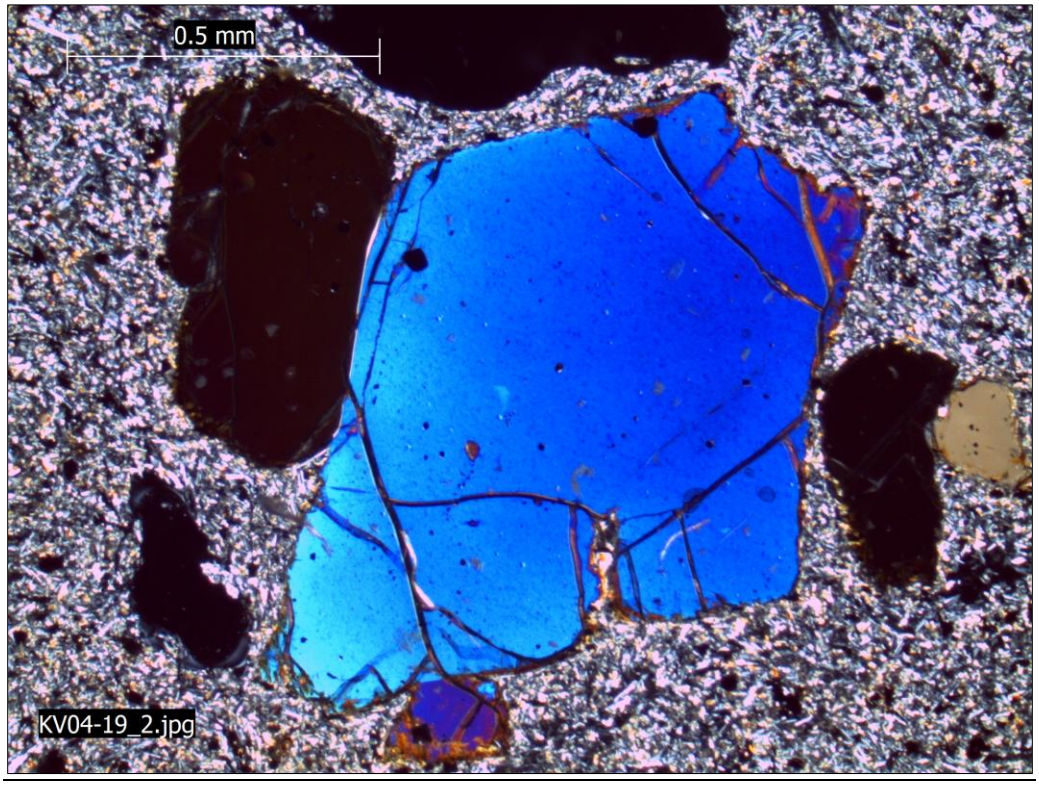

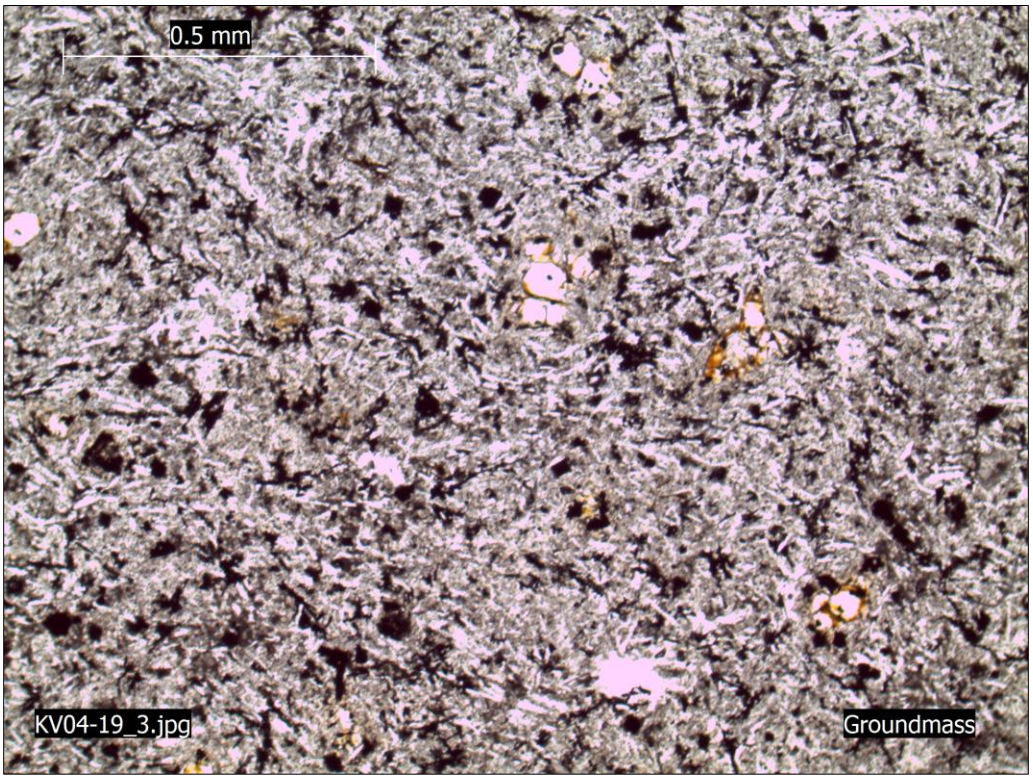
0.5 mm
KV04-19_3.jpg
Groundmass

Kauaʻi; KV04-22

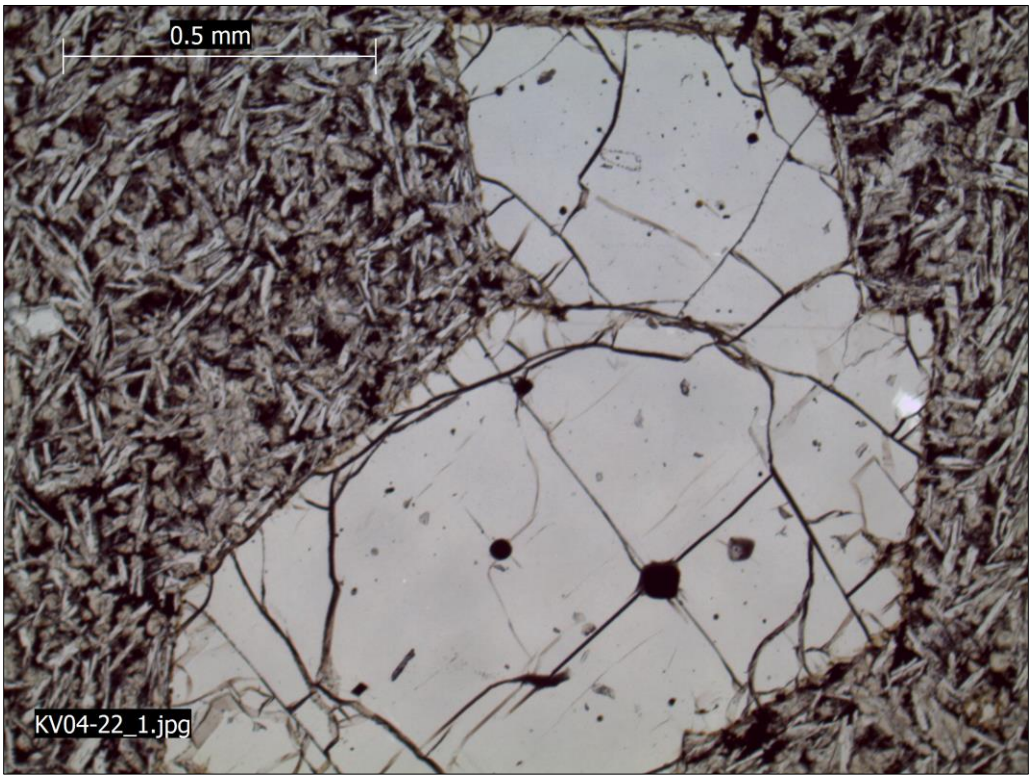

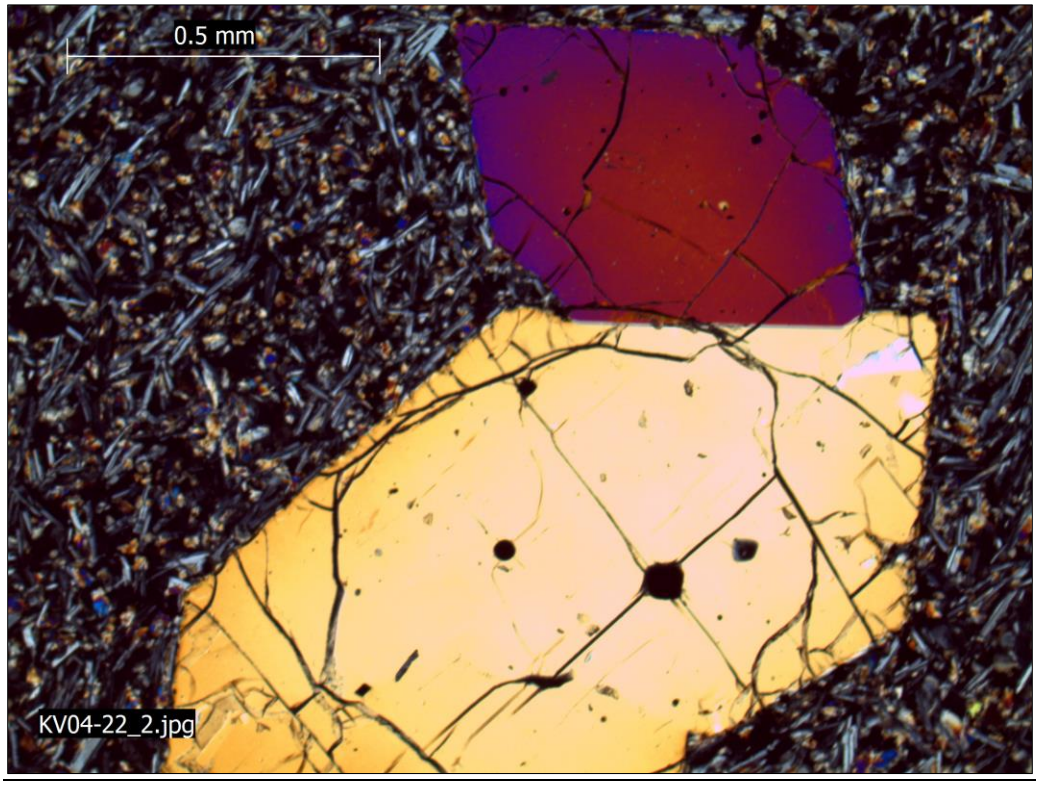

2) Sample preparation for XRF

All of these samples contain an alteration rim. The thickness of the alteration rim ranges from 1-4 cm. Submarine samples also have manganese encrustations (typically 0.1 - 1 cm thick). Manganese coating and alteration rim were removed prior to sample preparation. The least altered portion of the samples were coarsely crushed (1-8 mm) between tungsten-carbide (WC) coated plates in a hydraulic press. Crushed material was ultrasonically cleaned in Millipore water and dried for 24 hours at 70 ^{o}C. Cleaned material was hand-picked to remove altered fragments with discolored matrix material, vesicles filled by zeolites and/or calcite and pieces with extensive iddingsite had replacement of olivine phenocrysts. The freshest materials from these samples were powdered using a WC lined ring mill.

---

3) Monte Carlo simulation and equations

Three potential parental magma candidates were calculated for each sample using the K_d values of 0.315, 0.345, and 0.375. The three parental magma compositions are used to construct a synthetic sample of 10^6 using a Gaussian distribution. For each chemical component X, the mean and standard deviation of a normal distribution was constructed with the following equations:

$$\mu_i^{liq}\left(X_i^{liq}\right) = X_i^{liq}(K_d = 0.345)$$

$$\sigma_i^{liq}\left(X_i^{liq}\right) = \frac{\left|X_i^{liq}(K_d = 0.315) - X_i^{liq}(K_d = 0.345)\right| + \left|X_i^{liq}(K_d = 0.315) - X_i^{liq}(K_d = 0.345)\right|}{4}$$

A Gausian distribution using these statistical parameters is then constructed as:

$$\{X_i^{liq}\} \sim Normal\ (\mu_i^{liq}\ ,\ \sigma_i^{liq})$$

Where μ_i^{liq} and σ_i^{liq} are the mean and standard deviation of chemical component X_i^{liq} in the parental magma (i.e. X_{MgO}^{liq} (K_d = 0.345) = MgO in wt. % from the parental magma composition).

The same general formulation is used to construct the Gaussian distributions of olivine compositions:

$$\mu_i^{ol}(X_i^{ol}) = X_i^{ol}$$

$$\sigma_i^{liq}(X_i^{liq}) = RMS(X_i^{ol})$$

$$\{X_i^{ol}\} \sim Normal\ (\mu_i^{ol}\ ,\ \sigma_i^{ol})$$

Where μ_i^{ol} and σ_i^{ol} are the mean and standard deviation of chemical component X_i^{ol} for the highest forsterite olivine from each lava in wt. %. RMS is the root mean squared error in measurement of chemical component X_i^{ol}. This statistical construct confines ≥ 95% of the possible concentrations of each chemical component between the range defined by the compositions of the parental magmas calculated using K_d = 0.315 and 0.375, which are assumed to be the end-member compositions possible for a given sample (Figures A.1 and A.2). The Kd = 0.345 ± 0.030 is from Matzen et al., (2011). The K_d ± 0.030 is more than 3σ found by Matzen et al., (2011; 1σ = 0.009). From each compositional component distribution, 10^6 samples are drawn (Figures A.1 & A.2). These parental magmas are used in calculation of olivine-liquid temperature ($T^{ol\text{-}liq}$) using the olivine-liquid thermometer of Putirka et al., (2007; Eqn. 1).

Pressure and melt fraction are the greatest source of uncertainty when correcting for mantle potential temperatures (Putirka, 2008). Two approaches were used to estimate these parameters and evaluate the uncertainty inherent in each approach. The first method obtained a sample from a Gaussian distribution with a mean of 3 GPa, and a standard deviation of 0.15 GPa. Using the estimated parental magma compositions and pressure estimates, 10^6 $T^{ol\text{-}liq}$ possibilities are calculated (Appendix Eqn. 1; Appendix Figure A.3). Using these samples of $T^{ol\text{-}liq}$ and pressure, iterations over 10^6 samples obtained from five melt fraction Gaussian distributions defined by mean values of 8-24% with a standard deviation of 1% were used to calculate mantle potential temperatures (Figure A.3).

The second method calculated pressure using the Si-activity barometer of Putirka (2008, Eqn. 2). Using the estimated parental magma compositions and pressure estimates, 10^6 $T^{ol\text{-}liq}$ possibilities are calculated using the olivine-liquid thermometer of Putirka (2007; Eqn. 1). These olivine-liquid temperatures and pressures are used to solve for melt fraction using Eqn. (5) and then calculate the potential temperature.

Each of the variations in this approach yields six potential temperature distributions representing different melting characteristics for each sample. Using these distributions of olivine–liquid and mantle potential temperatures, the mean and standard deviation are calculated for each variation (Table A.2; Figure A.3). Potential temperature was calculated using the formulation of Putirka et al. (2007) to make comparisons with published potential temperatures in the main Hawaiian Islands as well as Putirka (2016) since it has been recently shown that the previous estimation of T_p could be overestimated using the thermodynamic properties of the Putirka et al. (2007) formulation (Putirka, 2016).

EQUATIONS

Olivine-liquid thermometer of Putirka et al. (2007)

$$Eqn\ (1)$$

$$= \frac{T^{ol-liq}\{15294.6 + 1318.8[P(GPa)] + 2.4834[P(GPa)]^2\}}{\left\{8.048 + 2.8352\left(ln\left[D_{Mg}^{\frac{ol}{liq}}\right]\right) + 2.097\left(ln[1.5C_{NM}^{liq}]\right) + 2.575\left(ln\left[3C_{SiO_2}^{liq}\right]\right) - 1.41(NF) + 0.222H_2O^{liq} + 0.5[P(GPa)]\right\}}$$

Where *P* is pressure of melt generations in GPa and is solved for iteratively using Eqn. (2); $D_{Mg}^{\frac{ol}{liq}} = X_{MgO}^{ol}/X_{MgO}^{liq}$ is the distribution coefficient of MgO in the olivine and liquid phases; X_i^j is the cation fraction of chemical component *i* in phase *j*; $C_{NM}^{liq} = X_{MgO}^{liq} + X_{MnO}^{liq} + X_{FeO}^{liq} + X_{CaO}^{liq} + X_{CoO}^{liq} + X_{NiO}^{liq}$ are the network modifying cation concentrations; $NF = \frac{7}{2}\left[\ln\left(1 - X_{AlO_{1.5}}^{liq}\right)\right] + 7\left[\ln\left(1 - X_{TiO_2}^{liq}\right)\right]$ are the network forming cation concentrations; $C_{SiO_2}^{liq} = X_{SiO_2}^{liq}$; H_2O^{liq} is in wt. %.

Si-activity barometer of Putirka (2008)

$$a_{SiO_2}^{liq} = \left(X_{SiO_2}^{liq}\right)^{-2}\left(1 - X_{AlO_{1.5}}^{liq}\right)^{7/2}(1 - X_{TiO_2}^{liq})^7 \quad Eqn(2)$$

$$P(kbar) = 231.5 + 0.186T^{ol-liq}(C°)0.124 + T^{ol-liq}(C°)\ln\left(a_{SiO_2}^{liq}\right) - 528.5\left(a_{SiO_2}^{liq}\right)^{1/2} + 13.3\left(X_{TiO_2}^{liq}\right) + 69.9\left(X_{NaO_{0.5}}^{liq}X_{KO_{0.5}}^{liq}\right) + 77.3\left(\frac{X_{AlO_{1.5}}^{liq}}{X_{AlO_{1.5}}^{liq} + X_{SiO_2}^{liq}}\right) \quad Eqn\ (3)$$

Where X_i^j is the cation fraction of chemical component *i* in phase *j;* $a_{SiO_2}^{liq}$ is calculated using Eqn. (2).

Potential Temperature Equations of Putirka (2007)

$$T_p(℃) = T^{ol-liq} + \Delta T_{fus} - P\frac{\partial T}{\partial P} \quad Eqn\ (4)$$

Where T_p is the mantle potential temperature T^{ol-liq} is the temperature calculated in °C from Eqn. (1); $\Delta T_{fus} = F[\frac{\Delta H_{fus}}{C_p}]$ is the temperature change due to partial melting, $F$is the melt fraction,

Potential Temperature Variable Equations of Putirka (2016)

$$F = \frac{(T^{ol-liq} + 5.14P^2 - 132.9P - 1120.7)}{(465.3 + 233.7P^{0.5} + 5.14P^2 - 132.9P)} \quad Eqn\ (5)$$

where T and P are in units of °C , C_p is the heat capacity for peridotite calculated using Eqn (6); and GPa.. ΔH_{fus} is the heat of fusion and is calculated using Eqn. (7).

$$C_p\left(\frac{J}{mole}\right) = 130 + 11.4\ln\left[T^{ol-liq}(°C)\right] \qquad Eqn\ (6)$$

Equation 7 yields C_p of 211.29 – 215.45 J/mole for temperatures of 1250-1800°C.

$$\Delta H_{fus}^{peridotite}\left(\frac{kJ}{mole}\right) = 21.1 + 0.061T^{ol-liq}(°C)7.6x10^{-5}[T^{ol-liq}(°C) - 1600]^2 \qquad Eqn\ (7)$$

Equation 7 yields $\Delta H_{fus}^{peridotite}$ of 88-128 kJ/mole for temperatures of 1250-1800°C.

$$\frac{\partial T}{\partial P} = \frac{T\alpha V}{C_p} = 13.3\ \frac{C°}{GPa} \qquad Eqn\ (8)$$

where *T* is temperature in °C, *P* is pressure in GPa, and α is the coefficient of thermal expansion *V* is the molar volume of olivine.

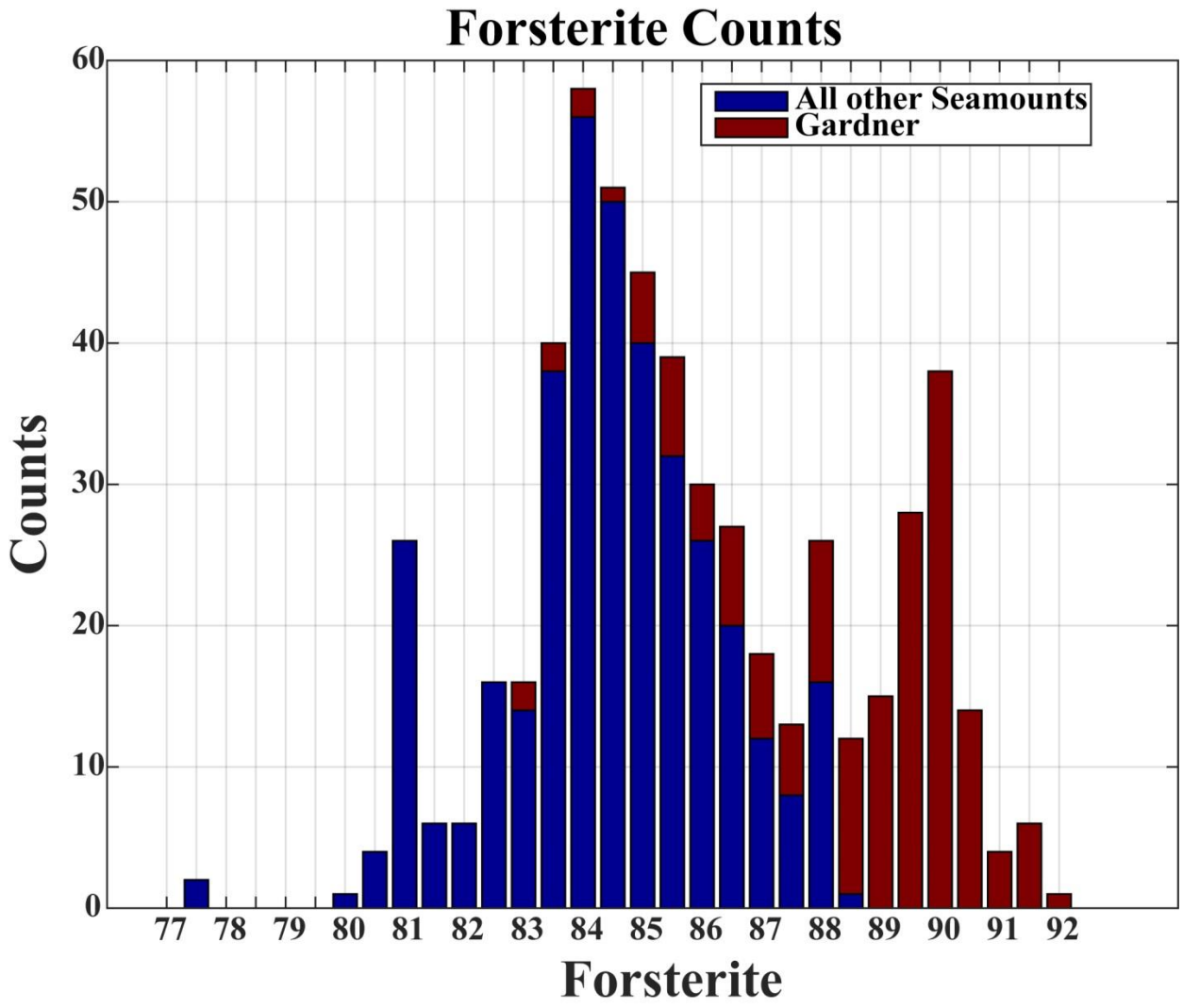

Figure A.1. Histogram showing the distribution of all 540 olivine core analyses with the olivine analyses in lavas from Gardner separated out from the rest of the analyses. The most frequent forsterite measured were 83.75-84.25 with a peak at 80.75-81.25 due to a high frequency of olivines measured between that range from the Nīhoa lavas. The bimodal distribution at higher forsterite >88 is due to the high frequency of olivines with >88 Fo measured in Gardner lavas.

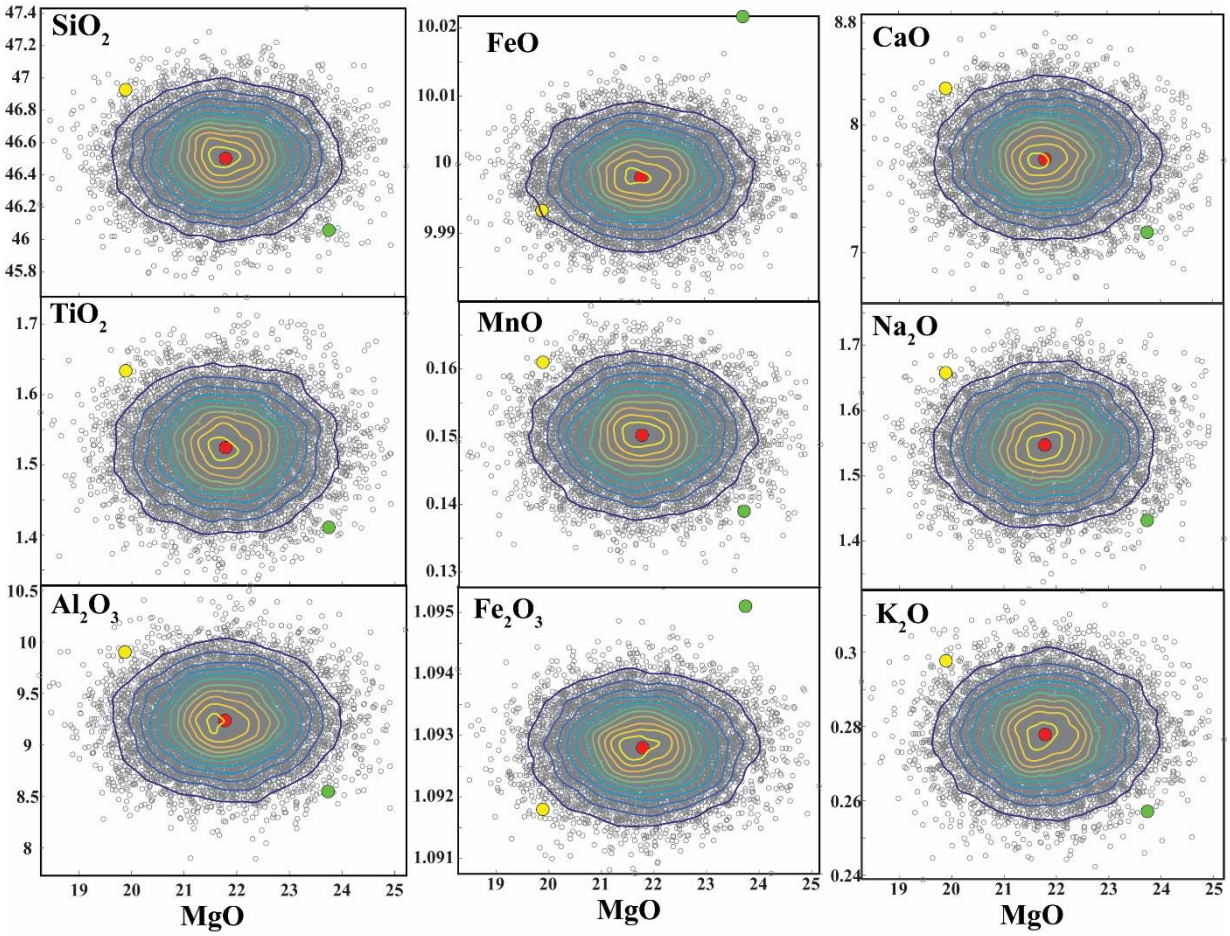

Figure A.2. Data density contoured at relative intervals in MgO variation diagrams from the Gardner sample 76-6-7-H simulation of 10^6 sampled parental magmas. The yellow, red and green circles are the compositions derived from the reverse fractionation modelling using a K_d = 0.315, 0.345, and 0.375 respectively.

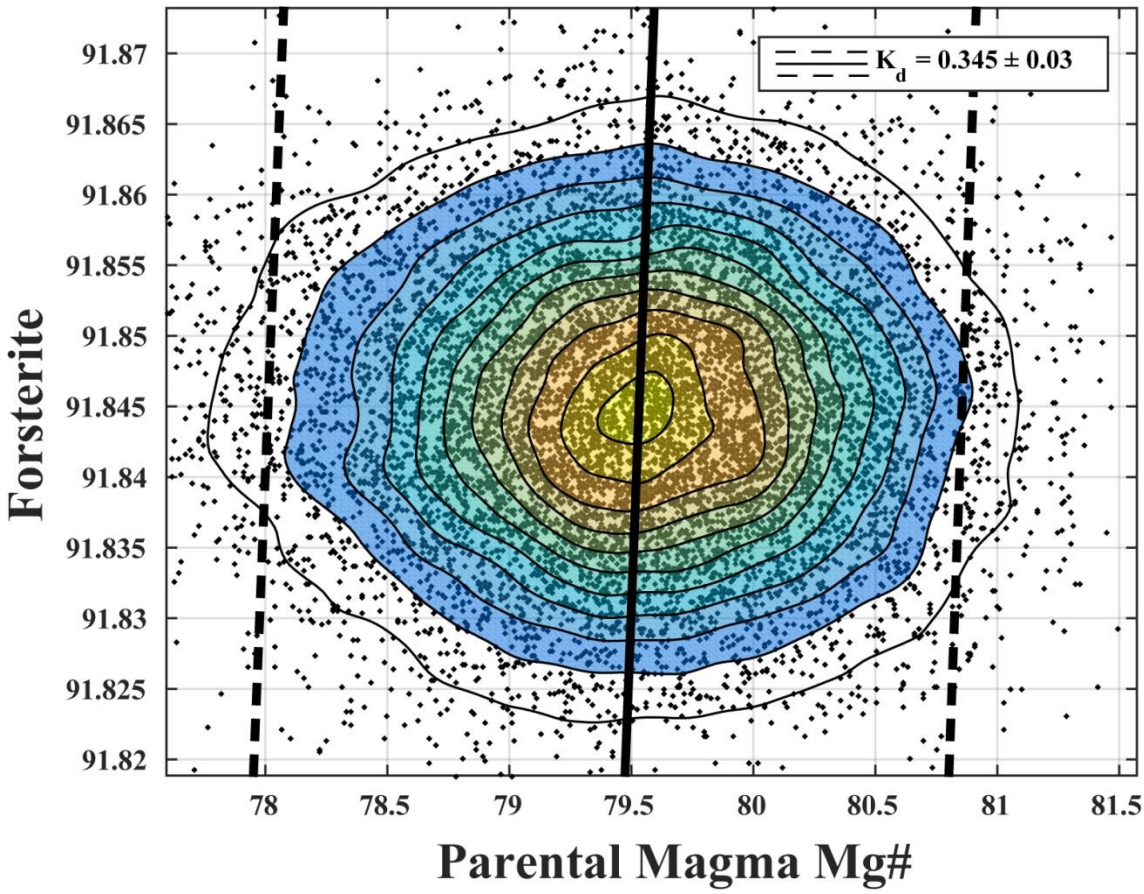

Figure A.3. Data density contoured plot of parental magma MgO # and olivine forsterite plotted on the Rhodes diagram from the 76-6-7-H simulation of 10^6 sampled parental magmas (black dots are individual simulated compositions). Mg # = mol % Mg/(Mg+Fe). Note that the peak of the data density lies directly under the line of K_d=0.345, and >95% of the data points lie within the array defined by $K_d = 0.345 \pm 0.030$, assuring that the samples drawn from the Gaussian distributions from these calculated parental magmas are truly possible equilibrium compositions. The $K_d = 0.345 \pm 0.030$ is from Matzen et al., 2011. The $K_d \pm 0.030$ is more than 3σ found by Matzen et al., (2011; 1σ = 0.009).

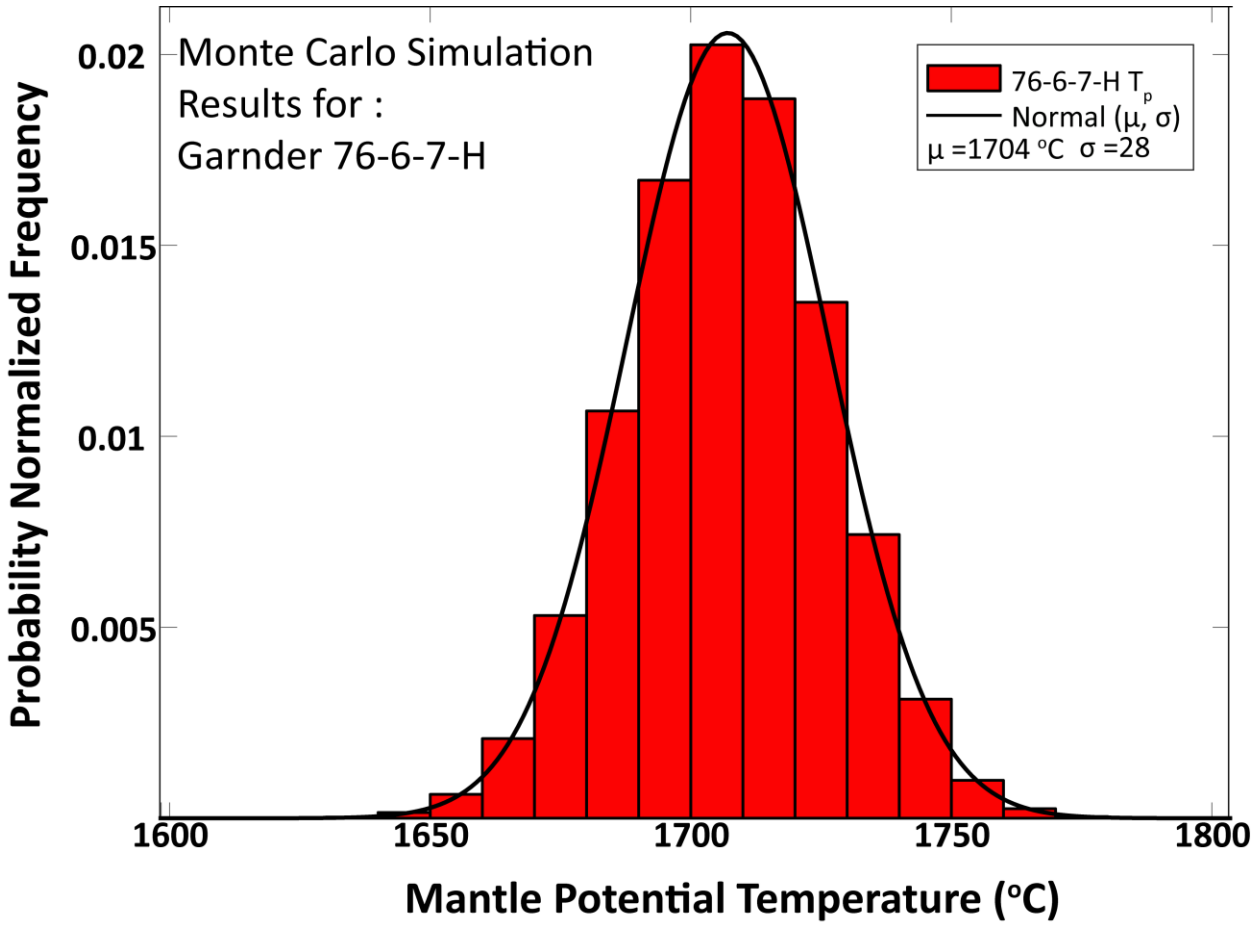

Figure A.4. Probability normalized frequency histograms with the Gaussian distribution plotted (red) defined by the mean and standard deviation that was calculated from the sample distribution of T_p derived from the synthetic samples.

5) Olivine-liquid temperatures and mantle potential temperature results

The temperatures reported in the main text are for olivines from the samples that yielded the maximum temperatures at each volcano (Table 7). Table A.1 summarizes each $T^{ol\text{-}liq}$ and T_p result for the 25 samples obtained from different combinations of pressure and melt fraction made when calculating temperatures using for each sample. Tp estimates calculated using the formulation of Putirka et al. (2007) and Putirka (2016). For each sample, the first five temperature estimates show the resulting temperature assuming 3.00 GPa pressure and 8-24 % melt fraction. The sixth temperature estimate shows the pressure obtained from the Si- barometer (Eqns. 2 & 3) and the calculated melt fraction (Eqn. 5).

TABLE A.1 OLIVINE-LIQUID TEMPERATURES AND MANLTE POTENTIAL TEMPERATURES FOR ALL SAMPLES

Seamount	Sample	P	F	$\mu T^{ol\text{-}liq}$	1σ	$\mu T_{p\ (2007)}$	1σ	$\mu T_{p\ (2015)}$	1σ
Daikakuji	A-55-1-6	3.00	0.08	1425	14	1439	20	1425	17
			0.12	1425	14	1466	20	1445	17
			0.16	1425	14	1493	20	1465	18
			0.20	1425	14	1521	21	1485	18
			0.24	1425	14	1548	22	1504	18
		1.16	0.12	1335	13	1400	28	1374	24
	A-55-2-3	3.00	0.08	1417	15	1432	20	1417	18
			0.12	1417	15	1459	20	1437	18
			0.16	1417	15	1486	21	1456	18
			0.20	1417	15	1513	22	1476	18
			0.24	1417	15	1540	22	1496	19
		1.15	0.11	1327	14	1383	30	1360	25
	A-55-4-12	3.00	0.08	1419	15	1433	20	1419	18
			0.12	1419	15	1460	20	1438	18
			0.16	1419	15	1487	21	1458	18
			0.20	1419	15	1514	22	1478	18
			0.24	1419	15	1541	22	1498	19
		1.12	0.11	1327	13	1388	30	1363	25
Unnamed	84-28-C-17	3.00	0.08	1481	16	1495	21	1482	19
			0.12	1481	16	1522	21	1503	19
			0.16	1481	16	1549	22	1523	19
			0.20	1481	16	1576	22	1544	19
			0.24	1481	16	1603	23	1565	20
		2.58	0.06	1461	15	1467	34	1458	29
	84-28-D-20	3.00	0.08	1484	16	1498	21	1486	19
			0.12	1484	16	1525	21	1507	19
			0.16	1484	16	1553	22	1527	19
			0.20	1484	16	1580	22	1548	20
			0.24	1484	16	1607	23	1569	20
		2.43	0.03	1458	15	1482	34	1468	29
Academician Berg	72-20-GG-19	3.00	0.08	1505	15	1519	20	1507	18
			0.12	1505	15	1546	20	1528	18
			0.16	1505	15	1573	21	1549	18
			0.20	1505	15	1600	21	1570	18
			0.24	1505	15	1628	22	1591	19
		2.46	0.12	1480	13	1528	31	1509	27

TABLE A.1 CONT.

Seamount	Sample	P	F	μ $T^{ol\text{-}liq}$	1σ	μ $T_{p\ (2007)}$	1σ	μ $T_{p\ (2015)}$	1σ
Pioneer	P5-526-rk2-10	3.00	0.08	1530	16	1545	21	1533	19
			0.12	1530	16	1572	21	1555	19
			0.16	1530	16	1599	21	1576	19
			0.20	1530	16	1626	22	1597	19
			0.24	1530	16	1653	23	1619	19
		2.66	0.15	1515	14	1578	33	1557	29
Gardner	76-6-7-B-14	3.00	0.08	1542	15	1557	20	1546	18
			0.12	1542	15	1584	20	1567	18
			0.16	1542	15	1611	21	1589	18
			0.20	1542	15	1638	21	1610	18
			0.24	1542	15	1665	22	1632	18
		2.47	0.19	1518	13	1612	30	1585	26
	76-6-7-C-6	3.00	0.08	1556	14	1570	20	1559	18
			0.12	1556	14	1597	20	1581	18
			0.16	1556	14	1624	20	1602	18
			0.20	1556	14	1651	21	1624	18
			0.24	1556	14	1678	22	1646	18
		2.61	0.20	1538	13	1637	30	1609	26
	76-6-7-F-27	3.00	0.08	1558	10	1572	17	1561	14
			0.12	1558	10	1599	17	1583	15
			0.16	1558	10	1626	18	1604	15
			0.20	1558	10	1653	19	1626	15
			0.24	1558	10	1680	20	1648	15
		2.65	0.20	1542	8	1641	20	1613	17
	76-6-7-H-11	3.00	0.08	1605	15	1619	20	1610	18
			0.12	1605	15	1646	20	1632	18
			0.16	1605	15	1673	21	1654	18
			0.20	1605	15	1701	21	1676	19
			0.24	1605	15	1728	22	1699	19
		3.21	0.24	1614	13	1731	32	1703	28
	76-6-7-I-27	3.00	0.08	1585	14	1599	20	1589	18
			0.12	1585	14	1626	20	1611	18
			0.16	1585	14	1653	21	1633	18
			0.20	1585	15	1680	21	1655	18
			0.24	1585	14	1707	22	1677	18
		2.87	0.23	1579	13	1695	31	1666	27

TABLE A.1 CONT.

Seamount	Sample	P	F	μ $T^{ol\text{-}liq}$	1σ	μ $T_{p\ (2007)}$	1σ	μ $T_{p\ (2015)}$	1σ
Gardner	76-6-7-J-30	3.00	0.08	1562	14	1576	20	1566	18
			0.12	1562	14	1603	20	1587	18
			0.16	1562	14	1630	20	1609	18
			0.20	1562	14	1658	21	1631	18
			0.24	1562	14	1685	22	1653	18
		2.56	0.22	1542	13	1654	30	1624	26
Mokumanamana	NEC-2A-18	3.00	0.08	1508	14	1522	20	1510	17
			0.12	1508	14	1549	20	1531	18
			0.16	1508	14	1576	20	1552	18
			0.20	1508	14	1603	21	1573	18
			0.24	1508	14	1630	22	1594	18
		1.94	0.16	1466	13	1547	29	1521	25
	NEC-3A-2	3.00	0.08	1483	15	1497	20	1484	18
			0.12	1483	15	1524	20	1505	18
			0.16	1483	15	1551	21	1526	18
			0.20	1483	15	1578	21	1546	18
			0.24	1483	15	1605	22	1567	18
		1.70	0.13	1432	13	1497	30	1473	25
Twin Banks	P5-688-1-20	3.00	0.08	1547	13	1561	18	1550	16
			0.12	1547	13	1588	19	1572	16
			0.16	1547	13	1615	19	1593	16
			0.20	1547	13	1642	20	1615	17
			0.24	1547	13	1669	21	1636	17
		2.86	0.16	1541	11	1608	26	1587	22
West Nīhoa	76-9-11-10	3.00	0.08	1503	15	1517	20	1505	18
			0.12	1503	15	1544	20	1526	18
			0.16	1503	15	1571	21	1547	18
			0.20	1503	15	1598	22	1568	19
			0.24	1503	15	1625	22	1589	19
		2.11	0.20	1441	14	1551	31	1517	27
Nīhoa	NIH-D1-2-19	3.00	0.08	1459	15	1473	20	1460	18
			0.12	1459	15	1500	20	1480	18
			0.16	1459	15	1527	21	1501	18
			0.20	1459	15	1554	21	1521	18
			0.24	1459	15	1582	22	1541	18
		1.49	0.14	1386	13	1461	30	1434	25

TABLE A.1 CONT.

Seamount	Sample	P	F	μ $T^{ol\text{-}liq}$	1σ	μ $T_{p\ (2007)}$	1σ	μ $T_{p\ (2015)}$	1σ
Nīhoa	NIH-D4-19	3.00	0.08	1404	27	1418	31	1403	30
			0.12	1403	27	1445	31	1422	30
			0.16	1404	27	1472	31	1442	30
			0.20	1403	27	1499	32	1461	31
			0.24	1404	27	1526	32	1481	31
		1.14	0.08	1312	27	1353	59	1335	49
	NIH-F-5A-9	3.00	0.08	1537	15	1551	20	1540	18
			0.12	1537	15	1578	20	1561	18
			0.16	1537	15	1605	21	1583	18
			0.20	1537	15	1632	21	1604	18
			0.24	1537	15	1659	22	1626	19
		2.42	0.18	1510	13	1601	31	1574	27
	NIH-F-9-4	3.00	0.08	1563	15	1577	20	1567	18
			0.12	1563	15	1604	20	1588	18
			0.16	1563	15	1631	21	1610	18
			0.20	1563	15	1658	21	1632	18
			0.24	1563	15	1686	22	1654	19
		2.22	0.25	1527	13	1668	32	1632	27
	NIH-W-11-1-6	3.00	0.08	1481	19	1495	23	1483	21
			0.12	1481	19	1522	23	1503	21
			0.16	1481	19	1550	24	1524	22
			0.20	1481	19	1577	24	1545	22
			0.24	1481	19	1604	25	1566	22
		2.55	0.06	1460	17	1470	39	1460	34
Kaua‘i	KV04-16-01	3.00	0.08	1531	12	1545	18	1533	16
			0.12	1531	12	1572	18	1555	16
			0.16	1531	12	1599	19	1576	16
			0.20	1531	12	1626	20	1598	16
			0.24	1531	12	1653	21	1619	16
		2.10	0.20	1489	10	1599	25	1567	21
	KV04-19-01	3.00	0.08	1461	14	1475	20	1462	17
			0.12	1461	14	1502	20	1482	18
			0.16	1461	14	1529	20	1503	18
			0.20	1461	14	1556	21	1523	18
			0.24	1461	14	1584	22	1544	18
		1.52	0.14	1390	13	1464	29	1437	25

TABLE A.1 CONT.

Seamount	Sample	P	F	μ $T^{ol\text{-}liq}$	1σ	μ $T_{p\ (2007)}$	1σ	μ $T_{p\ (2015)}$	1σ
Kaua‘i	KV04-22-15	3.00	0.08	1492	15	1506	20	1494	18
			0.12	1492	15	1533	20	1515	18
			0.16	1492	15	1560	21	1536	18
			0.20	1492	15	1587	21	1556	18
			0.24	1492	15	1615	22	1577	18
		1.81	0.16	1436	13	1523	30	1494	26

6) Olivine EPMA compositions and analytical error

Analyses were made for 539 euhedral to subhedral olivine crystals in 25 samples from the NWHR. The compositions of olivine (measured in weight percent oxides) and the forsterite content for each sample are reported in Table A.2. Samples are organized from oldest to youngest volcano, the same as reported in Table 1 (from Daikakuji to Kauai). Each analysis number is appended to the sample name (i.e., Gardner sample: 76-6-7-H-15 is the fifteenth olivine analysis of sample 76-6-7-H). The root-mean-squared (RMS) error in weight percent oxides compositions was calculated during a single analysis session (Table A.3). Each analysis session corresponds to a single calibration prior to measurements of unknowns. Thus, the RMS that is calculated for each oxides is representative of >1 of the lavas (see description in Section 5; Table 3).

TABLE A.2 OLIVINE COMPOSTIONS IN WEIGHT PERCENT

Seamount	Sample	SiO_2	FeO	NiO	MnO	MgO	CaO	Total	Fo
Daikakuji	A-55-1-1	39.05	17.76	0.29	0.22	41.55	0.23	99.10	80.66
	A-55-1-4	39.67	14.85	0.45	0.18	44.05	0.19	99.38	84.09
	A-55-1-5	39.54	15.40	0.41	0.18	43.66	0.19	99.39	83.48
	A-55-1-6	39.64	14.50	0.47	0.17	44.08	0.19	99.05	84.42
	A-55-1-7	39.30	16.14	0.39	0.19	42.92	0.20	99.13	82.58
	A-55-1-8	39.48	15.23	0.41	0.19	43.65	0.19	99.14	83.63
	A-55-1-9	39.50	14.95	0.45	0.17	43.75	0.20	99.02	83.92
	A-55-1-10	39.35	14.92	0.43	0.18	44.07	0.19	99.13	84.04
	A-55-1-11	39.45	14.67	0.40	0.18	44.29	0.20	99.19	84.33
	A-55-1-14	39.03	16.77	0.32	0.20	42.67	0.21	99.20	81.93
	A-55-1-15	39.25	16.62	0.38	0.20	43.06	0.20	99.72	82.20
	A-55-1-16	39.00	17.34	0.38	0.19	41.89	0.19	99.01	81.15
	A-55-1-17	39.10	16.96	0.32	0.21	42.64	0.22	99.44	81.76
	A-55-1-18	39.52	14.60	0.46	0.18	44.29	0.18	99.23	84.39
	A-55-1-20	39.21	16.26	0.34	0.21	43.05	0.21	99.27	82.52
	A-55-2-3	39.75	15.22	0.45	0.19	44.19	0.19	99.98	83.81
	A-55-2-4	39.41	15.80	0.38	0.19	43.83	0.21	99.82	83.18
	A-55-2-5	39.44	16.10	0.40	0.19	43.64	0.19	99.97	82.85
	A-55-2-6	39.19	16.72	0.36	0.20	43.00	0.20	99.66	82.10
	A-55-2-7	39.28	15.97	0.37	0.19	43.44	0.20	99.44	82.90
	A-55-2-8	39.52	15.23	0.42	0.18	44.15	0.19	99.70	83.79
	A-55-2-9	39.56	15.39	0.44	0.19	44.11	0.19	99.88	83.63
	A-55-2-10	38.95	18.69	0.29	0.23	41.44	0.21	99.81	79.81
	A-55-2-11	39.27	16.07	0.38	0.19	43.48	0.20	99.58	82.83
	A-55-2-12	39.17	17.12	0.30	0.21	42.42	0.22	99.44	81.54

TABLE A.2 CONT.

Seamount	Sample	SiO_2	FeO	NiO	MnO	MgO	CaO	Total	Fo
Daikakuji	A-55-2-14	39.36	15.91	0.39	0.18	43.55	0.20	99.59	83.00
	A-55-2-15	39.37	16.18	0.40	0.19	43.69	0.19	100.03	82.80
	A-55-2-16	39.03	16.80	0.36	0.20	42.67	0.19	99.25	81.91
	A-55-2-17	39.30	17.38	0.30	0.22	42.59	0.22	100.00	81.37
	A-55-2-18	39.28	16.41	0.36	0.20	43.26	0.20	99.70	82.46
	A-55-2-19	38.89	17.97	0.29	0.22	41.97	0.23	99.56	80.63
	A-55-2-20	39.38	16.54	0.34	0.21	43.24	0.21	99.92	82.33
	A-55-4-1	39.33	15.24	0.44	0.18	44.26	0.19	99.64	83.81
	A-55-4-2	39.02	16.34	0.33	0.20	43.38	0.22	99.48	82.56
	A-55-4-3	39.04	16.19	0.35	0.20	43.33	0.21	99.33	82.67
	A-55-4-4	39.14	15.23	0.44	0.19	44.08	0.19	99.25	83.76
	A-55-4-5	39.28	15.53	0.39	0.19	43.96	0.20	99.55	83.46
	A-55-4-6	39.23	16.53	0.28	0.23	43.21	0.23	99.70	82.33
	A-55-4-7	39.11	15.55	0.38	0.19	43.95	0.20	99.38	83.44
	A-55-4-8	38.98	17.34	0.30	0.22	42.50	0.21	99.55	81.37
	A-55-4-9	39.08	17.37	0.38	0.21	42.64	0.19	99.87	81.40
	A-55-4-10	39.09	16.04	0.36	0.20	43.49	0.20	99.37	82.86
	A-55-4-11	39.25	15.58	0.41	0.18	43.98	0.19	99.60	83.42
	A-55-4-12	39.25	15.08	0.42	0.18	44.05	0.19	99.16	83.89
	A-55-4-13	39.03	17.12	0.31	0.21	42.84	0.21	99.72	81.68
	A-55-4-14	39.46	15.23	0.43	0.18	44.45	0.19	99.94	83.87
	A-55-4-15	39.26	15.41	0.40	0.19	44.10	0.20	99.56	83.61
	A-55-4-16	39.19	16.29	0.34	0.20	43.39	0.21	99.61	82.60
	A-55-4-17	39.03	15.31	0.40	0.19	43.82	0.20	98.94	83.62
	A-55-4-18	39.43	15.29	0.42	0.18	44.11	0.20	99.63	83.72
	A-55-4-19	39.38	15.44	0.41	0.19	44.00	0.20	99.63	83.55

TABLE A.2 CONT.

Seamount	Sample	SiO_2	FeO	NiO	MnO	MgO	CaO	Total	Fo
Daikakuji	A-55-4-20	39.31	15.26	0.43	0.19	44.31	0.19	99.69	83.81
Unnamed	84-28-C-1	39.49	14.37	0.22	0.24	44.69	0.44	99.45	84.72
	84-28-C-2	39.33	14.55	0.21	0.24	44.55	0.45	99.33	84.52
	84-28-C-3	39.56	13.43	0.22	0.21	45.56	0.43	99.42	85.81
	84-28-C-4	39.56	13.32	0.22	0.22	45.46	0.42	99.20	85.89
	84-28-C-5	39.52	14.39	0.22	0.24	44.86	0.43	99.65	84.75
	84-28-C-6	38.72	13.73	0.22	0.22	44.59	0.43	97.92	85.27
	84-28-C-7	39.15	14.36	0.21	0.24	44.71	0.44	99.11	84.73
	84-28-C-8	39.41	13.82	0.22	0.23	45.23	0.44	99.34	85.36
	84-28-C-9	39.77	13.52	0.22	0.23	45.54	0.42	99.71	85.72
	84-28-C-10	39.21	15.00	0.21	0.25	44.37	0.45	99.49	84.06
	84-28-C-11	39.24	14.76	0.21	0.25	44.55	0.45	99.46	84.33
	84-28-C-12	39.34	14.73	0.21	0.25	44.51	0.46	99.50	84.34
	84-28-C-13	39.31	14.86	0.21	0.24	44.55	0.46	99.61	84.24
	84-28-C-14	39.52	14.11	0.22	0.24	45.15	0.42	99.66	85.08
	84-28-C-15	38.91	14.84	0.21	0.27	43.41	0.44	98.08	83.91
	84-28-C-16	39.19	14.32	0.22	0.24	44.65	0.45	99.06	84.75
	84-28-C-17	39.75	13.11	0.23	0.21	46.02	0.38	99.70	86.22
	84-28-C-18	39.52	13.69	0.23	0.23	45.43	0.37	99.47	85.54
	84-28-C-19	39.38	14.33	0.22	0.24	44.83	0.45	99.45	84.79
	84-28-C-20	39.31	14.41	0.22	0.24	44.69	0.43	99.29	84.68
	84-28-D-1	39.50	14.16	0.22	0.23	44.83	0.46	99.39	84.95
	84-28-D-2	39.44	14.40	0.21	0.23	44.32	0.46	99.06	84.58
	84-28-D-3	39.46	14.24	0.21	0.23	44.58	0.49	99.21	84.81
	84-28-D-4	39.45	14.37	0.21	0.24	44.63	0.48	99.38	84.70
	84-28-D-5	39.51	14.30	0.22	0.23	44.68	0.48	99.41	84.78

TABLE A.2 CONT.

Seamount	Sample	SiO_2	FeO	NiO	MnO	MgO	CaO	Total	Fo
Unnamed	84-28-D-6	39.49	14.23	0.22	0.23	44.82	0.47	99.47	84.88
	84-28-D-7	39.64	14.27	0.21	0.23	44.63	0.47	99.46	84.79
	84-28-D-8	39.55	14.24	0.21	0.24	44.76	0.48	99.48	84.85
	84-28-D-9	39.66	14.27	0.21	0.23	44.74	0.47	99.58	84.83
	84-28-D-10	39.60	14.30	0.21	0.23	44.79	0.51	99.65	84.81
	84-28-D-11	39.45	14.23	0.21	0.23	44.81	0.47	99.40	84.88
	84-28-D-12	39.60	14.28	0.22	0.24	44.98	0.44	99.76	84.88
	84-28-D-13	39.69	14.20	0.22	0.23	45.02	0.47	99.84	84.96
	84-28-D-14	39.73	14.34	0.22	0.24	45.13	0.43	100.08	84.87
	84-28-D-15	39.48	14.29	0.21	0.24	45.02	0.45	99.69	84.88
	84-28-D-16	39.38	14.42	0.22	0.23	44.97	0.42	99.63	84.75
	84-28-D-17	39.48	14.40	0.22	0.24	44.62	0.45	99.41	84.67
	84-28-D-18	39.67	14.46	0.22	0.24	44.90	0.46	99.95	84.70
	84-28-D-19	39.47	14.53	0.21	0.23	44.80	0.46	99.70	84.61
	84-28-D-20	39.70	14.14	0.22	0.23	45.27	0.41	99.97	85.09
Academician Berg	72-20-GG-1	39.23	15.27	0.30	0.19	44.78	0.25	100.01	83.94
	72-20-GG-2	39.30	16.60	0.27	0.22	43.85	0.21	100.45	82.49
	72-20-GG-3	39.22	15.41	0.30	0.20	44.65	0.25	100.02	83.78
	72-20-GG-5	39.34	14.92	0.30	0.19	45.14	0.24	100.14	84.36
	72-20-GG-6	39.75	14.03	0.31	0.18	45.95	0.26	100.48	85.37
	72-20-GG-7	39.43	14.84	0.31	0.19	45.13	0.24	100.15	84.43
	72-20-GG-8	39.57	13.81	0.33	0.18	46.17	0.20	100.26	85.63
	72-20-GG-9	39.45	15.46	0.29	0.20	44.65	0.25	100.31	83.74
	72-20-GG-10	39.75	13.25	0.32	0.18	46.57	0.24	100.31	86.23
	72-20-GG-11	39.60	14.37	0.31	0.19	45.53	0.22	100.23	84.96
	72-20-GG-12	39.27	15.66	0.29	0.20	44.47	0.27	100.16	83.50

TABLE A.2 CONT.

Seamount	Sample	SiO_2	FeO	NiO	MnO	MgO	CaO	Total	Fo
Academician Berg	72-20-GG-13	39.31	15.11	0.30	0.20	44.88	0.26	100.05	84.11
	72-20-GG-14	39.36	15.17	0.30	0.20	44.93	0.26	100.21	84.08
	72-20-GG-15	39.72	14.59	0.31	0.19	45.55	0.25	100.60	84.77
	72-20-GG-16	39.62	14.63	0.31	0.19	45.46	0.25	100.45	84.70
	72-20-GG-17	39.66	13.58	0.33	0.17	46.26	0.23	100.22	85.86
	72-20-GG-18	39.61	14.96	0.31	0.20	45.30	0.26	100.63	84.37
	72-20-GG-19	39.89	13.01	0.35	0.17	46.68	0.18	100.29	86.48
	72-20-GG-20	39.54	14.73	0.31	0.19	45.31	0.25	100.33	84.58
	72-20-GG-21	39.36	14.93	0.30	0.20	45.17	0.22	100.17	84.36
	72-20-GG-22	39.54	14.36	0.31	0.19	45.58	0.26	100.24	84.98
	72-20-GG-24	39.69	13.84	0.31	0.19	45.72	0.27	100.01	85.49
Pioneer	P5-526-rk2-1	39.59	13.90	0.36	0.19	45.82	0.24	100.10	85.45
	P5-526-rk2-2	39.32	14.02	0.33	0.18	45.32	0.22	99.39	85.21
	P5-526-rk2-3	39.71	13.81	0.37	0.19	45.73	0.24	100.04	85.51
	P5-526-rk2-4	39.60	13.97	0.39	0.17	45.53	0.20	99.87	85.32
	P5-526-rk2-5	39.14	16.54	0.27	0.22	43.34	0.25	99.77	82.36
	P5-526-rk2-6	39.61	15.53	0.29	0.20	44.54	0.22	100.39	83.64
	P5-526-rk2-7	39.33	15.80	0.28	0.21	44.17	0.24	100.03	83.29
	P5-526-rk2-8	39.46	14.90	0.27	0.20	44.99	0.24	100.06	84.33
	P5-526-rk2-9	39.74	14.80	0.29	0.20	45.03	0.23	100.30	84.43
	P5-526-rk2-10	39.70	13.01	0.38	0.17	46.34	0.22	99.81	86.40
	P5-526-rk2-11	38.99	16.33	0.30	0.22	43.54	0.22	99.60	82.62
	P5-526-rk2-12	39.45	14.97	0.26	0.20	44.71	0.25	99.83	84.18
	P5-526-rk2-13	39.19	16.19	0.25	0.21	43.71	0.25	99.80	82.79
	P5-526-rk2-14	39.24	15.34	0.28	0.20	44.18	0.23	99.47	83.70
	P5-526-rk2-15	39.09	16.26	0.27	0.22	43.76	0.24	99.83	82.75

TABLE A.2 CONT.

Seamount	Sample	SiO_2	FeO	NiO	MnO	MgO	CaO	Total	Fo
Pioneer	P5-526-rk2-16	39.60	15.25	0.28	0.20	44.63	0.24	100.20	83.92
	P5-526-rk2-17	39.26	15.35	0.28	0.20	44.40	0.24	99.74	83.76
	P5-526-rk2-18	39.32	15.10	0.30	0.20	44.61	0.28	99.82	84.04
	P5-526-rk2-19	39.09	15.19	0.28	0.20	44.23	0.24	99.22	83.85
	P5-526-rk2-20	39.23	15.55	0.30	0.21	44.29	0.24	99.83	83.54
Gardner	76-6-7-B-1	40.46	10.07	0.37	0.14	49.04	0.22	100.29	89.67
	76-6-7-B-2	40.51	10.15	0.37	0.15	48.85	0.22	100.24	89.56
	76-6-7-B-3	39.90	12.77	0.32	0.18	46.87	0.25	100.29	86.74
	76-6-7-B-4	40.61	10.25	0.38	0.15	49.04	0.23	100.65	89.50
	76-6-7-B-5	39.57	14.36	0.28	0.21	45.50	0.23	100.15	84.96
	76-6-7-B-6	39.88	12.69	0.30	0.18	46.88	0.25	100.19	86.81
	76-6-7-B-7	39.66	13.21	0.36	0.19	46.47	0.25	100.13	86.25
	76-6-7-B-8	40.37	10.11	0.38	0.14	48.87	0.23	100.10	89.61
	76-6-7-B-9	40.31	10.13	0.38	0.14	48.87	0.23	100.06	89.58
	76-6-7-B-10	40.33	10.51	0.38	0.15	48.71	0.23	100.31	89.21
	76-6-7-B-11	39.94	12.91	0.34	0.17	46.72	0.21	100.30	86.57
	76-6-7-B-12	39.65	13.27	0.26	0.19	46.46	0.26	100.09	86.19
	76-6-7-B-13	40.15	12.03	0.32	0.17	47.36	0.25	100.28	87.53
	76-6-7-B-14	40.41	9.54	0.40	0.14	49.44	0.22	100.15	90.24
	76-6-7-B-15	40.34	9.95	0.36	0.14	49.06	0.22	100.07	89.78
	76-6-7-B-16	40.33	10.42	0.39	0.15	48.70	0.25	100.23	89.28
	76-6-7-B-17	40.29	10.42	0.38	0.15	48.71	0.22	100.17	89.29
	76-6-7-B-18	40.61	9.69	0.39	0.14	49.48	0.25	100.56	90.10
	76-6-7-B-19	39.55	14.31	0.29	0.20	45.58	0.27	100.20	85.02
	76-6-7-B-20	40.16	11.74	0.31	0.16	47.74	0.24	100.34	87.87
	76-6-7-B-21	40.46	9.74	0.40	0.14	49.44	0.22	100.39	90.04

TABLE A.2 CONT.

Seamount	Sample	SiO_2	FeO	NiO	MnO	MgO	CaO	Total	Fo
Gardner	76-6-7-B-22	40.26	10.92	0.37	0.15	48.36	0.23	100.28	88.76
	76-6-7-B-23	40.23	10.44	0.35	0.14	48.73	0.23	100.12	89.27
	76-6-7-B-24	39.68	13.91	0.27	0.20	45.95	0.27	100.27	85.49
	76-6-7-B-25	40.39	9.91	0.41	0.14	49.15	0.23	100.22	89.84
	76-6-7-C-1	40.54	9.99	0.38	0.14	48.70	0.22	99.96	89.68
	76-6-7-C-2	40.56	10.45	0.37	0.14	48.41	0.22	100.16	89.20
	76-6-7-C-3	40.57	9.86	0.33	0.13	48.94	0.23	100.05	89.85
	76-6-7-C-4	40.64	9.69	0.38	0.13	49.15	0.21	100.21	90.04
	76-6-7-C-5	40.55	9.51	0.40	0.13	49.03	0.21	99.84	90.18
	76-6-7-C-6	40.55	9.44	0.39	0.13	49.09	0.21	99.81	90.26
	76-6-7-C-7	40.62	9.87	0.38	0.13	49.00	0.21	100.21	89.85
	76-6-7-C-8	40.49	10.01	0.35	0.13	48.80	0.21	100.00	89.68
	76-6-7-C-9	40.56	9.78	0.39	0.14	49.01	0.21	100.09	89.94
	76-6-7-C-10	40.33	10.74	0.36	0.15	48.13	0.26	99.98	88.87
	76-6-7-C-11	40.55	9.95	0.35	0.13	48.89	0.21	100.08	89.76
	76-6-7-C-12	40.58	9.59	0.39	0.13	49.05	0.21	99.96	90.12
	76-6-7-C-13	40.42	10.24	0.37	0.14	48.57	0.21	99.96	89.42
	76-6-7-C-14	40.52	9.95	0.38	0.14	48.78	0.21	99.99	89.73
	76-6-7-C-15	40.46	10.70	0.36	0.15	48.22	0.22	100.10	88.93
	76-6-7-C-16	40.39	10.47	0.36	0.14	48.38	0.22	99.96	89.18
	76-6-7-C-17	40.59	9.68	0.37	0.13	49.12	0.21	100.11	90.04
	76-6-7-C-18	40.56	9.51	0.39	0.13	49.09	0.21	99.90	90.20
	76-6-7-C-19	40.22	11.14	0.32	0.16	47.62	0.25	99.71	88.40
	76-6-7-C-20	40.61	9.57	0.40	0.13	49.06	0.22	100.00	90.14
	76-6-7-C-21	40.63	9.64	0.38	0.13	49.15	0.22	100.14	90.08
	76-6-7-F-1	40.22	9.90	0.40	0.14	49.23	0.22	100.11	89.86

TABLE A.2 CONT.

Seamount	Sample	SiO_2	FeO	NiO	MnO	MgO	CaO	Total	Fo
Gardner	76-6-7-F-2	40.39	9.52	0.41	0.13	49.58	0.22	100.26	90.27
	76-6-7-F-3	40.52	9.95	0.39	0.14	49.18	0.22	100.39	89.81
	76-6-7-F-4	40.47	9.68	0.41	0.14	49.53	0.22	100.44	90.12
	76-6-7-F-5	27.16	8.86	0.33	0.12	38.86	0.20	75.54	88.66
	76-6-7-F-6	40.31	10.07	0.38	0.14	49.23	0.22	100.35	89.71
	76-6-7-F-7	40.40	9.97	0.37	0.13	49.15	0.22	100.25	89.78
	76-6-7-F-8	40.21	9.96	0.39	0.14	49.19	0.22	100.11	89.80
	76-6-7-F-9	40.29	9.92	0.39	0.13	49.28	0.22	100.23	89.85
	76-6-7-F-10	40.11	10.25	0.37	0.15	48.99	0.22	100.09	89.50
	76-6-7-F-11	39.95	10.44	0.38	0.15	48.67	0.23	99.82	89.26
	76-6-7-F-12	39.34	15.22	0.28	0.22	44.92	0.24	100.23	84.03
	76-6-7-F-13	40.37	9.91	0.34	0.14	49.22	0.22	100.20	89.85
	76-6-7-F-14	40.46	10.26	0.38	0.14	49.01	0.22	100.47	89.49
	76-6-7-F-15	40.15	11.71	0.34	0.16	47.86	0.24	100.46	87.94
	76-6-7-F-16	40.49	9.50	0.41	0.14	49.62	0.22	100.37	90.30
	76-6-7-F-17	40.52	9.53	0.41	0.13	49.70	0.22	100.50	90.29
	76-6-7-F-18	40.44	10.18	0.36	0.14	49.18	0.23	100.53	89.60
	76-6-7-F-19	40.14	10.94	0.35	0.15	48.44	0.22	100.23	88.76
	76-6-7-F-20	40.19	10.75	0.36	0.15	48.54	0.23	100.22	88.95
	76-6-7-F-21	40.42	9.91	0.36	0.13	49.21	0.23	100.26	89.85
	76-6-7-F-22	40.57	9.60	0.38	0.13	49.49	0.21	100.38	90.19
	76-6-7-F-23	40.49	9.57	0.40	0.13	49.46	0.22	100.28	90.20
	76-6-7-F-24	40.58	9.52	0.42	0.13	49.65	0.22	100.51	90.29
	76-6-7-F-25	40.33	9.68	0.38	0.14	49.41	0.21	100.16	90.09
	76-6-7-F-26	40.37	9.84	0.41	0.13	49.34	0.22	100.31	89.94
	76-6-7-F-27	40.50	9.47	0.41	0.14	49.53	0.22	100.25	90.31

TABLE A.2 CONT.

Seamount	Sample	SiO_2	FeO	NiO	MnO	MgO	CaO	Total	Fo
Gardner	76-6-7-F-28	40.36	9.55	0.41	0.14	49.47	0.22	100.15	90.23
	76-6-7-H-1	40.38	8.29	0.46	0.12	50.00	0.21	99.46	91.49
	76-6-7-H-2	39.92	11.45	0.35	0.16	47.52	0.25	99.65	88.10
	76-6-7-H-3	39.88	11.42	0.35	0.16	47.56	0.25	99.61	88.13
	76-6-7-H-4	39.73	12.15	0.36	0.18	46.86	0.22	99.50	87.31
	76-6-7-H-5	39.96	10.30	0.45	0.14	48.41	0.21	99.47	89.34
	76-6-7-H-6	39.89	11.18	0.35	0.16	47.54	0.25	99.36	88.35
	76-6-7-H-7	40.43	8.25	0.48	0.12	50.10	0.21	99.59	91.54
	76-6-7-H-8	40.21	8.78	0.41	0.13	49.74	0.24	99.51	90.98
	76-6-7-H-9	40.28	8.17	0.45	0.12	50.17	0.22	99.41	91.63
	76-6-7-H-10	39.27	13.81	0.31	0.19	45.55	0.27	99.41	85.46
Highest Fo	76-6-7-H-11	40.27	7.95	0.45	0.12	50.25	0.21	99.25	91.85
	76-6-7-H-12	40.22	8.22	0.46	0.12	50.01	0.21	99.25	91.55
	76-6-7-H-13	39.32	13.03	0.37	0.19	46.21	0.24	99.38	86.34
	76-6-7-H-14	40.31	8.34	0.43	0.12	49.99	0.22	99.41	91.45
	76-6-7-H-15	39.24	13.81	0.32	0.19	45.54	0.29	99.39	85.46
	76-6-7-H-16	39.94	10.02	0.38	0.14	48.63	0.24	99.35	89.64
	76-6-7-H-17	39.31	13.77	0.37	0.19	45.67	0.28	99.59	85.53
	76-6-7-H-18	40.02	8.87	0.42	0.13	49.40	0.22	99.06	90.84
	76-6-7-H-19	39.54	12.21	0.35	0.18	46.84	0.25	99.37	87.24
	76-6-7-H-20	39.66	11.64	0.32	0.16	47.26	0.26	99.30	87.86
	76-6-7-H-21	39.15	14.63	0.26	0.21	44.89	0.31	99.46	84.54
	76-6-7-H-22	39.87	10.46	0.43	0.15	48.27	0.24	99.42	89.16
	76-6-7-H-23	39.77	10.73	0.39	0.16	48.10	0.25	99.39	88.88
	76-6-7-H-24	39.33	13.00	0.32	0.19	46.35	0.26	99.44	86.41
	76-6-7-H-25	40.14	8.64	0.46	0.12	49.78	0.22	99.35	91.12

TABLE A.2 CONT.

Seamount	Sample	SiO_2	FeO	NiO	MnO	MgO	CaO	Total	Fo
Gardner	76-6-7-H-26	39.75	11.92	0.34	0.17	47.24	0.25	99.68	87.60
	76-6-7-H-27	39.52	12.18	0.35	0.17	46.93	0.25	99.40	87.29
	76-6-7-H-28	39.39	12.45	0.31	0.17	46.65	0.25	99.23	86.98
	76-6-7-H-29	38.78	15.91	0.29	0.23	43.90	0.21	99.32	83.10
	76-6-7-H-30	39.70	10.56	0.36	0.16	48.24	0.26	99.28	89.06
	76-6-7-H-31	39.66	11.59	0.34	0.16	47.41	0.25	99.42	87.94
	76-6-7-H-32	39.71	10.93	0.35	0.16	47.97	0.25	99.37	88.66
	76-6-7-H-33	39.98	10.19	0.39	0.15	48.55	0.25	99.50	89.47
	76-6-7-H-34	39.76	10.43	0.37	0.15	48.38	0.24	99.34	89.21
	76-6-7-H-35	39.91	10.30	0.39	0.14	48.58	0.24	99.56	89.37
	76-6-7-I-2	39.75	11.51	0.30	0.17	47.40	0.24	99.37	88.01
	76-6-7-I-3	38.90	15.96	0.24	0.24	43.53	0.29	99.16	82.94
	76-6-7-I-4	39.66	12.15	0.34	0.18	46.93	0.26	99.52	87.31
	76-6-7-I-5	38.97	15.69	0.30	0.23	43.82	0.25	99.25	83.27
	76-6-7-I-6	39.51	12.99	0.36	0.18	46.11	0.28	99.44	86.35
	76-6-7-I-7	39.61	12.28	0.32	0.18	46.73	0.27	99.38	87.15
	76-6-7-I-8	39.52	12.33	0.30	0.18	46.61	0.26	99.20	87.07
	76-6-7-I-9	39.77	9.97	0.41	0.13	47.62	0.23	98.12	89.49
	76-6-7-I-10	39.18	14.13	0.31	0.20	45.11	0.31	99.24	85.05
	76-6-7-I-11	39.76	11.15	0.34	0.15	47.61	0.26	99.28	88.38
	76-6-7-I-12	39.39	14.04	0.31	0.20	45.35	0.27	99.56	85.20
	76-6-7-I-13	39.67	11.46	0.34	0.17	47.27	0.27	99.18	88.02
	76-6-7-I-14	39.84	10.96	0.39	0.16	47.83	0.26	99.44	88.61
	76-6-7-I-15	39.50	12.81	0.38	0.19	46.17	0.24	99.28	86.53
	76-6-7-I-16	39.81	11.69	0.41	0.17	47.30	0.24	99.62	87.82
	76-6-7-I-17	39.92	11.42	0.33	0.16	47.68	0.24	99.74	88.16

TABLE A.2 CONT.

Seamount	Sample	SiO_2	FeO	NiO	MnO	MgO	CaO	Total	Fo
Gardner	76-6-7-I-18	39.97	9.83	0.41	0.14	48.67	0.23	99.25	89.83
	76-6-7-I-19	40.02	10.30	0.33	0.15	48.48	0.24	99.51	89.35
	76-6-7-I-20	40.13	9.03	0.38	0.13	49.52	0.22	99.41	90.72
	76-6-7-I-21	39.76	11.23	0.35	0.16	47.73	0.25	99.49	88.34
	76-6-7-I-22	39.04	15.52	0.27	0.22	44.23	0.28	99.56	83.55
	76-6-7-I-23	40.04	9.62	0.39	0.14	48.89	0.27	99.35	90.06
	76-6-7-I-24	39.54	12.24	0.36	0.18	46.70	0.25	99.27	87.18
	76-6-7-I-25	40.09	9.17	0.42	0.13	49.36	0.22	99.39	90.57
	76-6-7-I-26	39.85	10.67	0.35	0.16	48.06	0.25	99.33	88.92
	76-6-7-I-27	40.26	8.32	0.45	0.12	49.98	0.22	99.36	91.46
	76-6-7-I-28	39.39	13.14	0.34	0.19	45.97	0.28	99.31	86.18
	76-6-7-I-29	39.90	9.81	0.36	0.14	48.65	0.24	99.09	89.84
	76-6-7-I-30	40.24	8.62	0.44	0.12	49.91	0.23	99.57	91.17
	76-6-7-J-1	40.15	9.64	0.38	0.13	48.93	0.22	99.44	90.05
	76-6-7-J-2	40.00	10.21	0.33	0.14	48.42	0.22	99.32	89.42
	76-6-7-J-3	40.01	10.02	0.37	0.13	48.49	0.21	99.24	89.61
	76-6-7-J-4	39.42	13.96	0.20	0.20	45.42	0.25	99.44	85.29
	76-6-7-J-5	39.87	11.16	0.34	0.16	47.66	0.24	99.43	88.39
	76-6-7-J-6	40.21	9.78	0.40	0.14	48.89	0.21	99.63	89.91
	76-6-7-J-7	39.89	11.02	0.35	0.16	47.66	0.23	99.31	88.52
	76-6-7-J-8	40.16	9.43	0.41	0.13	49.13	0.22	99.48	90.28
	76-6-7-J-9	40.11	9.96	0.34	0.14	48.68	0.22	99.45	89.71
	76-6-7-J-10	40.08	9.79	0.39	0.14	48.78	0.22	99.39	89.88
	76-6-7-J-11	40.18	9.33	0.41	0.14	49.19	0.22	99.46	90.38
	76-6-7-J-12	39.41	13.17	0.32	0.19	45.84	0.23	99.16	86.12
	76-6-7-J-13	40.05	10.38	0.37	0.15	48.27	0.23	99.44	89.24

TABLE A.2 CONT.

Seamount	Sample	SiO_2	FeO	NiO	MnO	MgO	CaO	Total	Fo
Gardner	76-6-7-J-14	40.04	9.65	0.38	0.14	48.86	0.22	99.29	90.02
	76-6-7-J-15	40.02	10.87	0.29	0.15	47.89	0.22	99.44	88.71
	76-6-7-J-16	40.17	9.90	0.38	0.14	48.60	0.24	99.43	89.75
	76-6-7-J-17	40.17	9.91	0.37	0.14	48.74	0.22	99.54	89.77
	76-6-7-J-18	40.05	10.27	0.36	0.15	48.38	0.22	99.43	89.35
	76-6-7-J-20	40.02	10.54	0.35	0.15	48.15	0.23	99.43	89.06
	76-6-7-J-21	39.36	14.25	0.21	0.21	45.26	0.24	99.52	84.99
	76-6-7-J-22	39.46	13.75	0.36	0.20	45.48	0.27	99.52	85.50
	76-6-7-J-24	39.26	14.98	0.18	0.22	44.64	0.25	99.53	84.15
	76-6-7-J-25	40.26	9.41	0.40	0.13	49.12	0.21	99.54	90.30
	76-6-7-J-26	39.55	13.03	0.32	0.18	46.02	0.25	99.35	86.29
	76-6-7-J-27	39.92	11.14	0.34	0.16	47.64	0.24	99.44	88.40
	76-6-7-J-28	40.26	9.75	0.37	0.14	48.79	0.22	99.54	89.92
	76-6-7-J-29	40.30	9.43	0.38	0.13	49.10	0.21	99.55	90.27
	76-6-7-J-30	40.26	9.31	0.40	0.14	49.04	0.22	99.37	90.37
	76-6-7-J-31	40.31	9.44	0.39	0.13	49.06	0.22	99.56	90.26
	76-6-7-J-32	39.40	13.72	0.27	0.19	45.42	0.28	99.28	85.51
Mokumanamana	NEC-2A-1	39.57	14.32	0.27	0.19	45.19	0.27	99.82	84.91
	NEC-2A-2	39.50	14.99	0.26	0.20	44.71	0.30	99.96	84.17
	NEC-2A-3	39.56	14.48	0.27	0.19	45.22	0.29	100.01	84.77
	NEC-2A-4	39.41	15.35	0.27	0.20	44.42	0.27	99.93	83.76
	NEC-2A-5	39.38	15.45	0.26	0.21	44.31	0.31	99.92	83.64
	NEC-2A-6	39.62	14.47	0.27	0.19	45.17	0.27	99.98	84.77
	NEC-2A-7	39.34	15.12	0.26	0.20	44.13	0.32	99.37	83.87
	NEC-2A-8	39.31	15.76	0.26	0.21	44.14	0.31	99.99	83.31
	NEC-2A-9	39.24	15.93	0.26	0.21	43.83	0.30	99.77	83.07

TABLE A.2 CONT.

Seamount	Sample	SiO_2	FeO	NiO	MnO	MgO	CaO	Total	Fo
Mokumanamana	NEC-2A-10	39.38	15.40	0.27	0.20	44.34	0.31	99.90	83.70
	NEC-2A-11	39.43	15.55	0.27	0.20	44.32	0.31	100.08	83.55
	NEC-2A-12	39.41	15.42	0.27	0.20	44.33	0.31	99.93	83.67
	NEC-2A-13	39.41	15.04	0.27	0.20	44.68	0.30	99.91	84.11
	NEC-2A-14	39.26	15.23	0.26	0.20	44.28	0.31	99.53	83.83
	NEC-2A-15	39.33	15.12	0.29	0.20	44.41	0.25	99.59	83.97
	NEC-2A-16	39.31	15.41	0.27	0.21	44.34	0.31	99.84	83.69
	NEC-2A-17	39.50	14.25	0.27	0.19	45.25	0.26	99.71	84.99
	NEC-2A-18	39.53	14.01	0.27	0.19	45.48	0.27	99.74	85.26
	NEC-2A-19	39.31	15.34	0.26	0.20	44.33	0.31	99.75	83.74
	NEC-2A-20	39.26	15.70	0.26	0.21	44.08	0.29	99.81	83.35
	NEC-2A-21	39.33	15.10	0.26	0.20	44.40	0.29	99.59	83.97
	NEC-3A-1	39.51	15.00	0.26	0.20	44.37	0.31	99.65	84.06
	NEC-3A-2	39.55	13.97	0.27	0.19	45.17	0.21	99.36	85.21
	NEC-3A-3	39.31	15.21	0.26	0.20	44.24	0.30	99.52	83.83
	NEC-3A-4	39.28	15.41	0.26	0.20	44.01	0.30	99.47	83.58
	NEC-3A-5	39.35	15.34	0.27	0.20	44.27	0.28	99.70	83.72
	NEC-3A-6	39.26	15.34	0.26	0.20	44.16	0.31	99.54	83.69
	NEC-3A-7	39.42	14.66	0.27	0.20	44.78	0.27	99.59	84.48
	NEC-3A-8	39.31	15.48	0.26	0.21	44.10	0.30	99.67	83.55
	NEC-3A-9	39.30	15.39	0.27	0.20	44.16	0.30	99.63	83.64
	NEC-3A-10	39.54	14.07	0.28	0.19	45.31	0.26	99.64	85.16
	NEC-3A-11	39.36	15.45	0.27	0.20	44.14	0.29	99.70	83.59
	NEC-3A-12	39.25	15.57	0.26	0.20	44.11	0.27	99.67	83.47
	NEC-3A-13	39.43	14.54	0.27	0.19	44.83	0.24	99.49	84.60
	NEC-3A-14	39.41	15.26	0.27	0.20	44.35	0.28	99.76	83.82

TABLE A.2 CONT.

Seamount	Sample	SiO_2	FeO	NiO	MnO	MgO	CaO	Total	Fo
Mokumanamana	NEC-3A-15	39.16	15.86	0.26	0.21	43.82	0.28	99.59	83.13
	NEC-3A-16	39.35	15.43	0.26	0.20	44.19	0.31	99.74	83.62
	NEC-3A-17	39.43	15.23	0.27	0.20	44.45	0.29	99.88	83.87
	NEC-3A-18	39.34	15.40	0.27	0.20	44.20	0.29	99.70	83.65
	NEC-3A-19	39.47	15.22	0.27	0.21	44.42	0.30	99.87	83.88
	NEC-3A-20	39.32	15.16	0.27	0.20	44.38	0.29	99.62	83.92
Twin Banks	P5-688-1-1	39.54	14.01	0.31	0.18	45.74	0.21	100.00	85.34
	P5-688-1-2	39.55	14.04	0.31	0.18	45.73	0.21	100.02	85.31
	P5-688-1-3	39.59	13.89	0.32	0.18	45.83	0.23	100.05	85.47
	P5-688-1-4	39.61	14.19	0.29	0.19	45.65	0.21	100.13	85.15
	P5-688-1-5	39.40	15.61	0.29	0.21	44.44	0.25	100.21	83.54
	P5-688-1-6	39.43	15.16	0.30	0.20	44.82	0.21	100.13	84.05
	P5-688-1-7	39.33	15.43	0.29	0.20	44.46	0.24	99.96	83.70
	P5-688-1-8	39.40	14.37	0.31	0.19	45.37	0.22	99.87	84.91
	P5-688-1-9	39.41	14.29	0.31	0.19	45.47	0.23	99.91	85.01
	P5-688-1-10	39.25	15.19	0.29	0.20	44.75	0.26	99.94	84.00
	P5-688-1-11	39.33	14.98	0.30	0.20	44.83	0.25	99.89	84.21
	P5-688-1-12	40.04	11.64	0.41	0.15	47.60	0.19	100.02	87.94
	P5-688-1-13	39.83	13.33	0.31	0.16	46.23	0.19	100.06	86.08
	P5-688-1-14	39.67	14.49	0.31	0.19	45.28	0.25	100.18	84.78
	P5-688-1-15	39.62	14.37	0.30	0.19	45.46	0.25	100.19	84.94
	P5-688-1-16	39.30	14.33	0.32	0.18	45.26	0.20	99.59	84.91
	P5-688-1-17	39.47	14.41	0.29	0.19	45.24	0.22	99.82	84.84
	P5-688-1-18	39.15	15.61	0.29	0.21	44.14	0.24	99.64	83.45
	P5-688-1-19	39.51	14.77	0.30	0.19	44.91	0.23	99.91	84.43
	P5-688-1-20	40.17	11.48	0.40	0.15	47.91	0.17	100.29	88.15

TABLE A.2 CONT.

Seamount	Sample	SiO_2	FeO	NiO	MnO	MgO	CaO	Total	Fo
West Nīhoa	76-9-11-1	39.50	14.42	0.31	0.19	45.21	0.27	99.90	84.82
	76-9-11-2	39.66	14.59	0.31	0.19	45.03	0.24	100.03	84.62
	76-9-11-3	39.60	14.36	0.30	0.19	45.17	0.25	99.87	84.87
	76-9-11-4	39.58	13.88	0.32	0.18	45.55	0.20	99.72	85.40
	76-9-11-5	39.60	14.91	0.30	0.20	44.87	0.26	100.13	84.28
	76-9-11-6	39.66	14.10	0.30	0.18	45.46	0.22	99.93	85.18
	76-9-11-7	39.37	15.59	0.29	0.20	44.38	0.25	100.07	83.54
	76-9-11-8	39.47	14.52	0.30	0.19	45.10	0.26	99.83	84.70
	76-9-11-9	39.60	13.87	0.32	0.18	45.68	0.20	99.84	85.44
	76-9-11-10	39.58	13.74	0.31	0.18	45.77	0.24	99.82	85.59
	76-9-11-11	38.96	16.56	0.30	0.21	43.59	0.24	99.87	82.44
	76-9-11-12	39.62	14.89	0.30	0.19	44.90	0.25	100.16	84.32
	76-9-11-13	39.43	15.01	0.29	0.20	44.75	0.25	99.93	84.17
	76-9-11-14	39.39	14.99	0.31	0.19	44.93	0.24	100.05	84.24
	76-9-11-15	39.45	15.25	0.30	0.19	44.60	0.24	100.04	83.90
Nīhoa	NIH-D1-2-1	36.82	14.68	0.33	0.18	44.73	0.21	96.95	84.45
	NIH-D1-2-2	36.66	14.70	0.33	0.19	44.62	0.21	96.72	84.40
	NIH-D1-2-3	36.83	15.02	0.33	0.19	44.35	0.21	96.92	84.03
	NIH-D1-2-4	36.62	14.82	0.33	0.18	44.56	0.21	96.73	84.28
	NIH-D1-2-5	36.64	15.05	0.33	0.19	44.48	0.21	96.89	84.04
	NIH-D1-2-6	36.53	14.87	0.33	0.19	44.57	0.20	96.69	84.24
	NIH-D1-2-7	36.32	14.94	0.33	0.19	44.47	0.21	96.46	84.14
	NIH-D1-2-8	36.69	14.97	0.33	0.19	44.55	0.20	96.93	84.13
	NIH-D1-2-9	36.87	14.73	0.33	0.19	44.57	0.21	96.90	84.36
	NIH-D1-2-10	36.46	16.31	0.31	0.21	43.40	0.22	96.91	82.58
	NIH-D1-2-11	36.80	14.99	0.32	0.19	44.51	0.20	97.00	84.10

TABLE A.2 CONT.

Seamount	Sample	SiO_2	FeO	NiO	MnO	MgO	CaO	Total	Fo
Nīhoa	NIH-D1-2-12	37.10	15.12	0.33	0.19	44.55	0.21	97.49	84.01
	NIH-D1-2-13	36.81	14.78	0.33	0.19	44.65	0.20	96.97	84.34
	NIH-D1-2-14	36.73	14.78	0.33	0.19	44.60	0.20	96.83	84.32
	NIH-D1-2-15	36.75	14.78	0.33	0.18	44.65	0.20	96.90	84.34
	NIH-D1-2-16	36.82	15.86	0.32	0.19	43.91	0.21	97.30	83.15
	NIH-D1-2-17	37.07	14.47	0.34	0.18	44.99	0.21	97.25	84.72
	NIH-D1-2-18	36.63	14.92	0.33	0.19	44.55	0.20	96.82	84.19
	NIH-D1-2-20	36.72	15.00	0.33	0.18	44.55	0.20	96.99	84.11
	NIH-D1-2-21	36.94	14.81	0.32	0.18	44.56	0.21	97.03	84.28
	NIH-D1-2-22	36.78	14.80	0.33	0.19	44.59	0.21	96.90	84.30
	NIH-D1-2-23	36.82	14.77	0.32	0.18	44.70	0.21	97.00	84.36
	NIH-D1-2-24	36.68	15.14	0.32	0.19	44.48	0.20	97.02	83.96
	NIH-D1-2-25	36.61	15.15	0.32	0.19	44.32	0.21	96.80	83.91
	NIH-D4-1	38.58	17.62	0.30	0.22	42.02	0.23	98.96	80.96
	NIH-D4-2	38.63	17.74	0.29	0.22	42.16	0.23	99.28	80.90
	NIH-D4-3	38.76	17.72	0.30	0.22	42.03	0.23	99.26	80.87
	NIH-D4-4	38.67	17.68	0.30	0.22	42.07	0.23	99.17	80.92
	NIH-D4-5	38.66	17.77	0.29	0.22	42.09	0.23	99.26	80.85
	NIH-D4-6	38.68	17.73	0.29	0.22	42.05	0.23	99.20	80.87
	NIH-D4-7	38.77	17.80	0.29	0.22	41.65	0.23	98.96	80.66
	NIH-D4-8	38.78	17.64	0.30	0.22	42.00	0.23	99.16	80.93
	NIH-D4-9	38.76	17.64	0.29	0.22	41.94	0.23	99.10	80.91
	NIH-D4-10	38.61	17.68	0.30	0.22	42.20	0.23	99.24	80.97
	NIH-D4-11	38.65	17.74	0.30	0.22	42.04	0.23	99.18	80.86
	NIH-D4-12	38.76	17.77	0.29	0.22	42.04	0.23	99.30	80.83
	NIH-D4-13	38.71	17.70	0.29	0.22	41.99	0.23	99.14	80.88

TABLE A.2 CONT.

Seamount	Sample	SiO_2	FeO	NiO	MnO	MgO	CaO	Total	Fo
Nīhoa	NIH-D4-14	37.62	17.72	0.29	0.22	42.02	0.22	98.10	80.87
	NIH-D4-15	36.38	17.64	0.30	0.22	42.20	0.22	96.96	81.00
	NIH-D4-16	36.41	17.95	0.32	0.22	42.05	0.22	97.17	80.68
	NIH-D4-17	36.28	17.71	0.29	0.22	42.29	0.22	97.02	80.97
	NIH-D4-18	36.49	17.62	0.30	0.22	42.23	0.23	97.09	81.03
	NIH-D4-19	36.38	15.96	0.34	0.20	43.64	0.20	96.71	82.98
	NIH-D4-20	36.13	17.76	0.29	0.22	42.24	0.22	96.86	80.92
	NIH-D4-21	36.35	17.73	0.30	0.22	42.26	0.23	97.08	80.95
	NIH-D4-22	36.39	17.72	0.29	0.22	42.21	0.22	97.06	80.94
	NIH-D4-24	36.32	17.68	0.29	0.22	42.11	0.23	96.84	80.94
	NIH-D4-25	36.60	17.69	0.30	0.22	42.33	0.23	97.37	81.01
	NIH-F-5A-1	39.66	12.66	0.37	0.16	46.32	0.21	99.38	86.71
	NIH-F-5A-2	39.57	12.98	0.37	0.18	45.90	0.22	99.21	86.31
	NIH-F-5A-3	39.72	12.61	0.38	0.16	46.27	0.21	99.34	86.74
	NIH-F-5A-4	39.70	13.15	0.36	0.17	46.13	0.22	99.74	86.21
	NIH-F-5A-5	39.41	13.58	0.36	0.18	45.59	0.22	99.33	85.68
	NIH-F-5A-6	39.68	12.24	0.38	0.16	46.65	0.21	99.32	87.17
	NIH-F-5A-7	39.31	13.46	0.37	0.17	45.77	0.21	99.30	85.84
	NIH-F-5A-8	39.32	13.51	0.36	0.17	45.60	0.20	99.17	85.75
	NIH-F-5A-9	39.66	12.09	0.40	0.16	46.85	0.19	99.35	87.36
	NIH-F-5A-10	39.74	12.72	0.38	0.17	46.63	0.19	99.83	86.73
	NIH-F-5A-11	39.43	13.34	0.37	0.17	45.81	0.21	99.33	85.95
	NIH-F-5A-12	39.49	13.42	0.37	0.17	45.66	0.20	99.32	85.84
	NIH-F-5A-13	39.65	12.74	0.37	0.17	46.23	0.21	99.37	86.61
	NIH-F-5A-14	39.45	13.36	0.37	0.17	45.73	0.21	99.30	85.92
	NIH-F-5A-15	39.55	13.06	0.37	0.17	45.95	0.21	99.32	86.25

TABLE A.2 CONT.

Seamount	Sample	SiO_2	FeO	NiO	MnO	MgO	CaO	Total	Fo
Nīhoa	NIH-F-5A-16	39.52	12.98	0.37	0.17	46.18	0.22	99.44	86.38
	NIH-F-5A-17	39.34	13.36	0.36	0.17	45.85	0.21	99.29	85.95
	NIH-F-5A-18	39.51	13.96	0.33	0.18	45.42	0.21	99.61	85.29
	NIH-F-5A-19	39.73	12.71	0.37	0.16	46.25	0.23	99.46	86.64
	NIH-F-5A-20	39.45	13.71	0.36	0.18	45.45	0.21	99.36	85.53
	NIH-F-5A-21	39.37	13.59	0.34	0.18	45.45	0.21	99.15	85.64
	NIH-F-5A-22	39.34	13.44	0.36	0.18	45.67	0.23	99.21	85.83
	NIH-F-5A-23	39.16	13.34	0.37	0.17	45.83	0.21	99.08	85.96
	NIH-F-5A-24	39.46	13.25	0.37	0.17	45.92	0.21	99.38	86.07
	NIH-F-5A-25	39.54	12.82	0.37	0.17	46.10	0.21	99.20	86.51
	NIH-F-5A-26	39.28	14.32	0.35	0.19	44.80	0.22	99.16	84.79
	NIH-F-9-3	39.97	11.60	0.40	0.15	47.29	0.19	99.61	87.90
	NIH-F-9-4	39.87	11.25	0.39	0.15	47.45	0.20	99.31	88.26
	NIH-F-9-5	39.87	11.82	0.39	0.15	46.94	0.19	99.35	87.62
	NIH-F-9-6	39.93	11.57	0.39	0.15	47.30	0.19	99.54	87.94
	NIH-F-9-7	39.90	11.49	0.39	0.15	47.24	0.20	99.37	87.99
	NIH-F-9-8	39.80	12.38	0.35	0.16	46.58	0.23	99.50	87.03
	NIH-F-9-9	39.89	11.53	0.40	0.15	47.27	0.19	99.42	87.96
	NIH-F-9-10	39.82	12.44	0.37	0.16	46.57	0.21	99.58	86.96
	NIH-F-9-11	39.68	12.70	0.37	0.16	46.31	0.22	99.44	86.67
	NIH-F-9-12	39.50	12.97	0.36	0.17	45.94	0.23	99.16	86.33
	NIH-F-9-13	39.54	12.71	0.37	0.16	46.14	0.21	99.14	86.61
	NIH-F-9-14	39.67	12.61	0.36	0.17	46.38	0.22	99.41	86.77
	NIH-F-9-15	39.69	12.92	0.37	0.16	46.17	0.21	99.53	86.43
	NIH-F-9-16	39.86	11.79	0.39	0.15	47.02	0.19	99.41	87.67
	NIH-F-9-17	39.73	11.79	0.38	0.16	46.96	0.20	99.20	87.65

TABLE A.2 CONT.

Seamount	Sample	SiO_2	FeO	NiO	MnO	MgO	CaO	Total	Fo
Nīhoa	NIH-F-9-18	39.89	11.51	0.40	0.15	47.36	0.19	99.49	88.00
	NIH-F-9-19	39.84	11.58	0.38	0.15	47.23	0.19	99.37	87.91
	NIH-F-9-20	39.79	12.10	0.38	0.16	46.96	0.21	99.60	87.37
	NIH-F-9-21	39.41	14.40	0.32	0.18	44.96	0.21	99.49	84.77
	NIH-F-9-22	39.86	11.61	0.39	0.15	47.27	0.18	99.47	87.89
	NIH-F-9-23	39.94	11.68	0.40	0.15	47.32	0.20	99.69	87.84
	NIH-F-9-24	39.93	11.67	0.40	0.15	47.39	0.19	99.74	87.86
	NIH-F-9-25	39.75	12.22	0.39	0.15	46.80	0.19	99.49	87.23
	NIH-W-11-1-1	39.01	17.56	0.32	0.23	42.28	0.09	99.49	81.10
	NIH-W-11-1-2	39.06	17.64	0.32	0.22	42.35	0.09	99.67	81.06
	NIH-W-11-1-3	39.61	14.40	0.35	0.18	44.88	0.21	99.62	84.75
	NIH-W-11-1-4	39.01	17.78	0.33	0.22	42.14	0.06	99.53	80.86
	NIH-W-11-1-5	39.89	13.35	0.37	0.17	45.81	0.21	99.80	85.95
	NIH-W-11-1-6	40.02	12.39	0.38	0.16	46.60	0.20	99.75	87.02
	NIH-W-11-1-7	39.77	13.93	0.36	0.18	45.38	0.20	99.82	85.31
	NIH-W-11-1-8	39.97	12.61	0.38	0.16	46.45	0.20	99.76	86.78
	NIH-W-11-1-9	39.94	13.04	0.38	0.16	46.14	0.21	99.87	86.32
	NIH-W-11-1-10	39.45	15.54	0.29	0.20	44.06	0.21	99.74	83.48
	NIH-W-11-1-11	39.95	12.67	0.38	0.16	46.55	0.21	99.91	86.76
	NIH-W-11-1-12	39.83	13.19	0.38	0.17	46.02	0.20	99.78	86.15
	NIH-W-11-1-13	39.55	14.85	0.30	0.19	44.63	0.22	99.74	84.27
	NIH-W-11-1-14	39.96	12.56	0.38	0.16	46.53	0.20	99.79	86.84
	NIH-W-11-1-15	39.75	13.76	0.35	0.18	45.44	0.21	99.67	85.48
	NIH-W-11-1-16	39.69	13.47	0.36	0.17	45.62	0.21	99.52	85.79
	NIH-W-11-1-17	39.36	16.07	0.27	0.20	43.64	0.22	99.75	82.88
	NIH-W-11-1-18	39.61	13.58	0.37	0.17	45.54	0.21	99.49	85.67

TABLE A.2 CONT.

Seamount	Sample	SiO_2	FeO	NiO	MnO	MgO	CaO	Total	Fo
Nīhoa	NIH-W-11-1-19	39.75	13.02	0.37	0.17	46.02	0.21	99.54	86.31
	NIH-W-11-1-20	39.69	13.20	0.37	0.17	45.95	0.20	99.57	86.12
	NIH-W-11-1-21	39.80	13.95	0.34	0.18	45.48	0.21	99.96	85.32
Kauaʻi	KV04-16-01	40.19	11.46	0.35	0.16	48.11	0.18	100.45	88.21
	KV04-16-02	39.84	14.03	0.37	0.19	46.12	0.21	100.75	85.42
	KV04-16-03	39.87	13.40	0.34	0.17	46.66	0.18	100.62	86.13
	KV04-16-04	40.01	13.21	0.36	0.18	46.82	0.20	100.76	86.33
	KV04-16-05	40.17	11.45	0.38	0.16	48.04	0.18	100.38	88.21
	KV04-16-06	39.76	13.95	0.32	0.18	46.31	0.21	100.74	85.55
	KV04-16-07	39.93	13.34	0.37	0.18	46.72	0.22	100.76	86.19
	KV04-16-08	39.70	14.23	0.33	0.19	45.97	0.20	100.62	85.20
	KV04-16-09	39.73	13.73	0.35	0.19	46.41	0.21	100.62	85.76
	KV04-16-10	39.81	13.83	0.35	0.19	46.28	0.21	100.67	85.64
	KV04-16-11	39.83	13.18	0.38	0.18	46.91	0.20	100.68	86.39
	KV04-16-12	39.69	13.97	0.31	0.18	46.16	0.21	100.52	85.49
	KV04-16-13	39.69	14.14	0.35	0.19	46.19	0.22	100.78	85.35
	KV04-16-14	39.69	13.41	0.35	0.18	46.67	0.21	100.51	86.12
	KV04-16-15	39.81	13.59	0.35	0.19	46.64	0.24	100.81	85.95
	KV04-16-16	39.82	13.39	0.35	0.18	46.81	0.20	100.74	86.18
	KV04-19-01	39.72	12.52	0.39	0.16	47.17	0.20	100.16	87.04
	KV04-19-02	39.29	15.42	0.29	0.20	45.01	0.23	100.43	83.88
	KV04-19-03	38.94	16.80	0.29	0.20	43.77	0.21	100.21	82.29
	KV04-19-04	39.01	16.51	0.29	0.20	44.12	0.21	100.35	82.65
	KV04-19-05	38.85	18.11	0.26	0.22	43.00	0.21	100.66	80.89
	KV04-19-06	39.46	15.41	0.31	0.21	45.36	0.22	100.96	84.00
	KV04-19-07	38.17	21.01	0.25	0.27	40.49	0.21	100.40	77.45

TABLE A.2 CONT.

Seamount	Sample	SiO_2	FeO	NiO	MnO	MgO	CaO	Total	Fo
Kauaʻi	KV04-19-08	38.92	16.65	0.28	0.21	44.02	0.21	100.28	82.50
	KV04-19-09	38.09	21.07	0.24	0.25	40.35	0.20	100.20	77.34
	KV04-19-10	39.23	14.82	0.30	0.19	45.43	0.21	100.19	84.53
	KV04-19-11	39.21	15.33	0.30	0.20	45.15	0.22	100.40	84.00
	KV04-19-12	39.31	14.80	0.33	0.19	45.52	0.21	100.36	84.58
	KV04-19-13	39.10	14.72	0.33	0.19	45.50	0.21	100.04	84.64
	KV04-19-14	38.99	15.32	0.29	0.20	45.07	0.21	100.07	83.99
	KV04-19-15	39.21	14.65	0.33	0.19	45.56	0.21	100.14	84.72
	KV04-22-01	39.35	14.88	0.34	0.19	45.30	0.19	100.25	84.44
	KV04-22-02	39.81	11.97	0.38	0.16	47.58	0.20	100.10	87.63
	KV04-22-03	39.67	12.03	0.39	0.16	47.55	0.18	99.97	87.57
	KV04-22-04	39.59	13.44	0.38	0.17	46.42	0.19	100.19	86.03
	KV04-22-05	39.59	12.85	0.36	0.17	46.95	0.20	100.11	86.69

TABLE A.3 RMS ERROR IN EPMA MEASUEMENTS USED IN MONTE CARLO

Seamount	Sample	SiO_2	FeO	NiO	MnO	MgO	CaO
Daikakuji	A-55-1	0.608	0.056	0.006	0.008	0.314	0.016
	A-55-2	0.608	0.056	0.006	0.008	0.314	0.016
	A-55-4	0.454	0.065	0.015	0.007	0.305	0.014
Unnamed	84-28-C	0.454	0.065	0.015	0.007	0.305	0.014
	84-28-D	0.454	0.065	0.015	0.007	0.305	0.014
Academician Berg	72-20-GG	1.410	0.210	0.000	0.008	0.960	0.015
Pioneer	P5-526-rk2	1.410	0.210	0.000	0.008	0.960	0.015
Gardner	76-6-7-B	1.410	0.210	0.000	0.008	0.960	0.015
	76-6-7-C	1.324	0.145	0.003	0.006	0.169	0.015
	76-6-7-F	1.410	0.210	0.000	0.008	0.960	0.015
	76-6-7-H	0.395	0.066	0.002	0.007	0.243	0.016
	76-6-7-I	0.395	0.066	0.002	0.007	0.243	0.016
	76-6-7-J	0.395	0.066	0.002	0.007	0.243	0.016
Mokumanamana	NEC-2A	0.405	0.050	0.006	0.005	0.168	0.016
	NEC-3A	0.405	0.050	0.006	0.005	0.168	0.016
Twin Banks	P5-688-1	1.410	0.210	0.000	0.008	0.960	0.015
West Nīhoa	76-9-11	1.410	0.210	0.000	0.008	0.960	0.015
Nīhoa	NIH-D-1-2	1.324	0.145	0.003	0.006	0.169	0.015
	NIH-D4	1.324	0.145	0.003	0.006	0.169	0.015
	NIH-F-5A	1.324	0.145	0.003	0.006	0.169	0.015
	NIH-F-9	1.324	0.145	0.003	0.006	0.169	0.015
	NIH-W-11-1	1.324	0.145	0.003	0.006	0.169	0.015
Kauai	KV04-16	0.420	0.127	0.022	0.009	0.482	0.017
	KV04-19	0.420	0.127	0.022	0.009	0.482	0.017
	KV04-22	0.420	0.127	0.022	0.009	0.482	0.017

References Cited

Amante, C., and Eakins, B.W., 2009. ETOPO1 1 Arc-Minute Global Relief Model: Procedures, Data Sources and Analysis. NOAA Technical Memorandum NESDIS NGDC-24. National Geophysical Data Center, NOAA. doi:10.7289/V5C8276M. Accessed online 08-20-15.

Anderson, D.L., 2000. The thermal state of the upper mantle: no role for mantle plumes. Geophysical Research Letters, Volume 27, Issue 22, p. 3623–3626, doi: 10.1029/2000GL011533.

Armstrong, J.T., 1988. Quantitative analysis of silicate and oxide materials: comparison of Monte Carlo, ZAF, and f(rZ) procedures: in Microbeam Analysis, Newbury DE, ed., p. 239-246.

Ballmer, M.D., Ito, G., and van Keken, P., 2015. Hotspots, large igneous provinces and melting anomalies: in G. Schubert and D. Bercovici, eds., Mantle Dynamics, Elsevier, Treatise of Geophysics 7.10, 2nd edition, p. 393-459.

Ballmer, M. D., G. Ito, Wolfe, C. J., and Solomon, S. C., 2013. Double layering of a thermochemical plume in the upper mantle beneath Hawaii. Earth Planetary Science Letters, Volume 376, p. 155-164, doi: 10.1016/j.epsl.2013.06.022

Bargar, K.E., and Jackson, E.D., 1974. Calculated volumes of individual shield volcanoes along the Hawaiian-Emperor chain. Journal of Research, U.S. Geological Survey, Volume 2, Number 5, p. 545–550.

Carmichael, I.S.E., Turner, F.J., and Verhoogen, J., eds., 1974. Igneous Petrology. McGraw-Hill Inc., U.S.

Clague, D.A., 1996. The growth and subsidence of the Hawaiian-Emperor volcanic chain: in Keast, A., and Miller, S.E., eds., The Origin and Evolution of Pacific Island Biotas, New Guinea to Eastern Polynesia: Patterns and Processes. Amsterdam, Academic Publishing, p. 35–50.

Clague, D.A., Dalrymple, G.B., and Moberly, R., 1975. Petrography and K-Ar ages of dredged volcanic rocks from the western Hawaiian Ridge and the southern Emperor Seamount Chain. Geological Society of America Bulletin, Volume 86, p. 991–998, doi:10.1130/0016-7606(1975)86 <991.PAKAOD>2.0.CO;2.

Clague, D.A., and Sherrod, D.R., 2014. Growth and degradation of Hawaiian volcanoes: in Poland, M.P., Takahashi, T.J., and Landowski, C.M., eds., Characteristics of Hawaiian Volcanoes. U.S. Geological Survey Professional Paper 1801, p. 97–146.

Crough, S.T., 1983. Hotspot swells. Annual Review of Earth and Planetary Sciences, Volume 11, p. 165–193.

Dalrymple, G.B., Clague, D.A., Garcia, M.O., and Bright, S.W., 1987. Petrology and K-Ar ages of dredged samples from Laysan Island and Northampton Bank volcanoes, Hawaiian evolution of the Hawaiian-Emperor chain. Geological Society of America Bulletin, Volume 92, p. 884–933, doi: 10.1130/GSAB-P292-884.

Dalrymple, G.B., Lanphere, M.A., and Jackson, E.D., 1974. Contributions to the petrography and geochronology of volcanic rocks from the leeward Hawaiian Islands. Geological Society of America Bulletin, Volume 85, p. 727–738, doi: 10.1130 /0016-7606(1974)85<727:CTTPAG>2.0.CO;2.

Danyushevsky, L.V., and Plechov, P., 2011. Petrolog3: Integrated software for modeling crystallization processes. Geochemistry, Geophysics, Geosystems, Volume 12, Number 7, Q07021, doi: 10.1029/2011GC003516.

Daubeny, C., 1835. Some account of the eruption of Vesuvius, which occurred in the month of August 1834. Philosophical Transactions of the Royal Society of London, Volume 125, p. 153-159.

Decker, R.W., Wright, T.L., and Stauffer, P.W., eds., 1987. Volcanism in Hawaii. U.S. Geological Survey Professional Paper 1350, p. 997-1018.

Donovan, J., Kremser, D., and Fournelle, J., 2007. Probe for EPMA v. 10.6.6 User's Guide and Reference Xtreme Edition Probe Software, Inc., Eugene, OR, link: http://probesoftware.com/download/PROBEWIN.pdf.

Foulger, G.R. and Natland, J.H., 2003. Is 'hotspot' volcanism a consequence of plate tectonics?. Science, Volume 300(5621), p. 921-922.

Foulger, G.R., Natland, J.H., Presnall, D.C., and Anderson, D.L., 2005. Plates, Plumes, and Paradigms. Boulder, Colorado, Geological Society of America Special Paper 388, p. 881.

Frey, F., Wise, W., Garcia, M.O., West, H., and Kwon, S.T., 1990. Evolution of Mauna Kea Volcano, Hawaii: Petrologic and geochemical constraints on post-shield volcanism. Journal of Geophysical Research, Volume 95, p. 1271–1300, doi: 10.1029/JB095iB02p01271.

Frey, F.A., Garcia, M.O., Wise, W.A.S., Kennedy, A., Gurdet, P., and Albarede, F., 1991. The evolution of Mauna Kea volcano, Hawaii: Petrogenesis of tholeiitic and alkalic basalts. Journal of Geophysical Research, Volume 96, p. 14,347-14,375.

Garcia, M.O., Grooms, D.G., and Naughton, J.J., 1987. Petrology and geochronology of volcanic rocks from seamounts along and near the Hawaiian ridge: Implications for propagation rate of the ridge. Lithos, Volume 20, p. 323–336, doi: 10.1016/S0024-4937(87)80005-1.

Garcia, M.O., Hulsebosch, T., and Rhodes, J., 1995. Olivine-rich submarine basalts from the southwest rift zone of Mauna Loa Volcano: Implications for magmatic processes and geochemical evolution. American Geophysical Union Monograph 92, Mauna Loa Decade Volcano, p. 219-239.

Garcia, M.O., Smith, J.R., Tree, J.P., Weis, D., Harrison, L., and Jicha, B.R., 2015. Petrology, geochemistry, and ages of lavas from Northwest Hawaiian Ridge volcanoes: in Neal, C.R., Sager, W., Erba, E., and Sano, T., eds., The Origin, Evolution, and Environmental Impact of Oceanic Large Igneous Provinces. Geological Society of America Special Paper 511, p. 1–25, doi:10.1130/2015.2511(01).

Garcia, M.O., Swinnard, L., Weis, D., Greene, A.R., Tagami, T., Sano, H., and Gandy, C.E., 2010. Geochemistry and geochronology of Kaua'i lavas over 4.5 Ma: Implications for the origin of rejuvenated volcanism and the petrology, geochemistry, and ages of lavas from Northwest Hawaiian Ridge volcanoes evolution of the Hawaiian plume. Journal of Petrology, Volume 51, p. 1507–1540, doi: 10.1093/petrology/egq027.

Greene, A.R., Garcia, M.O., Pietruszka, A., Marske, J., Weis, D., Vollinger, M.J., and Eiler, J., 2013. Temporal geochemical variations in lavas from Kīlauea's Pu'u 'Ō'ō Eruption (1983-2010): Cyclic variations from the melting of source heterogeneities. Geochemistry, Geophysics, Geosystems., Volume 14, p. 4849–4873, doi: 10.1002/ggge.20285.

Harrison, L.H., Weis, D., Garcia, M.O. in review. The link between Hawaiian mantle plume composition, magmatic flux, and deep mantle geodynamics. Earth and Planetary Science Letters.

Herzberg, C., 1995. Generation of plume magmas through time: An experimental perspective. Chemical Geology, Volume 126, Number 1, p. 1-16.

Herzberg, C., Asimow, P.D., Arndt, N., Niu, Y., Lesher, C.M., Fitton, J.G., Cheadle, M.J., and Saunders, A.D., 2007. Temperatures in ambient mantle and plumes: Constraints from basalts, picrites, and komatiites. Geochemistry, Geophysics, Geosystems, Volume 8, Q02006, doi:10.1029/2006GC001390.

Herzberg, C. and Gazel, E., 2009. Petrological evidence for secular cooling in mantle plumes. Nature, Volume 458, p. 629-622.

Herzberg, C., and O'Hara, M.J., 2002. Plume-associated ultramafic magmas of Phanerozoic age. Journal of Petrology, Volume 43, p. 1857–1883.

Jarosewich, E., Nelen, J.A., and Norberg, J.A., 1980. Corrections. Geostandards Newsletter 4, p. 257-258.

Jarosewich, E., Nelen, J.A., and Norberg, J.A., 1980, Reference samples for electron microprobe analysis. Geostandards Newsletter 4, p. 43-47.

Kress, V.C., and Carmichael, I.S.E., 1988. The compressibility of silicate liquids containing Fe_2O_3 and the effect of composition, temperature, oxygen fugacity and pressure on their redox states. Contributions to Mineralogy and Petrology, Volume 108, p. 82-92.

Larson, L.M., and Pederson, A.K., 2000. Processes in high-Mg, high-T magmas: evidences from olivine, chromite, and glass in Paleogene picrites from West Greenland. Journal of Petrology, Volume 41, p. 1071-1098.

Le Maître, R.W., ed., 2002. Igneous rocks. A Classification and Glossary of Terms: Recommendations of the International Union of Geological Sciences Subcommission on the Systematics of Igneous Rocks (second edition), Cambridge, UK, Cambridge University Press, p. 254.

Lee, C.-T.A., Luffi, P., Plank, T., Dalton, H., and Leeman, W.P., 2009. Constraints on the depths and temperatures of basaltic magma generation on Earth and other terrestrial planets using new thermobarometers for mafic magmas. Earth and Planetary Science Letters, Volume 279, p. 20–33, doi:10.1016/j.epsl.2008.12.020.

Lipman, P.W., Rhodes, J.M., Dalrymple, G.B., 1990. The Ninole Basalt — Implications for the structural evolution of Mauna Loa volcano, Hawaii. Bulletin of Volcanology, Volume 53, Issue 1, p. 1-19, doi: 10.1007/BF00680316.

Lonsdale, P., 1988. Geography and history of the Louisville hotspot chain in the southwest Pacific. Journal of Geophysical Research, Volume 93, p. 3078-3104.

Macdonald, G.A., and Katsura, T., 1964. Chemical composition of the Hawaiian lavas. Journal of Petrology, Volume 5, p. 82–133, doi: 10.1093/petrology/5.1.82.

Matzen, A.K., Baker, M.B, Beckett, J.R., and Stolper, E.M., 2011. Fe-Mg partitioning between olivine and high-magnesium melts and the nature of Hawaiian parental liquids. Journal of Petrology, Volume 52, Issue 7/8, p1243-1263, doi: 10.1093/petrology/egq089.

McKenzie, D., and Bickle, M.J., 1988. The volume and composition of melt generated by extension of the lithosphere. Journal of Petrology, Volume 29, p. 625–679.

Morgan, W.J., 1971. Convection plumes in the lower mantle. Nature, Volume 230, p. 42–43.

Myers, J.L., and Well, A.D., eds., 2003. Research Design and Statistical Analysis (2nd ed.), Lawrence Erlbaum, p. 508. ISBN 0-8058-4037-0.

Norman, M.D. and Garcia, M.O., 1999. Primitive tholeiitic magma compositions and source characteristics of the Hawaiian plume: Constraints from picritic lavas. Earth Planetary Science Letters, Volume 168, p. 19-26.

O'Connor, J.M., Steinberger, B., Regelous, M., Koppers, A.A.P., Wijbrans, J.R., Haase, K.M., Stoffers, P., Jokat, W., and Garbe-Schönberg, D., 2013. Constraints on past plate and mantle motion from new ages for the Hawaiian-Emperor seamount chain. Geochemistry, Geophysics, Geosystems, Volume 14, p. 4564–4584, doi:10.1002/ggge.20267.

Pearce, T.H., 1984. The analysis of zoning in magmatic crystals with emphasis on olivine. Contributions to Mineralogy and Petrology, Volume 86, p. 149-154.

Pietruszka, A.J., Norman, M.D., Garcia, M.O., Marske, J.P., and Burns, D.H., 2013. Chemical heterogeneity in the Hawaiian mantle plume from the alteration and dehydration of recycled oceanic crust. Earth and Planetary Science Letters, Volume 361, p. 298-309.

Putirka, K.D., 2008. Thermometers and barometers for volcanic systems: in Putirka, K.D., and Tepley, F. eds., Reviews in Mineralogy and Geochemistry, Volume 69, p. 61-120.

Putirka, K.D., 2016. Rates and styles of planetary cooling on Earth, Moon, Mars, and Vesta, using new models for oxygen fugacity, ferric-ferrous ratios, olivine-liquid Fe-Mg exchange, and mantle potential temperature. American Mineralogist, Volume 101, p. 819–840.

Putirka, K.D., Perfit, M., Ryerson, F.J., and Jackson, M.G., 2007. Ambient and excess mantle temperatures, olivine thermometry, and active vs. passive upwelling. Chemical Geology, Volume 241, p. 177-206.

Putirka, K.D., Ryerson, F.J., Perfit, M., and Ridley, W.I., 2010. Mineralogy and composition of the oceanic mantle. Journal of Petrology, Volume 52, p. 279-313.

Poland, M.P., Miklius, A., and Montgomery-Brown, E.K., 2014. Magma supply, storage, and transport at shield-stage Hawaiian volcanoes. U. S. Geological Survey Professional Paper 1801, p. 179-235.

Regelous, M., Hofmann, A.W., Abouchami, W., and Galer, S.J.G., 2003. Geochemistry of lavas from the Emperor Seamounts, and the geochemical evolution of Hawaiian magmatism from 85 to 42 Ma. Journal of Petrology, Volume 44, p. 113-140.

Rhodes, J.M., 2016. The aluminum conundrum in Hawaiian shield-building lavas: An argument for a deep, garnet-bearing, mantle source. Geochemica et Cosmochemica Acta, Volume 185, p. 216-231.

Rhodes, J.M., Dungan, M.A., Blanchard, D.P., and Long, P.E., 1979. Magma mixing at mid-ocean ridges: Evidence from basalts drilled near 22^{o} on the Mid-Atlantic Ridge. Tectonophysics, Volume 55, Issues 1–2, p.35–61, doi:10.1016/0040-1951(79)90334-2.

Rhodes, J.M., Huang, S., Frey, F.A., Pringle, M., and Xu, G., 2012. Compositional diversity of Mauna Kea shield lavas recovered by the Hawaii Scientific Drilling Project: Inferences of source lithology, magma supply, and the role of multiple volcanoes. Geochemistry Geophysics Geosystems, Volume 13, Q03014, doi: 10 .1029 /2011GC003812.

Rhodes, J.M., and Vollinger, M.J., 2004. Composition of basaltic lavas sampled by phase-2 of the Hawaii Scientific Drilling Project: Geochemical stratigraphy and magma types. Geochemistry, Geophysics, Geosystems, Volume 5, Q03G13, doi: 10.1029 /2002GC000434.

Ribe, N.M., and Christensen, U.R., 1999. The dynamical origin of Hawaiian volcanism. Earth and Planetary Science Letters, Volume 171, p. 517-531.

Sinton, J., Grönvold, K., and Sæmundsson, K., 2005. Postglacial eruptive history of the western volcanic zone, Iceland. Geochemistry, Geophysics, Geosystems, Volume 6, Q12009, doi: 10.1029/2005GC001021.

Spice, H. E., Fitton, J. G., and Kirstein, L. A., 2016. Temperature fluctuation of the Iceland mantle plume through time. Geochemistry, Geophysics, Geosystems, 17, 243–254, doi:10.1002/2015GC006059.

Stormer, J., 1973. Calcium zoning in olivine and its relationship to silica activity and pressure. Geochimica et Cosmochimica Acta, Volume 27, p. 1815-1821.

Togia, Harrison, 2015. New constraints on temporal variations in Hawaiian plume buoyancy flux. Master's Thesis submitted to the University of Hawai'i at Mānoa, May 2015, p. 1-35.

Toplis, M.J., 2005. The thermodynamics of iron and magnesium partitioning between olivine and liquid: Criteria for assessing and predicting equilibrium in natural and experimental systems. Contributions to Mineralogy and Petrology, Volume 149. Issue 1, p. 22-39, doi: 10.1007/s00410-004-0629-4.

Von Herzen, R.P., Cordery, M.J., Detrick, R.S., and Fang, C., 1989. Heat flow and the thermal origin of hot spot swells: The Hawaiian swell revisited. Journal of Geophysical Research, Volume 94, B10, p. 13783-13799, doi: 10.1029/JB094iB10p13783.

Watson, S., and McKenzie, D., 1991. Melt generations by plumes: a study of Hawaiian volcanism. Journal of Petrology, Volume 32, p. 501-537.

Weis, D., Garcia, M.O., Rhodes, J.M., Jellinek, M., and Scoates, J.S., 2011. Role of the deep mantle in generating the compositional asymmetry of the Hawaiian mantle plume. Nature Geoscience, Volume 4, p. 831–838, doi: 10.1038/ngeo1328.

Wessel, P., 2016. Regional-residual separation of bathymetry and revised estimates of Hawaii plume flux. Geophysical Journal International, Volume 204(2), p. 932-947. doi: 10.1093/gji/ggv472.

White, R.S., 1993. Melt production rates in mantle plumes. Philosophical Transactions of the Royal Society of London, Series A, 342, 1663, p.137–153, doi: 10.1098/rsta.1993.0010.

White, R.S., and McKenzie, D.P., 1989. Magmatism at rift zones: the generation of volcanic continental margins and flood basalts. Journal of the Geological Society of America, Volume 149, p 841-854.

Wilson, J.T., 1963a. A possible origin of the Hawaiian Islands. Canadian Journal of Physics, Volume 41, p. 863-870.

Wilson, J.T., 1963b. Evidence from islands on the spreading of ocean floors. Nature, Volume 197, p. 536-538.

Wilson, J.T., 1973. Mantle plumes and plate motions. Tectonophysics, Volume 19, p. 149-164.

Wolfe, C.J., Solomon, S.C., Laske, G., Collins, J.A., Detrick, R.S., Orcutt, J.A., Bercovici, D., and Hauri, E.H., 2011. Mantle p-wave velocity structure beneath the Hawaiian hotspot: Earth and Planetary Science Letters, Volume 303, p. 267–280, doi: 10.1016 /j.epsl.2011.01.004.

Wright, T.L., 1971. Chemistry of Kilauea and Mauna Loa lava in space and time. U.S. Geological Survey Professional Paper 735, p. 40.

Wright, T.L., and Klein, F.W., 2006. Deep magma transport at Kilauea volcano, Hawaii. Lithos, Volume 87(1–2), p. 50–79, doi: 10.1016/j.lithos.2005.05.004.863–870.

Xu, G., Huang, S., Frey, F., Blichert-Toft, J., Abouchami, W., Clague, D., Cousens, B., Moore, J., and Beeson, M.H., 2014. The distribution of geochemical heterogeneities in the source of Hawaiian shield lavas as revealed by a transect across the strike of the Loa and Kea spatial trends: East Molokai to West Molokai to Penguin Bank. Geochimica et Cosmochimica Acta, Volume 132, p. 214–237.